UC Berkeley
UC Berkeley Electronic Theses and Dissertations

Title
Mechanistic Insights into Hole Transfer from Photoexcited Quantum Dots

Permalink
https://escholarship.org/uc/item/5d07t968

Author
Olshansky, Jacob Hale

Publication Date
2017

Peer reviewed|Thesis/dissertation

Mechanistic Insights into Hole Transfer from Photoexcited Quantum Dots

By

Jacob Hale Olshansky

A dissertation submitted in partial satisfaction of the

requirements for the degree of

Doctor of Philosophy

in

Chemistry

in the

Graduate Division

of the

University of California, Berkeley

Committee in charge:

Professor A. Paul Alivisatos, Chair
Professor Stephen R. Leone
Professor Roya Maboudian

Spring 2017

Abstract

Mechanistic Insights into Hole Transfer from Photoexcited Quantum Dots

by

Jacob Hale Olshansky

Doctor of Philosophy in Chemistry

University of California, Berkeley

Professor A. Paul Alivisatos, Chair

Harnessing the energy in photoexcitations requires efficient and controlled charge separation whether to drive a photochemical reaction or to create electricity for a photovoltaic device. Semiconducting nanocrystals, or quantum dots, have shown particular promise as light absorbers for these applications. They possess large extinction coefficients, size-tunable band gaps, and an accessible and functionalizable surface. The accessibility of the surface not only enables efficient charge extraction, but it also allows for undesirable charge trapping on ill-defined surface states. This dissertation will explore the mechanism of charge transfer from photoexcited quantum dots in order to better understand both charge extraction and trapping. It is specifically focused on hole transfer by using hole-accepting moieties since this process tends to limit the efficiency of quantum dot based devices and is understudied compared to electron transfer.

A model system for studying hole transfer is presented that uses cadmium selenide/cadmium sulfide core/shell nanocrystals or quantum dots with high photoluminescence quantum yields, which therefore selects dots with relatively few traps. The surface of these quantum dots are functionalized with ferrocene-derived hole-accepting molecules and the effect of this functionalization on the photoluminescence is used to determine the rate constant for hole transfer. The rates are found to exponentially decay with increasing CdS shell thickness or increasing linker length between the ferrocene and the quantum dot surface. This is well modeled by a tunneling process.

The relationship between driving force and rate in this system was investigated by using six distinct ferrocene acceptors with a range in driving force of 800 meV. The resulting relationship between rate and energetic driving force for hole transfer is not well modeled by the standard two-state Marcus model. Alternative mechanisms for charge transfer are posited, including an Auger-assisted mechanism that provides a successful fit to the results. The observed relationship can be used to design QD-molecular systems that maximize interfacial charge transfer rates while minimizing energetic losses associated with the driving force.

The temperature dependence of the hole transfer rate in this model system is also explored. The observed Arrhenius slopes for these rates do not depend on driving force, which suggests that surface state mediated hole transfer may dominate direct hole transfer. A model for trap-mediated transfer via shallow and reversible hole traps is posited and matches well with the data.

Finally, the results presented within are used to inform the creation of a generalizable model for hole transfer through which previously published work on hole transfer to both engineered and native hole traps can be analyzed.

Acknowledgements

I am thankful that I was able to spend the last five years living and working in the city of Berkeley and being a part of the College of Chemistry. It is a wonderful place to live and the sense of community within the Chemistry department often makes me feel like I am at a small liberal arts college.

I would like to thank my advisor, Professor Paul Alivisatos, for truly caring about my development as a scientist and as a contributing member of society. He encouraged me to think independently and deeply about my research, while always trying to keep the bigger picture in mind. He has had a profound impact on the way I think about and approach scientific questions.

I would also like to especially thank Professor David Chandler for his role as a pedagogical mentor during the two classes I served as his teaching assistant. His energy and sharpness during lecture were inspiring. His lessons gave me a deep appreciation for the ability of statistical mechanics to explain much of the world around me.

I would like to thank all of the other members of the Alivisatos lab that I have overlapped with, both past and present. Just to name a few: Yogi Surendranath and David Grauer for providing me with mentorship in my first year. Hoduk Cho, Justin Ondry, and Brandon Beberwyck for their companionship as TEM supervisors. Nima Balan, Youjin Lee, and David Nenon for showing me that you can learn as much from the students that you mentor as they learn from you. Finally, I would like to specially thank Tina Ding for being my scientific partner in crime throughout the majority of my PhD. She also did the majority of the work presented in Chapter 2.

I would like to thank my parents, both UC Berkeley graduates, for encouraging me to come here in the first place and for providing moral support along the way.

Table of Contents

List of Figures

List of Tables

Chapter 1 : Introduction

1.1   Motivation for studying charge transfer in quantum dots

Understanding the dynamics of charge carriers in photoexcited quantum dots (QDs) is an integral part of both designing new and refining existing QD-based technologies. These applications almost exclusively rely on efficiently harnessing the energy stored in an excited electron-hole pair either through radiative recombination or through charge separation to produce chemical or electrical work (Figure 1.1). To date, the majority of commercially viable applications rely on the former process. The sharp fluorescent line-widths, photostability, and color-tunability of QDs have led to their use in bio-imaging[1,2] and display technologies.[3] QDs have also shown great promise as potential light absorbers in photovoltaic[4-7] (electrical work) and photocatalytic[8-10] (chemical work) devices that rely on efficient charge separation. Specific photovoltaic examples include thin film QD photovoltaics[4,5] or solution junction QD sensitized solar cells.[6,11] Additionally, QD-based photocatalytic devices have been made that produce hydrogen[10,12] reduce CO_2,[13,14] or photocatalyze C-C bond formation.[15,16]

The predominance of the surface in QDs presents both desirable and undesirable consequences in advancing these technologies. The proximity of a functionalizable surface to photoexcited charges in QDs allows for efficient and controlled charge extraction, yet ill-defined and undercoordinated surface atoms (traps) can also localize these excited charges and non-radiatively dissipate their energy. Therefore, studying charge transfer from QDs to well-defined states is key to improving performance in the variety of applications listed in the previous paragraph. Resultantly, charge transfer from QDs to both molecular[17-19] and bulk states[20-22] has been extensively studied in the last decade.
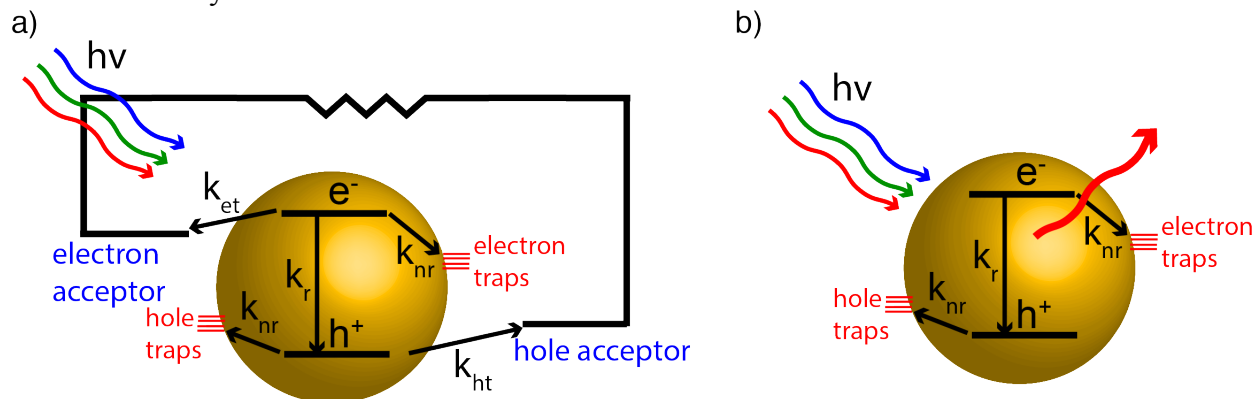
Figure 1.1. Quantum dot energy conversion. Two different mechanisms for harnessing photoexcited energy in QDs for useful applications: a) converting photons to electrical current or chemical work and b) efficiently down-converting broadband photons to a narrow emission profile. Rates of de-excitation are highlighted: electron transfer (k_{et}), hole transfer (k_{ht}), radiative recombination (k_r), and non-radiative recombination (k_{nr}) either through hole traps or electron traps.
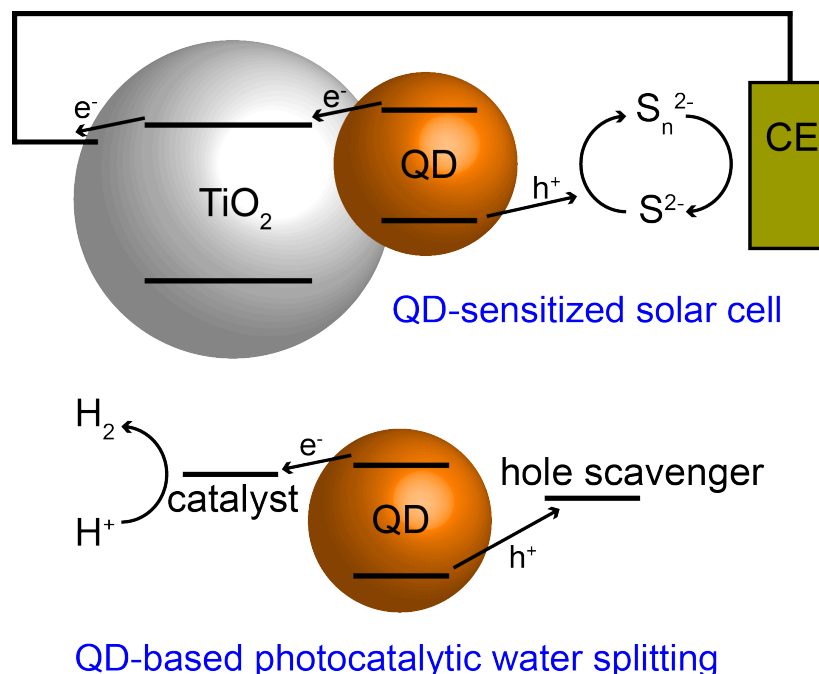
Figure 1.2. QD applications reliant on charge separation. Two promising applications for solar energy conversion using QDs. Top, QD-sensitized solar cells involve fast electron injection into n-type TiO_2, yet the hole transfer to the polysulfide/sulfide redox couple is often sluggish. Bottom, QD-based photocatalytic hydrogen evolution systems have been demonstrated for efficient proton reduction, yet their efficiencies are limited by the hole transfer to sacrificial reductants.

To motivate specifically studying hole transfer, it is worth looking at two intensely researched QD-based solar conversion schemes that rely on efficient charge separation, shown in Figure 1.2. The first scheme, QD-sensitized solar cells (QDSSCs), is an offshoot of the popular dye-sensitized solar cell, simply replacing the dye with a QD. QDSSCs have recently achieved efficiencies in excess of 11%.[11,23] In these devices, the photo-excited electron can be efficiently injected into an *n*-type metal oxide (e.g. TiO_2), however the residual hole drives oxidative photocorrosion.[6,24,25] To overcome this limitation, researchers have used blocking layers[26] and the polysulfide/sulfide[27,28] redox couple to passivate the surface of the QD, yet both of these strategies introduce new kinetic barriers to charge transfer.[29] In the second application, solar driven hydrogen evolution has been shown to efficiently reduce protons with a reported 100% conversion efficiency of photons to hydrogen.[30] While the photo-excited electrons in these systems are again sufficiently reducing to drive hydrogen evolution in the presence of a catalyst, the residual hole typically drives photocorrosion, necessitating the use of a sacrificial electron donor in order to sustain photocatalysis. The use of sacrificial donors limits the utility of the photocatalytic scheme and severely diminishes the energy stored in the net reaction. Moreover, the identity of the sacrificial donor is often the key determinant of the chemical quantum yield for photocatalysis suggesting that the rate-determining process is hole extraction from the nanocrystal rather than electron transfer to a hydrogen evolving catalyst.[9,31,32] Thus, a detailed understanding of interfacial hole transfer dynamics at semiconductor nanocrystals is a pre-requisite for the rational design of more robust and active photocatalysts and sensitizers for photovoltaics.

These applications would not only benefit from a mechanistic understanding of hole transfer, but also from an empirical relationship between the thermodynamic driving force and

the associated rate for charge transfer. The efficiency of a device will ultimately be dictated by both these quantities. The driving force for initial charge separation will necessarily reduce the potential energy output of the device, resulting in reductions in either the open circuit voltage (photovoltaics) or in the achievable chemical work (photocatalysis). Similarly, the rate for charge transfer will affect quantities such as the short circuit current (photovoltaics) and quantum efficiency (photocatalysis). Generally, one would want to maximize the rate while minimizing the potential energy loss associated with the driving force. The next sections will outline the charge transfer theories used to understand these relationships and how they can be applied to QD systems.

1.2 Marcus theory

Electron transfer processes are critical in diverse applications ranging from photosynthesis[33] and cellular respiration to emerging alternative energy technologies such as organic photovoltaics,[34] dye-sensitized solar cells,[35] next generation batteries,[36] and electrochemical fuel generation.[37] The primary electron transfer process in these systems can occur between donor and acceptor electronic states that are discrete in energy and localized in space (molecular orbitals), or spatially delocalized with a continuum of available states in energy (bands in solids or surfaces), or a compromise between these two limits. Across this spectrum, from the discrete to continuum limits of electron transfer, Marcus theory has served as a robust framework for understanding charge transfer.
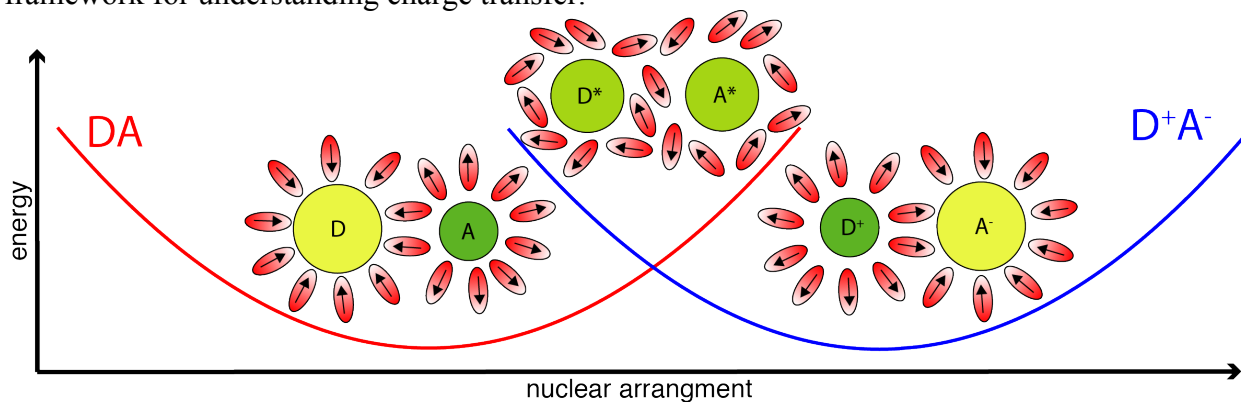
Figure 1.3. Marcus theory cartoon. Potential energy surfaces for when the electron is on the donor (red) and for when the electron is on the acceptor (blue). The electron transfers when these curves cross. The nuclear arrangement coordinate accounts for both orientation of solvent molecules (outer sphere) and nuclear re-arrangement within the donor and acceptor molecules (inner sphere).

In the discrete limit, molecular charge transfer is well described by the standard two-state Marcus model.[33,38] In this model, nuclear fluctuations are assumed to be much slower than electron transfer (the Born-Oppenheimer approximation). Therefore, the electron cannot dissipate its energy unless it transfers when the nuclei are arranged such that the electron being on the donor is isoenergetic to the electron being on the acceptor, i.e. when the curves cross in Figure 1.3. Marcus theory assumes that the potential energy surfaces that facilitate this charge transfer, one with the electron on the donor and the other with the electron on the acceptor, can be approximated with harmonic potentials. As is shown in Figure 1.3, the nuclear arrangement coordinate encompasses both rearrangement in the nuclei within the donor and acceptor (inner sphere reorganization) as well as changes in the solvent dipoles (outer sphere reorganization).

The total energy required to reorganize the nuclei from the DA to D$^+$A$^-$ conformation without transferring charge is termed the reorganization energy, which is often given the symbol λ.

The schematic in Figure 1.3 represents a case where the thermodynamic driving force ($-\Delta G_0$) for charge transfer is zero. Increasing the driving force for charge transfer has a drastic affect on the observed rate, as can be seen in Figure 1.4. The rate follows a standard Arrhenius relationship with an activation energy of $\Delta G^\ddagger$:

$$k_{et} = \nu * exp\left(-\frac{\Delta G^\ddagger}{k_B T}\right) \tag{1}$$

Where ν is a frequency factor. Therefore, the rate initially increases with increasing driving force (as $\Delta G^\ddagger$ decreases) until $\lambda = -\Delta G_0$, at which point the activation energy is zero and the rate is maximized (Figure 1.4 b,e). Further increasing $-\Delta G_0$ results in reductions in the rate and defines the inverted region (Figure 1.4 c,f).
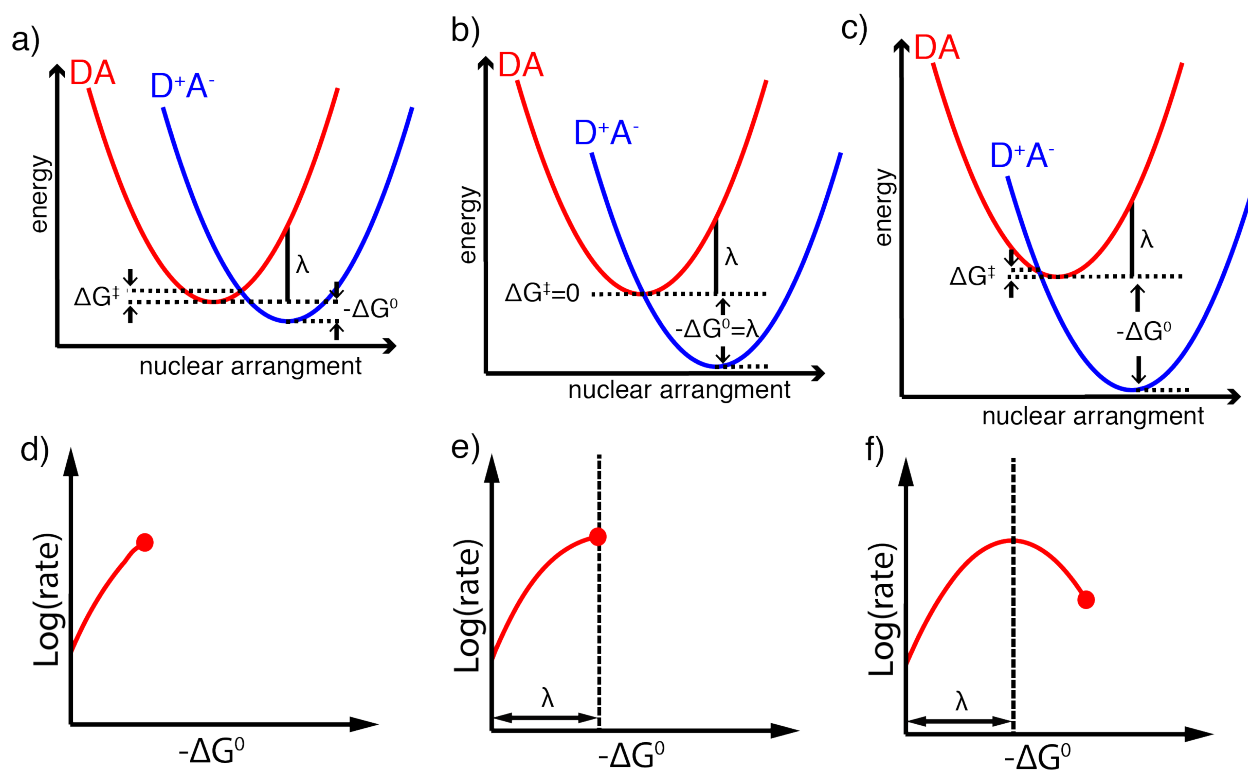
Figure 1.4. Effect of driving force on rate in Marcus theory. (a-c) Potential energy surfaces for when the electron is on the donor (red) and for when the electron is on the acceptor (blue) across a range of increasing driving forces. (d-f) The relationship between rate and driving force as the driving force is increased from left to right.

The activation energy can be redefined in terms of λ and $-\Delta G_0$, and the frequency factor can be defined based on Fermi's Golden Rule to give the commonly cited equation for non-adiabatic electron transfer:

$$k_{ct} = \frac{2\pi}{\hbar}|H_{a,b}|^2 \frac{1}{\sqrt{4\pi\lambda k_b T}} exp\left(-\frac{(\lambda + \Delta G_0)^2}{4\lambda k_b T}\right) \tag{2}$$

Where $|H_{a,b}|^2$ is the electronic coupling between the donor and acceptor. Furthermore, this electronic coupling factor has been shown to depend exponentially on the distance (d) between donor and acceptor since it is proportional to the wave-function overlap between these donor and

acceptor states. The leakage of the wave function into classically forbidden barriers allows for long-range tunneling of electrons from donor to acceptor in accordance with the following equation:

$$k_{et} \propto \left| H_{a,b} \right|^2 \propto exp\left(-\beta d \right) \tag{3}$$

Where the damping coefficient, β, is related to both the barrier height and the effective mass of the relevant charge carrier.[39]

Marcus theory can also be extended to charge transfer between molecules and semiconductors[35,40] or metallic electrodes.[41] In such cases, a continuum of either final or initial states will eliminate the Marcus inverted region, since at large driving forces a new state can always be found that maximizes the rate (Figure 1.5 c,f).[40] The continuum behavior is described quantitatively by integrating Equation (2 over the density of participating states. An intermediate charge transfer regime with multiple discretized initial or final states would necessitate a summation of Equation (2 over these states, which results in oscillations in the driving force vs. rate plot dependent on temperature, λ, and the energy level spacings (Figure 1.5 b,e). Since QDs straddle the gap between molecular and bulk, it is important to understand when it is appropriate to apply these different formulations of Marcus theory.
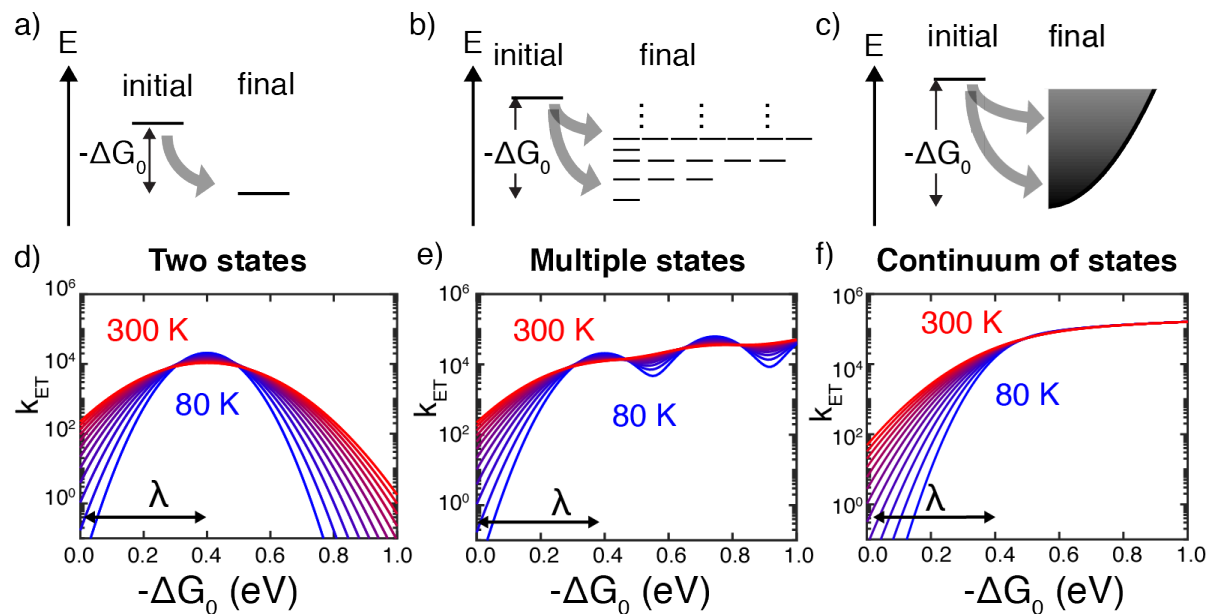
Figure 1.5. Marcus theory from two states to the continuum. Energetic diagram of (a) two state charge transfer, (b) charge transfer with multiple final states, and (c) charge transfer with a continuum of final state. (d-f) Driving force and temperature dependence of charge transfer under the three regimes presented in the top panel.

1.3   QD-molecular charge transfer

As was established in section 1.1, energy conversion in QD-based systems would benefit from a robust model for charge transfer from QDs. The previous section outlined how Marcus theory has been applied to both molecular and bulk systems, yet its application to QD systems is associated with numerous complications and unanswered questions, some of which will be outlined in this section. These uncertainties have motivated a considerable body of work on both electron[18,20,42-45] and hole transfer[19,46-50] from QDs to acceptor molecules in the last decade.

5

However, inherent heterogeneities in ensembles of QD-molecular conjugates, a limited set of tools for accurately probing the QD surface, and a lack of control in varying one parameter without also affecting other key parameters has limited our ability to chart clear mechanistic relationships such as the dependence of the rate on donor-acceptor distance and the relationship between driving force and rate. A recent review by Knowles *et al*[17] highlights much of this work and the associated difficulties in performing mechanistic studies on QD-molecular charge transfer systems.

Molecular Charge Transfer   **QD-molecular charge transfer**
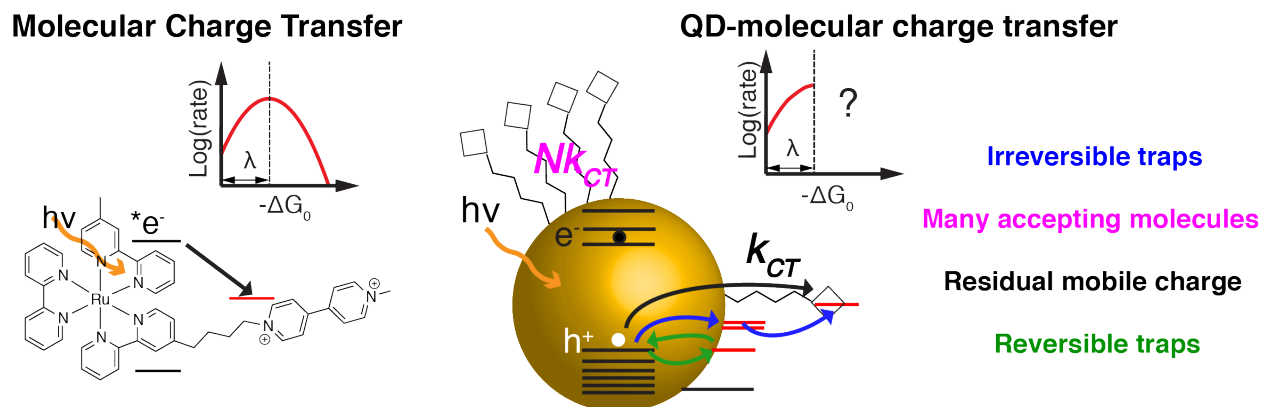
Figure 1.6. Complicating factors for studying QD-molecular charge transfer. Left, a standard molecular charge transfer system and its associated rate vs. driving force relationship given by the two-state Marcus model. Right, schematic of a QD-molecular charge transfer system and the associated complicating factors including an unknown relationship between driving force and rate.

To establish a sound model for charge transfer from QDs to molecular acceptors, we must address the features of this system that make the process more difficult to characterize than for the pure molecular case. In addition to the intrinsic intensive parameters of the Marcus model, such as the driving force, the electronic coupling between donor and acceptor, and inner-sphere and outer-sphere reorganization energies, in QDs one must also contend with a variety of complicating factors outlined in Figure 1.6. These include the possible presence of reversible and irreversible trap states of unknown energetic and spatial distribution on the QD surface, the need to precisely quantify the number of molecular acceptors attached to the QD, and the presence of a residual mobile charge in the QD core.

In cadmium chalcogenide QDs it has been shown that hole traps, typically undercoordinated chalcogen atoms, are more prevalent than electron traps and are the dominant cause of low photoluminescence quantum yields (PLQYs) in these materials.[51-53] The predominance of these ill-defined trap states can be ameliorated by growing a shell of a larger bandgap material around the QD. Although the nonradiative pathways resultant from irreversible traps are now more suppressed, the shell also electronically insulates the QD, thus erecting a barrier to charge transfer. Also of critical importance is the presence of reversible traps that can localize charge on the QD surface, but still allow for recovery of the excitonic radiative recombination. In fact, models that allow for reversible charge trapping to states energetically near the band edge have been shown to reproduce the observed temperature dependence of the photoluminescence (PL).[54-57]

Considering the number of molecular acceptors attached to the QD, another unique characteristic of nanocrystal charge transfer is that the particle can attach from one to tens of thousands of molecular acceptors, depending on the QD size. This extensive parameter *N*, the number of bound charge acceptors per QD, needs to be determined before it is possible to

6

accurately understand the effects of Marcus parameters such as driving force and coupling. In measuring N, the single donor-single acceptor charge transfer rate k_{ht}, is deconvoluted from the ensemble charge transfer rate k_{Nht} for hole transfer from the QD to any number of the surface-bound acceptors (Equation (4). In this equation, we assume that each additional hole transfer pathway is additive and independent of the other pathways of the system. At high coverage, we expect that there may be positive or negative cooperativity leading to deviations from this assumption.

$$k_{Nht} = N * k_{ht} \qquad (4)$$

Inconsistencies in the method of measurement, especially regarding reporting single donor-single acceptor charge transfer rate constants (k_{ht}) versus single donor-multiple acceptor charge transfer rate constants (k_{Nht}) leads to drastically different values for similar systems. Some groups have characterized the number of ligands bound indirectly using optical methods.[45,58] NMR, though difficult to use for a measurement of the number of ligands due to the high concentration required for its measurement, allows one to differentiate between bound versus free ligands due to their different signatures in the NMR spectrum. A variety of NMR techniques have shed light on the kinetics and makeup of the QD-ligand interface.[59]

Finally, the presence of the mobile charge in QDs has been shown to have significant effects on the excited state dynamics. The enhanced confinement in QDs results in higher Coulomb interactions between the electron and hole and weaker electron-phonon coupling, which has been known to be the cause of charge coupled intraband relaxation and other Auger-like effects in these materials.[60] For example, Klimov *et al* has found that intraband relaxation of the photoexcited electron is strongly dependent on the coupling to the hole.[61] Additionally, Auger recombination, an undesirable process in light-emitting applications that competes with biexciton radiative recombination, is 4-5 orders of magnitude higher in QDs than their bulk counterparts, and it is strongly dependent on the QD size.[62] Considering these findings, it is conceivable that Auger effects from the residual charge could also play a role in charge transfer processes.

The aim of this dissertation will be to explore and elucidate the effect of the complicating factors described in the preceding paragraphs on QD-molecular charge transfer (listed in Figure 1.6). In **Chapter 2**, I will describe a model system based on CdSe/CdS core/shell QDs with ferrocene-derived molecular hole acceptors that overcomes issues related to *irreversible traps* and demonstrates a method for accounting for the *many accepting molecules* that can be present.[50] The work in **Chapter 3** expands on this model system by exploring a larger library of ferrocene acceptors that allow one to chart the relationship between driving force and rate.[63] The results of this work provide valuable insights on the role of the *residual mobile charge* in facilitating charge transfer. In the final chapter containing original research (**Chapter 4**), the temperature dependence of hole transfer is explored within the context of the same model system. The results highlight the importance of *reversible traps* in expediting charge separation. In **Chapter 5**, the results are placed in the context of prior work on hole transfer to both engineered and native traps to provide general guidelines for assessing QD-hole transfer systems.

Chapter 2 : A model system for studying charge transfer

In this section, a model system for studying charge transfer is presented that can account for the variable number of accepting molecules and overcomes issues associated with native irreversible traps. CdSe-core CdS-shell QDs with near-unity native PLQYs are used since they significantly reduce the effect of traps that cause non-radiative recombination. The QDs are then covalently linked to well-defined hole acceptor ligands that provide the predominant PL quenching pathway. By calibrating the number of molecular hole acceptors bound to the QDs, N, using ^{1}H-NMR, the PL quenching can be monitored to extract the intrinsic hole transfer rate constant per hole acceptor, k_{ht}. Employing this technique, nine donor-acceptor systems are examined, varying shell thickness and molecular acceptor, with k_{ht} spanning over four orders of magnitude to demonstrate the highly variant effect of N on the PLQY for these systems. Importantly, this enables a mapping between donor-acceptor distance and charge transfer rate, which is interpreted in terms of the tunneling relationship in Equation (3.

The results presented in this section also clarify a topic of great inconsistency in the literature regarding the QY-N relationship. Frequently, PL intensity has been used as a direct (linear) proxy for coverage or surface binding,[64-66] yet there have also been reports that the dependence is nonlinear[67] with coverage. The current work demonstrates the general framework for determining the functional dependence on the number of acceptors.

The primary hole acceptor used in this study is ferrocene, which has a large driving force for hole transfer and has been shown to quench the fluorescence of the QDs in this system and in prior QD systems.[47] The ferrocene moieties are connected via an alkyl chain to a thiol, which displaces native oleate ligands on the nanocrystal surface and binds as a thiolate. The independent effects of hole transfer to the thiolate binding group are isolated and quantified for thorough characterization of the molecular acceptor ligand. The electronic coupling between the donor and acceptor is varied by modulating the thickness of the CdS shell and the length of the alkyl chain in the molecular acceptor. In these systems, hole transfer for a single donor-single acceptor can occur from tens of nanoseconds to hundreds of microseconds. The former is highly competitive with the native radiative lifetime of the nanocrystal while the latter is completely ineffective at extracting charge on a one-acceptor basis. However, a large number of molecular acceptors compensates for those systems with a low intrinsic k_{ht} relative to k_r to make the total hole transfer rate, Nk_{ht}, still very effective for extracting photoexcited holes in many of these systems. In these experiments, we address the unique characteristics of nanocrystal charge transfer that have been discussed in the preceding paragraphs, to show that these subtle parameters can have significant effects on the efficiency for hole transfer, an important consideration in photochemical energy conversion.

2.1   Description of donor-acceptor system

CdSe (3.9 nm diameter) with 3 monolayer (ML), 5ML, and 7ML CdS shells (Figure 2.1c-f) were synthesized, and their absorbance and fluorescence spectra are plotted in Figure 2.1a. The PLQYs and radiative rate constants, k_r, for these nanocrystals are 79.2%, 86.2%, 91.2%, and 0.044, 0.031, 0.021 ns^{-1}, respectively. The decreasing values of k_r as a function of increasing particle size are expected as a result of the electron delocalization through the larger volumes,

resulting in reduced wavefunction overlap with the hole that remains localized in the CdSe core.[68]
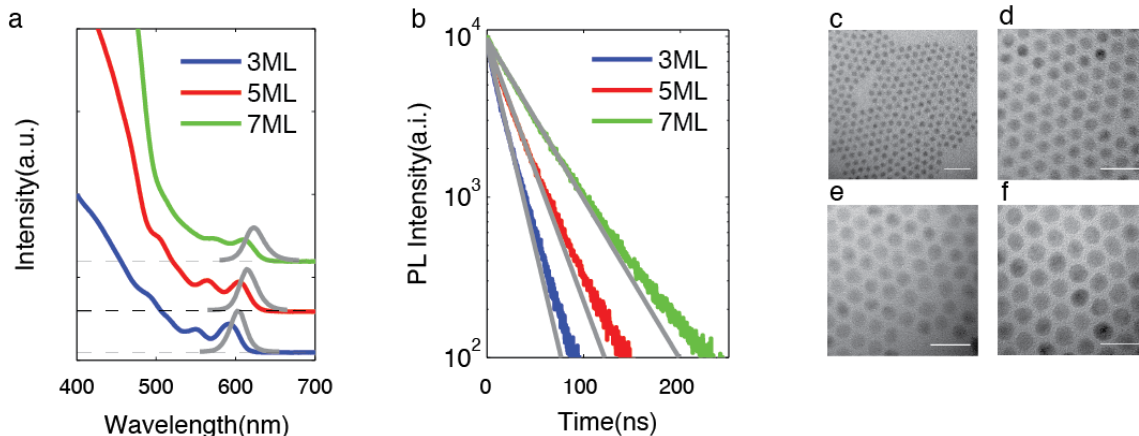
Figure 2.1. Optical and morphological characterization of QDs. (a) Absorption (solid) and photoluminescence (grey) of QDs synthesized with the same 3.9 nm CdSe corewith 3ML, 5ML, and 7ML CdS shells. (b) Photoluminescence lifetime of the three core/shell particles with their respective single exponential fits (grey). (c-f) Transmission Electron Microscopy images of the (c) CdSe core, and (d-f) the three core/shell particles. Scale bar is 20 nm.

Hole transfer is reported from the CdSe core to acceptors covalently linked to the nanocrystal surface via the thiolate binding group (Figure 2.2). The hole acceptor used is ferrocene, whose oxidation potential lies approximately 750 meV above the valence band of the CdSe core based on electrochemical and computational studies.[49] The energetics will be discussed in greater detail in Chapter 3. The possibility of resonance energy transfer is precluded due to the lack of spectral overlap of the ferrocene absorption with QD emission. The large thermodynamic driving force for photoinduced hole transfer allows this process to compete with native radiative recombination, reflected in the measured PL and PL lifetime. However, the hole transfer rate is most sensitive to modulations in the electronic coupling, achieved by varying the thickness and composition of the barrier material between the CdSe core and the acceptor. The donor-acceptor distance is well-defined in this model system, achieved by using a nearly-spherical nanocrystal morphology and acceptors that contain a well-characterized binding group. This expected well-defined distance is further verified by using two ferrocene ligands with different alkyl chain lengths, 3-ferrocenylpropanethiol (FcC_3SH) and 6-ferrocenylhexanethiol (FcC_6SH), to demonstrate that the charge transfer rate constants match the expected tunneling through saturated alkyl chains. The effects of the thiolate on the measured hole transfer rate is examined by using a thiol alkyl ligand with an NMR tag: 11-(1H-pyrrol-1-yl) undecane-1-thiol (PyrrSH). Although the pyrrole group has a 100 meV driving force for hole transfer, the eleven carbon chain distance precludes pyrrole oxidation from being a significant hole transfer pathway, as the already low rate associated with the weak driving force is now diminished completely by an exponential drop-off in the rate across such a large distance. Therefore, PyrrSH is referred to as AlkylSH in the rest of this chapter and functions as a control for examining hole transfer to surface thiols, a well-known shallow hole trap for CdSe materials.[69]
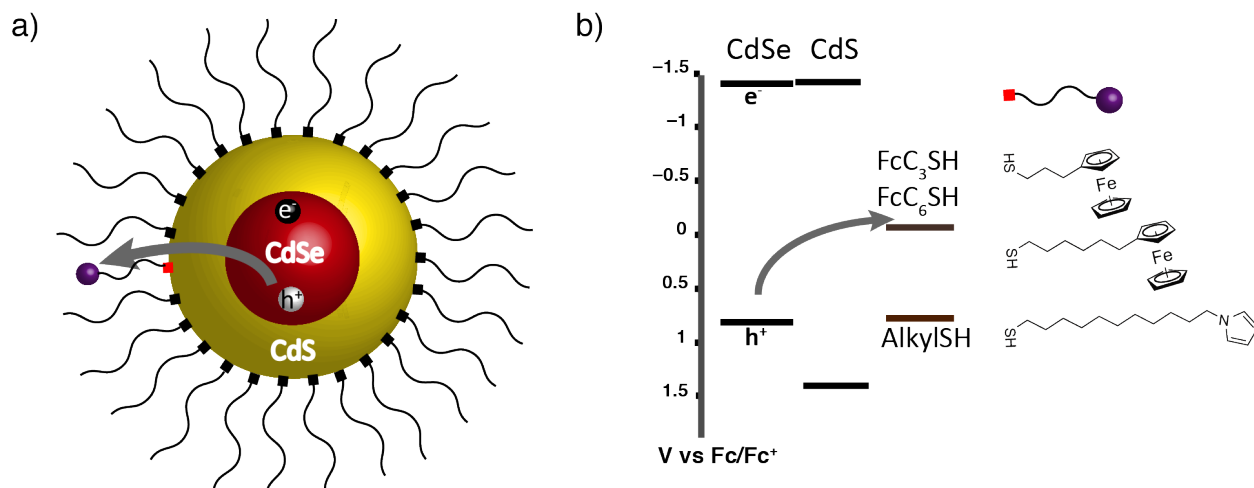
Figure 2.2. The model donor-acceptor system. (a) Illustration of the donor-acceptor system. The hole donor is at the CdSe core, and the acceptor is localized at the end of the ligand chain. (b) Energy positions of the conduction and valence bands of CdSe and CdS and the oxidation potentials of FcSH and AlkylSH.

The donor-acceptor system was prepared by a controlled ligand exchange of FcC$_3$SH, FcC$_6$SH, or AlkylSH with the native oleate ligand. By varying the concentration of added functional thiols, QDs with a range of coverages were prepared and their QYs measured. ICP atomic emission spectroscopy (see Appendix) combined with quantitative ^{1}H NMR[70] was used to determine the number of bound ligands per nanocrystal, *N*, whether it be native oleic acid, FcC$_3$SH, FcC$_6$SH, or AlkylSH. All ligands measured here have spectrally resolved signatures in ^{1}H NMR that allow for facile quantification. A schematic of the ligand exchange is shown in Figure 2.3 along with example ^{1}H NMR spectra used for quantification. It should be noted that surface bound species exhibit dramatically broadened peaks with widths 50-100 Hz.[50,59,67,71] This makes them easy to distinguish from species free in solution; however, the broadening complicates one's ability to accurately quantify the bound peaks. Any protons in the crowded methyl and methylene regions shifted by 1-3.5 ppm are often too convoluted for accurate quantification. Typically, resonances downfield from 4 ppm are easier to quantify such as the protons on the alkene of oleic acid at 5.3 ppm.[67,71]

^{1}H NMR spectra of the surface of native nanocrystals suggest that both bound oleate (the coordinating ligand in the Cd precursor) and octadecylphosphonate (ODPA, the CdSe core's surface ligand) are bound since the ratio of alkene protons to alkane protons is too low for just oleate. ODPA has been shown to form very strong bonds on chalcogenide nanocrystal surfaces,[71] and therefore ODPA is a strong competitor for the surface of the final core-shell nanocrystal despite its overall lower concentration in the growth reaction. Phosphorus NMR was performed to verify the presence of ODPA on the surface of the core/shell QDs. A semi-quantitative method was employed to collect ^{31}P NMR spectra of both native QDs and FcC6SH exchanged QDs by using identical concentrations, as monitored by optical absorption, and identical collection parameters for the two spectra (Figure 2.4). Proton NMR showed a 2:1 ratio of FcC$_6$SH to oleic acid on the exchanged QDs, indicating that significant exchange has occurred. Integration of the ^{31}P NMR peaks associated with bound ODPA show a 25% reduction in ODPA from native QDs to FcC$_6$SH QDs. Therefore, the ligand exchanges presented in this work are primarily thiols replacing oleic acid on the surface, yet residual ODPA also participates in exchange to a much smaller extent. Furthermore, the presence of a consistent number of bound ODPA molecules (originating from the core ligands) in the synthesis of these core-shell nanocrystals with three

shell thicknesses results in a deviation in the total number of bound oleic acids for the three sizes from what is predicted based on their surface area.
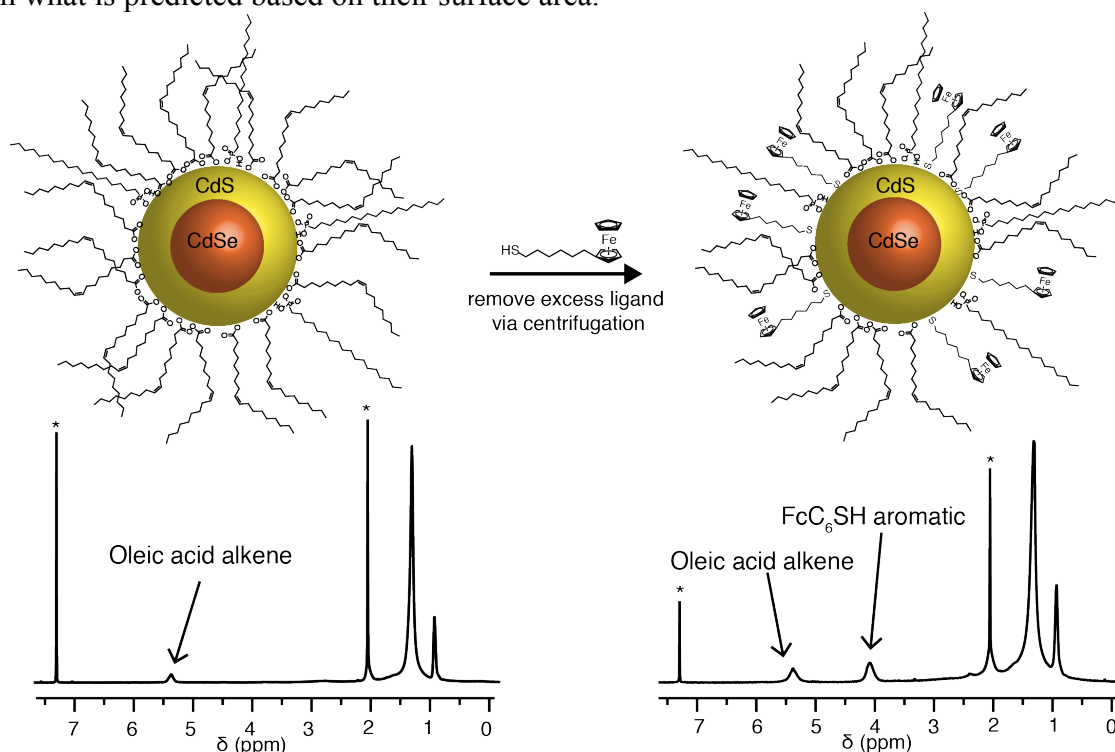
Figure 2.3. Schematic of ligand exchange, monitored by NMR. Top, schematic of the ligand exchange that replaces oleic acid with FcC_6SH on the QD surface. Bottom, representative ^1H NMR spectra of the native and ligand-exchanged QDs, highlighting the regions used for quantification (4-5 ppm).
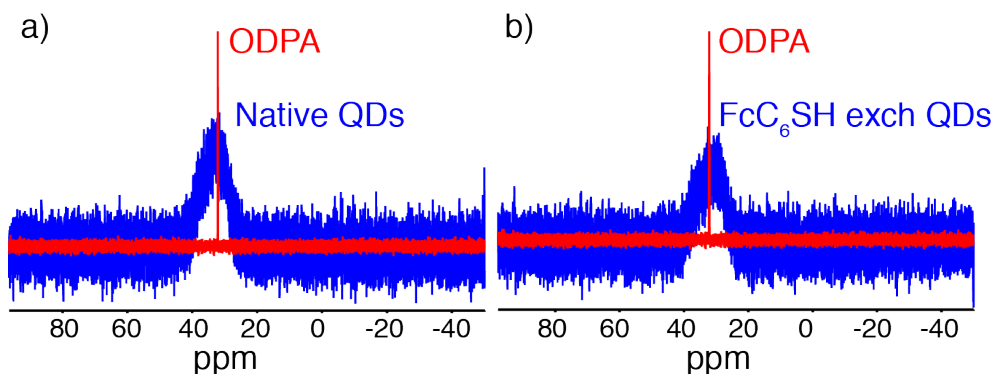
Figure 2.4. ^{31}P NMR spectra of native and ligand exchanged QDs. ^{31}P NMR spectrum of free octadecylphosphonic acid (ODPA) in tetrahydrofuran- d_8 (red) and CdSe/CdS core/shell QDs in chloroform-d (blue). It is apparent that ODPA is present on both (a) native QDs and (b) FcC6SH exchanged QDs.

2.2 Measuring hole transfer rates

The QD PLQY as a function of N across nine donor-acceptor systems with k_{ht} spanning over four orders of magnitude is shown in Figure 2.5. The nine k_{ht} values were controlled by electronic coupling, which is modulated by varying the thickness of the CdS shell and the alkyl chain length of the ferrocene hole acceptor, both of which act as tunneling barriers for the holes that are energetically confined to the CdSe core. The nine systems represent all permutations

possible from the three donor nanocrystals and three acceptor molecules used in this study, allowing quantitative comparison of rates across different coupling regimes.

$$PLQY = \frac{k_r}{k_r + k_{nr} + Nk_{ht}} = \frac{k_r}{k_{tot}} \qquad (5)$$
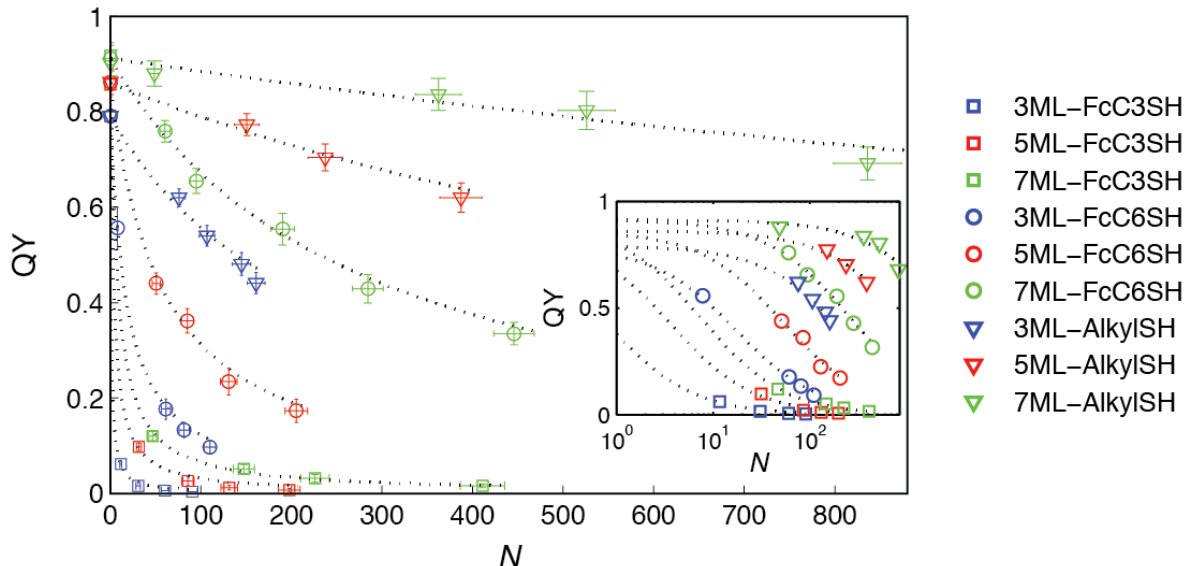
Figure 2.5. PLQY vs. *N* for nine donor-acceptor systems. The nine donor-acceptor systems are composed of the three donor QDs with 3, 5, or 7 ML CdS shell thicknesses and the three acceptor molecules: FcC_6SH, FcC_3SH, and AlkylSH. Inset: the same data and fits plotted on a logarithmic scale for *N* to give a better representation of the effect of low *N*.

The raw data (QY, *N*) of each of the nine systems is fit to Equation (5, which describes the QY as a function of the rate constants of all the pathways of the photoseparated charges and *N* to yield the hole transfer rate constant per acceptor, k_{ht}, for that given system. The fit uses the radiative rate constant, k_r, and the nonradiative rate constant, k_{nr}, that have been determined for the native QD from PLQY and fluorescence lifetime measurements (Figure 2.1b). The lifetime data fit well to single exponentials (Figure 2.1b) across the highest two decades of intensities, as expected from these core-shell materials, and the fit is used to determined k_{tot}. The raw data and their respective fits are plotted together in Figure 2.5. The same relationship plotted on a logarithmic scale for *N* is shown in the inset, allowing for better visualization of the expected quenching when *N* is less than 10, which is significant for the systems containing FcC_3SH as the acceptor. The fits in Figure 2.5 agree well with the data across the nine different systems even at high coverage, thereby confirming the validity of Equation (4. For these systems, the presence of ODPA on the QD and the weaker packing efficiency of the ferrocene ligands relative to the native oleic acid molecules prevent the QD from achieving the intimate ligand interactions on the surface that may lead to cooperativity.

2.3 Electronic coupling and charge extraction efficiency

Table 2.1 tabulates the values of k_r, k_{ht}, OA_o (number of native oleic acid per QD), N_{max}, $N_{max}k_{ht}$, and the maximum hole transfer quantum yield (*HTQY*) (Equation (6) for the nine systems depicted in Figure 2.5. N_{max} is the maximum number of hole accepting ligands that were

experimentally measured in the respective system, and it corresponds to approximately the maximum number of ligands that could be exchanged by mixing at room temperature. As shown in Table 2.1, N_{max} depends on the size of the QD and the length of the alkyl chain of the acceptor.

$$HTQY(N) = \frac{Nk_{ht}}{k_r + k_{nr} + Nk_{ht}} = \frac{QY(N)}{QY(N = 0)} \qquad (6)$$

$HTQY_{max}$=$HTQY(N_{max})$ represents the maximum charge extraction yield achieved at the highest coverage, N_{max}. The nanocrystal systems with FcC$_3$SH achieve $HTQY_{max}$ of 97%-99.5%. In the fastest of these systems (**1a**), a native luminescence QY of 82% is reduced to a luminescence QY of only 0.5% by approximately 91 FcC$_3$SH ligands on the surface. k_{ht}, the hole transfer rate constant per acceptor, on the other hand, varies from 63 μs^{-1} for hole transfer from the 3ML QD to the FcC$_3$SH molecule to 3 ms^{-1} for hole transfer from the 7ML QD to AlkylSH.

	Donor-Acceptor	$k_{ht}(ns^{-1})$	OA_o	N_{max}	$N_{max}k_{ht}(ns^{-1})$	$k_r(ns^{-1})$	$HTQY_{max}$
1a.	3ML-FcC3SH	0.063×10^0	198	91	5.7	0.044	99.5%
1b.	5ML-FcC3SH	0.010×10^0	413	197	2.0	0.031	99.1%
1c.	7ML-FcC3SH	0.026×10^{-1}	890	404	1.05	0.021	96.2%
2a.	3ML-FcC6SH	0.033×10^{-1}	198	110	0.36	0.044	86.5%
2b.	5ML-FcC6SH	0.094×10^{-2}	413	207	0.19	0.031	84.0%
2c.	7ML-FcC6SH	0.079×10^{-3}	890	446	0.035	0.021	60.3%
3a.	3ML-AlkylSH	0.028×10^{-2}	198	161	0.050	0.044	47.1%
3b.	5ML-AlkylSH	0.035×10^{-3}	413	387	0.018	0.031	33.1%
3c.	7ML-AlkylSH	0.078×10^{-4}	890	836	0.0033	0.021	12.5%

Table 2.1. Tabulated data for the nine donor-acceptor systems. Rate constants, surface ligand characterization, and $HTQY_{max}$ of the nine donor-acceptor systems plotted in **Figure 2.5**. The hole donor is the CdSe core of the QD with the specified shell thickness in ML.

Hole transfer rates to the AlkylSH ligand are about 10% as fast as the hole transfer rates to the ferrocene ligands with thiolate binding groups. Therefore, charge trapping to the thiolate binding group can be excluded as a convoluting or competitive pathway for hole transfer in the ferrocene donor acceptor systems. However, assuming the total charge transfer to be a sum of both pathways, this reduces the hole transfer rates reported in Table 2.1 by about 10%. In this experiment, the larger band gap CdS shell has a high enough energy barrier such that the hole transfer to intrinsic nonradiative pathways and low-driving force traps like thiols is ineffective, while at the same time being weak enough so that tunneling to a high driving force acceptor such as ferrocene is effective. This thereby demonstrates that one can use QD heterostructure design to strike a balance between mitigating undesirable traps while still being able to extract charge efficiently to well-defined desirable traps.

In Table 2.1, it is worth noting that k_{ht} and $HTQY_{max}$, together comprehensively describe the effectiveness of nanocrystal charge transfer. More specifically, k_{ht} depicts the individual charge transfer efficiency of each ligand while $HTQY$ (Equation (6) is the efficiency of the entire QD system to extract the photogenerated hole from the core to the surface. Therefore, $HTQY$ includes contributing factors from the competing pathways of k_r and the number of acceptors bound, N. While k_{ht} is an intrinsic parameter that can be compared to the theory of charge transfer, $HTQY$ is an extensive empirical value with implications for applications in energy conversion, with $HTQY_{max}$ representing the charge transfer efficiency limit of a QD-molecular system at maximum acceptors bound. Both are essential for understanding nanocrystal charge transfer.

2.3.1 k_{ht} for reliable comparisons between systems to examine electronic coupling

The k_{ht} values obtained in the previous section allow for an accurate investigation into the effects of coupling under calibrated conditions. The distance dependence of the charge transfer rate constant is given by Equation (3, described in Chapter 1. By varying the shell thickness and obtaining the resulting k_{ht}, the damping coefficient (β) can be determined for hole transfer through CdS. Figure 2.6a shows the plot of the logarithm of k_{ht} as a function of the thickness of CdS for the FcC_3SH, FcC_6SH, and AlkylSH systems, yielding β for hole transfer of (0.22 ± 0.032) Å^{-1}, (0.26 ± 0.022) Å^{-1} and (0.25 ± 0.021) Å^{-1}, respectively. The values are within error of one another, yielding an average β of (0.24 ± 0.025) Å^{-1}, which is similar to electron transfer through conjugated carbon chains with reported β values of ~0.2 Å^{-1}. A higher β indicates weaker coupling, or higher tunneling barrier, since the rate drops off at shorter distances. Previous work on charge transfer on semiconductor nanocrystal heterostructures has measured β of 0.91 Å^{-1} for hole transfer through ZnS in a CdSe/ZnS system,[43] albeit without directly measuring the number of ligands. As the valence band of ZnS lies lower in energy than that of CdS, we expect the lower CdS barrier to result in higher coupling between the donor and acceptor, hence a lower β, which agrees with the experimental results.

a)

b)
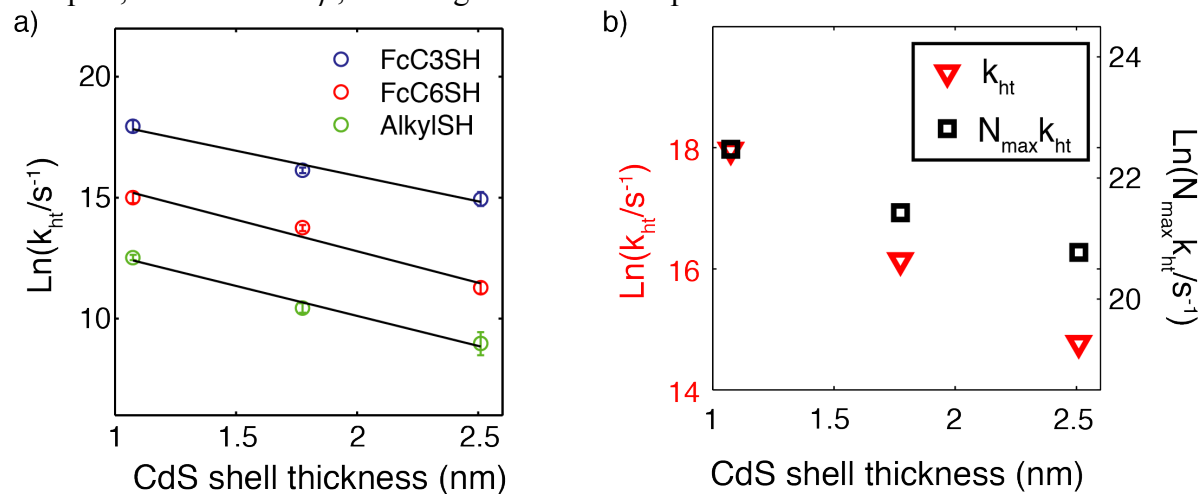
Figure 2.6. Effect of CdS shell thickness on hole transfer rate. (a) The natural log of the rate as a function of shell thickness is plotted for each of the acceptor molecules. Hole transfer through CdS yields an average β of (0.24 ± 0.025) Å^{-1}. (b) Comparison of k_{ht} and Nk_{ht} as a function of the three shell thicknesses for hole transfer to FcC_3SH. At larger sizes, N_{max} increases as the square of the radius thereby lessening the magnitude of the decrease in total hole transfer rate.

To extend this analysis, the β for hole transfer through the saturated carbon bonds of the ferrocene ligand could be determined by comparing the k_{ht} for FcC_3SH versus FcC_6SH. This yields β of ~(0.85 ± 0.1) Å^{-1}, which falls within what has been experimentally measured for saturated carbon chains in literature.[72] These two β measurements together indicate that the donor-acceptor distance is well defined in the QD charge transfer system presented in this chapter.

Furthermore, these β values can be used to predict the k_{ht} for hole transfer from bare CdSe QD to acceptors that are separated from the surface by a single bond. For CdSe core size diameter of 3.9 nm containing approximately 30 acceptor ligands, we predict a single hole transfer time constant of about 200 ps and a total hole transfer rate below 10 ps. This value is comparable to that seen by Sykora *et al* for hole transfer from CdSe to various Ru-polypyridine

complexes with similar driving force and similar donor-acceptor distance as the system presented in this chapter.[19] However, it is faster than the 2.5 ns rate measured for hole transfer from CdSe to phenothiazine physisorbed to the surface in a 1:1 donor-acceptor mixture,[46] which agrees with findings that electronic coupling via van der Waals forces is much weaker than those achievable through covalent interactions.

2.3.2 HTQY and the possible advantages of multiple acceptors

The QD itself is stable upon electronic excitation because one quantum of electronic excitation is distributed over thousands or even tens of thousands of atoms. When hole transfer takes place for a system with one molecular acceptor, the charge is now confined within just the few atoms of the molecular acceptor. The molecular acceptor is therefore more likely to degrade by charge transfer dynamics before the QD does. This is the root cause of the enhanced photochemical stability of QDs over molecular chromophores. Yet by balancing rates and the number of ligands, we show that it is possible to assemble one QD with hundreds of molecular acceptors so that the degradation of one acceptor will not render the entire system inactive for further hole transfer. The ability to distribute the probability of hole transfer into many acceptors on the surface may be a strategic advantage of nanocrystal systems. Additionally, by using a molecule with a well-defined redox potential, specificity is achieved in the driving force for hole transfer. The high number of hole transfer pathways in these systems therefore provides a means by which charge transfer can occur both effectively, persistently, and specifically.

In molecular systems commonly made of a single donor and a single acceptor, the charge transfer rate k_{ct} must outcompete the native recombination pathways to be effective. For example, electron transfer from $[Ru(bpy)_3]^{2+}$ to methyl viologen is effective because the electron transfer time constant of tens of nanoseconds is much faster than the microsecond triplet lifetime of the sensitizer. Table 2.1 shows that in the QD-molecular systems, only in system **1a** does the k_{ht} (63 μs^{-1}) surpass k_r (44 μs^{-1}). In this system, with contributions from approximately 91 acceptor ligands, the $N_{max}k_{ht}$ of the system reaches 5.8 ns^{-1}, or a total time constant of 170 ps, which is more than two orders of magnitude faster than the 23 ns radiative lifetime of the QDs with a 3ML shell. The $HTQY_{max}$ for this system is approximately unity.

On the other hand, for six out of the nine donor acceptor systems studied here, the k_{ht} is one to over four orders of magnitude slower than k_r. This highlights one of the important advantages of QD charge transfer as a single donor-multiple acceptor system. The addition of more acceptors can compensate for the intrinsically low k_{ht} as compared to k_r, as is the case for the systems **2a**, **2b**, **2c**, and **3a**. Although a thicker shell lowers the rate of hole transfer, the number of acceptors that can be accommodated on this larger QD grows as the square of the radius. Therefore, $N_{max}k_{ht}$ does not drop off at the same magnitude as k_{ht} over the same coupling distance, as shown in Figure 2.6b. Additionally, k_r, the competitive pathway for charge recombination, is a tunable parameter that also affects the efficiency of hole extraction in these system, as it approximately doubles from the 7ML QD to the 3ML QD.

To illustrate this point further, system **3a** has a higher k_{ht} but a lower $HTQY_{max}$ than system **2c**. System **3a** is more effective as a single donor-*single* acceptor system, with a faster k_{ht}, but system **2c** is more effective as a single donor-*multiple* acceptor system. System **2c** is able to accommodate almost three times as many ligands as system **3a** and thus it is able to achieve a higher total charge transfer rate $N_{max}k_{ht}$ and therefore a higher $HTQY_{max}$. Additionally, its k_r is slower than that of system **3a** making it easier for hole transfer to outcompete native recombination pathways. Similarly, systems **2a** and **1c** depict the same trend, representing another example that highlights this behavior.

AlkylSH is able to achieve the highest maximum coverage (Table 2.1) for the same QD size because the pyrrole group comfortably occupies the spatial volume at a distance that is eleven carbon molecules from the QD surface. On the other hand, FcC_6SH with its six carbon linker and FcC_3SH with its three carbon linker are more kinetically inhibited to bind at higher coverages due to the steric effects of the cyclopentadiene rings at these close distances from the QD surface. Additionally, the maximum achieved coverage is greater for FcC_6SH than FcC_3SH, as expected. Similar to the effects seen in CdS, a higher N_{max} afforded by the longer chain length linearly improves the total hole transfer rate $N_{max}k_{ht}$ as a result of improved packing; k_{ht} on the other hand drops exponentially over this distance due to the weaker electronic coupling at this longer chain length. Notably, the larger β (0.8Å^{-1}) of the alkyl chain than that of the CdS shell (0.25Å^{-1}) indicates that N_{max} achieved by modulating the chain length plays a smaller role in counteracting the effect of electronic coupling. The effect on a plot of $N_{max}k_{ht}$ in Figure 2.6b versus shell thickness will be less pronounced for the ligand shell than the inorganic CdS shell.

Both total $HTQY$ and k_{ht} are important in the characterization of nanocrystal charge transfer. While k_{ht} allows one to accurately compare systems as a function of variation in the parameters of charge transfer theory, $HTQY$ reflects the efficiency of the entire system to extract the hole to the surface. $HTQY_{max}$ represents the best charge transfer efficiency one can obtain from such a QD system. Therefore, the often-overlooked factors of k_r and N can have a significant effect on charge transfer efficiency.

Chapter 3 : The relationship between rate and driving force

In section 1.1, the merits of determining the relationship between driving force and rate for hole transfer from photoexcited QDs were discussed in the context of designing better QD-based solar energy conversion schemes. The difficulties of creating this systematic relationship in QD-molecular systems were also discussed in section 1.3. Complicating factors such as ill-defined binding of acceptor molecules, the lack of an accurate measure of N, and competition from native traps have all limited researchers' ability to determine the relationship between driving force and rate. However, the model system described in Chapter 2 has provided a means to overcome these limitations.

This chapter expands on that model system by using a series of ferrocene-derived hole accepting molecules that allow for the hole transfer rate to be charted as a function of driving force. To achieve modulation in driving force, the cyclopentadiene rings of ferrocene were synthetically modified with electron withdrawing and donating groups that tune the oxidation potential of the molecule by approximately 800 meV, spanning a driving force range of 150 to 950 meV. The well-defined nature of this donor-acceptor system, as demonstrated in Chapter 2, allows for driving force tunability without significantly changing other parameters of the system that may affect the rate constant. Specifically, the size of the QD core, the linker length, and the head group of the ligand within this system are held constant. The present work demonstrates the first systematic study of the relationship between rate and driving force for hole transfer from photoexcited QDs.

3.1   The Auger-assisted model for QD charge transfer

A handful of systematic studies on QDs relating *electron* transfer rates to driving force have been reported, all of which report Marcus behavior in the normal regime.[20,44] The groups of Lian and Prezhdo recently published a comprehensive experimental study mapping the relationship for the electron transfer rate as a function of driving force using CdTe, CdSe, and CdS QDs of varying size coupled with three distinct molecular acceptors, covering a larger range in driving force than has previously been probed.[44] The primary mode for controlling driving force in many of these studies relies on changing the QD size and thus also the conduction band energy. However, this makes it difficult to control the changes in electronic coupling, since one would expect smaller QDs to be more efficiently coupled to surface bound acceptors. The work from the groups of Lian and Prezhdo accounted for this variation with an effective mass model that normalized the electronic coupling factor to electron density on the surface of the QD.[44]

Lian and Prezhdo's showed no inverted regime for electron transfer, with the charge transfer rate constant saturating at the highest driving forces. Lian and Prezhdo postulated that the energy lost as the electron transfers to the molecular acceptor is coupled to the excitation of the residual hole in the valence band, similar to the Auger effect responsible for nonradiative recombination in systems with an extra charge. A schematic of this process is shown in Figure 3.1. Electron transfer coupled with hole excitation allows the rate to stay high at large driving force since there are many potential final states associated with hole excitation, one of which will have a driving force near the barrierless region (Figure 1.5). They found that their data fits well to this proposed model.
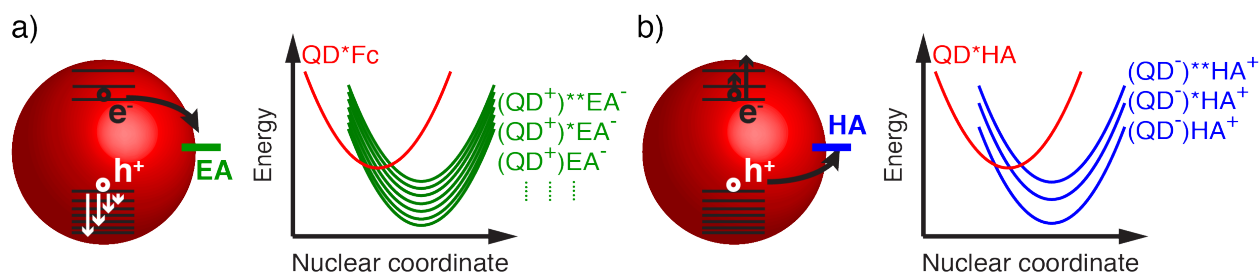
Figure 3.1. Schematic of Auger-assisted charge transfer. (a) Electron transfer from a photoexcited QD to an electron acceptor (EA, green). The multitude of final potential energy states result from the many available hole excited states in cadmium chalcogenide QDs. (b) Hole transfer from a photoexcited QD to a hole acceptor (HA, blue). The final states are more discretized to reflect the larger energy spacing of electron levels in the conduction band.

The analogous hole transfer, however, may deviate from this behavior for a few reasons. First, the electron density of states is significantly lower than the hole density of states in cadmium chalcogenide QDs. Although it should be noted that according to the Auger-assisted model, the electron density of states for our system is still large enough to eliminate any inverted region dynamics at room temperature. Second, since there is still no spectroscopic evidence for core charge excitation during charge transfer, another possibility is that the Auger-assisted model is operating via excitation of trapped charges. Therefore, the differing trap state densities of electrons and holes would affect the results. Finally, the electronic coupling between initial and final states in the Auger-assisted model will certainly change for hole transfer coupled with electron excitation. We seek to experimentally determine the existence of this Auger-assisted behavior for hole transfer by systemically mapping the rate constant of hole transfer as a function of driving force.

3.2   Hole acceptors with systematically variable driving force

Five ferrocene derivatives with oxidation potentials spanning 800 meV in energy were synthesized (Figure 3.2). The redox potentials were controlled by modification of the cyclopentadienyl rings with either electron donating or withdrawing groups. In this study, the electron-withdrawing group was bromine, which was found to lower the energy of the highest occupied molecular orbital (HOMO) on ferrocene by approximately 130 meV per additional bromine, in accordance with previous literature results.[73] To achieve higher HOMO energies, electron donating methyl substituents were employed. Higher HOMO energies will correspond to larger driving forces for hole transfer from the QD to the ferrocene. All the ligands were synthesized with a six-carbon linker and a thiol binding head to covalently attach to the surface of the QD. Five ligands were synthesized starting with either 1,2,3-tribromoferrocene (Br$_3$Fc), 1,2-dibromoferrocene (Br$_2$Fc), bromoferrocene (BrFc), ferrocene (Fc), or bis(tetramethylcyclopentadienyl)iron (Me$_8$Fc). Of these, BrFc, Fc, and Me$_8$Fc were available commercially while Br$_2$Fc and Br$_3$Fc were synthesized from BrFc.

The linker group and binding head were added to Br$_3$Fc, Br$_2$Fc, BrFc, Fc, and Me$_8$Fc via a Friedel-Crafts acylation with 6-bromohexanoyl chloride followed by a thiolation[74] (Figure 3.2). As expected, owing to the electron-withdrawing nature of bromine, the acylation occurred on the cyclopentadienyl ring that had not been brominated in the cases of BrFc, Br$_2$Fc, and Br$_3$Fc. This observation was confirmed by ^{1}H NMR. It should also be noted that the Me$_8$Fc synthesis suffered from a particularly low yield due to its propensity to oxidize under the conditions

required for a Friedel-Crafts acylation (See Appendix).[75] A sixth ligand, 6-ferrocenylhexanethiol (FcC_6SH), available commercially, was also used in this study.
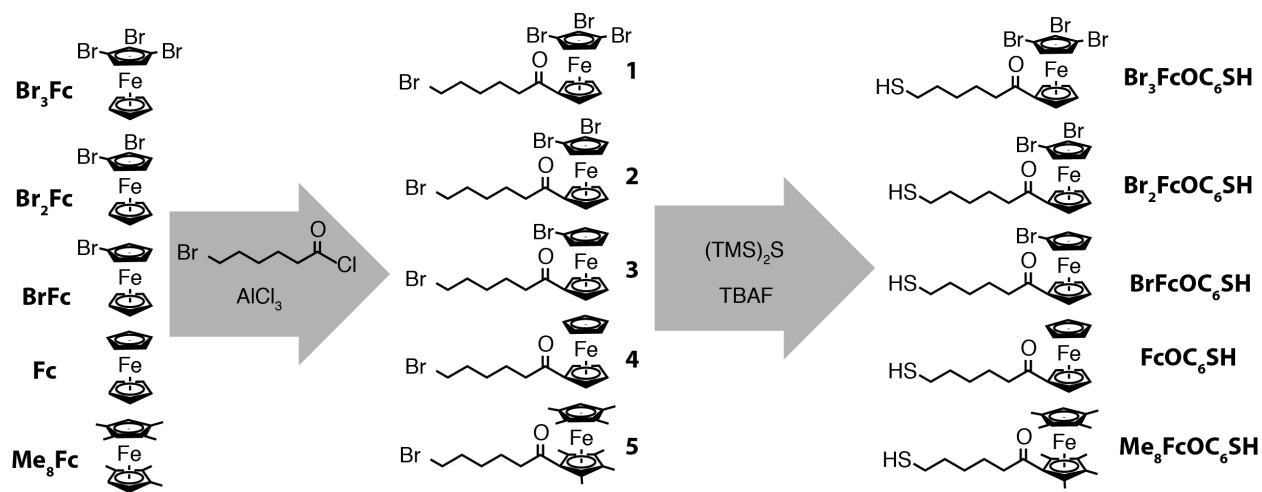
Figure 3.2. Scheme for synthesis of ferrocene derivatives. Synthesis of Br_3FcOC_6SH, Br_2FcOC_6SH, $BrFcOC_6SH$, $FcOC_6SH$, and Me_8FcOC_6SH via a Friedel-Crafts acylation to make compounds **1-5**, followed by a thiolation reaction with bis(trimethylsilyl)sulfide to produce the desired products (see Appendix for further detail).
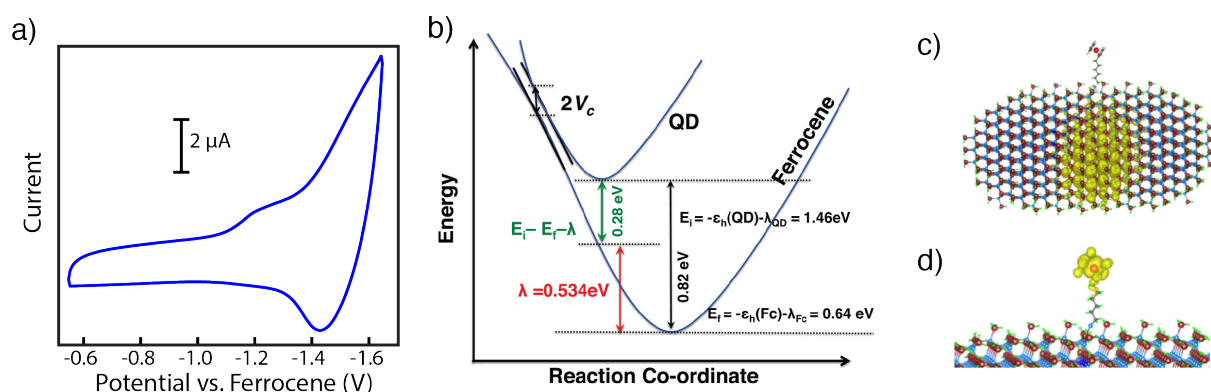
Figure 3.3. Electrochemical and theoretical determination of QD energetics (a) Low temperature CV of a cross-linked QD (sample 1) film. Reductive filling of the conduction band is observed to start at approximately -1.25 V vs. Fc/Fc$^+$. Oxidative removal of some of these charges can also be observed as negative current in the anodic sweep. (b) Marcus theory energy diagram. The QD indicates the total energy curve when the hole is located on the QD, while the ferrocene indicates the total energy curve when the hole is located at the ferrocene. $V_c = |H_{a,b}|$, the electronic coupling. Model of the theoretical system with the (c) QD valence band state, and the (d) ferrocene HOMO state shown with an isosurface representation.

To determine the energetics of the system, and therefore the driving force for hole transfer, the band energies of the CdSe/CdS core/shell quantum dots were first determined by referencing to ferrocene via low temperature cyclic voltammetry measurements of the conduction band edge. Band filling was observed at -1.25 (±0.05) V vs. ferrocene (see Figure 3.3a). This measurement probes the lowest energy electronic state, which for CdSe/CdS core/shell systems has been shown to be delocalized over both the core and the shell.[76-78] Therefore, this state is electrochemically accessible and its measurement gives the LUMO energy of the core/shell system. The QDs used for this measurement had a fluorescence peak at 2.03 eV. Assuming this to be the difference in energy between the conduction band of the

core/shell system and the valence band of CdSe, the valence band energy could be approximated as + 0.78 (±0.05) V vs. ferrocene (Figure 3.4b). This value is in good agreement with theoretical work on CdSe/CdS core/shell rods that determined the position of the valence band edge of the CdSe core at + 0.82 V vs. ferrocene (See Figure 3.3b-d).[49] Slight deviations may be a result of the smaller CdSe cores used in the rod study, which would shift the valence band down by a small amount.

Cyclic voltammetry was used to determine the reversible potentials, and thus HOMO energies of the ferrocene derived ligands. The ligands were referenced to unfunctionalized ferrocene and cover an 800 meV range in potentials (Figure 3.4a). It should be noted that the electrochemistry on the ferrocene derivatives was performed in the reductively stable electrochemical solvent of tetrahydrofuran, while the optical studies to determine charge transfer rates were performed in chloroform-*d* diluted into chloroform, to allow for direct optical measurement of the NMR solutions. This may lead to a slight systematic deviation in the precise value of the driving force, yet the range and the trend will remain the same. This deviation is likely less than ~10% since the difference in measured redox potentials between ferrocene and decamethylferrocene is 483 mV in chloroform and 427 mV in tetrahydrofuran.[79]
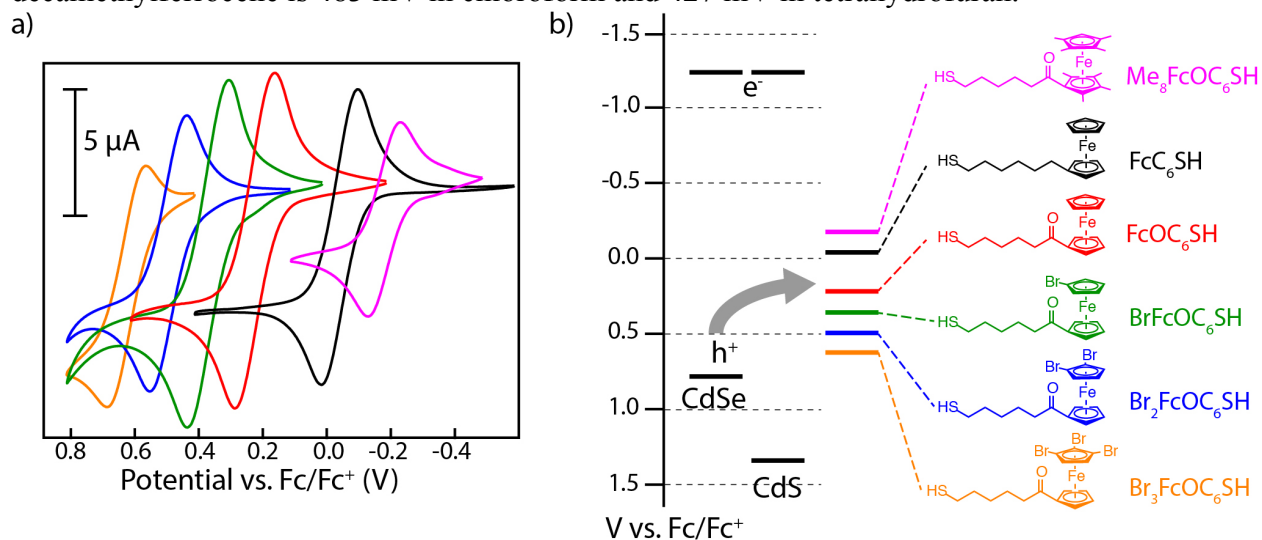
Figure 3.4. Cyclic voltammetry and energy diagram of ferrocene derivatives. (a) Cyclic voltammograms of the ferrocene ligands collected in 0.1 M TBA-PF$_6$ in THF, scanned at 10 mV s^{-1} and referenced to Fc/Fc$^+$. Br$_3$FcOC$_6$SH (orange), Br$_2$FcOC$_6$SH (blue), BrFcOC$_6$SH, (green) FcOC$_6$SH (red), FcC$_6$SH (black), and Me$_8$FcOC$_6$SH (magenta). (b) Energy diagram of CdSe and CdS valence and conduction bands relative to the six ferrocene ligands used in the study.

3.3 Relative rate constants of hole transfer

With a well-characterized and sizable range in driving forces established, QD-molecular conjugates were prepared and the relative charge transfer rate constants were determined by monitoring the photoluminescence quenching as a function of ferrocene coverage. The work in Chapter 2 demonstrated that this quenching is directly attributable to hole transfer to ferrocene, scaling accordingly with coverage and coupling.[50] As in Chapter 2, the work in this chapter relies on quantitative ^{1}H NMR to determine relative ligand concentration.
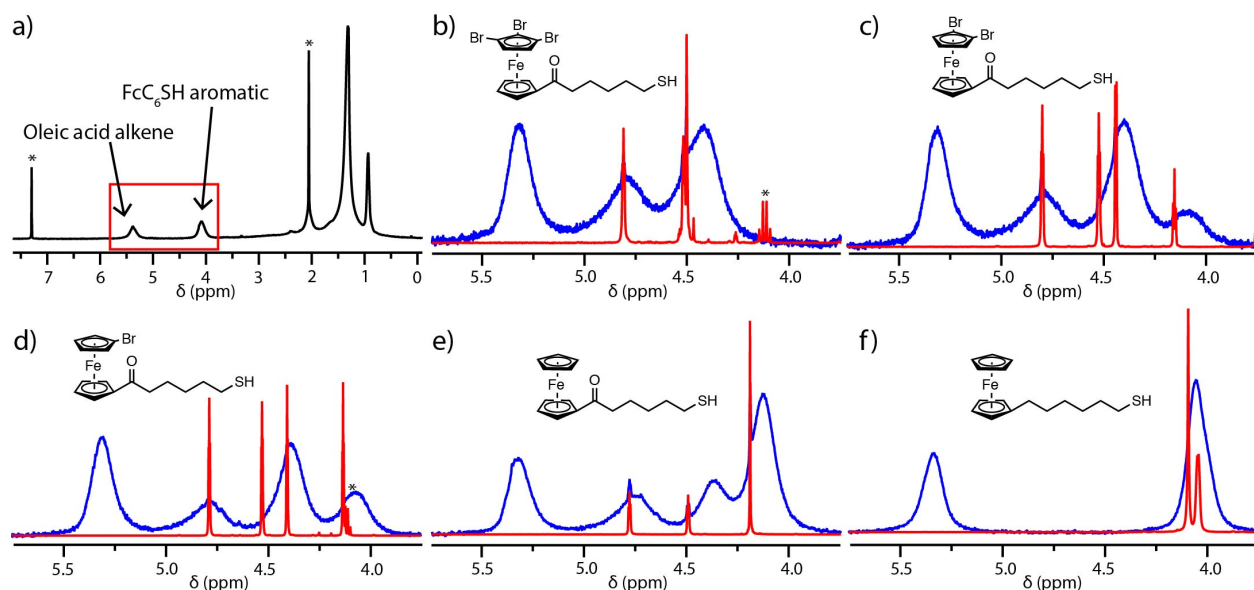
Figure 3.5. ¹H NMR spectra of ferrocene ligands. (a) Full spectrum of a QD sample with partial ligand exchange from the native oleate ligand to FcC₆SH. Solvent peaks are from chloroform and acetonitrile. (b-f) Expanded spectra on the ppm region of interest, which includes ferrocene aromatic protons and oleic acid alkene protons. (Red) spectra of ferrocene ligands free in solution, and (blue) spectra of ligands bound to QD surface, including oleate.

The current work quantifies ligand coverage by integration of the aromatic protons on the ferrocene derivatives (4-5 ppm) and referencing to an external standard. Since, the native ligands are primarily oleic acid with some residual octadecylphosphonic acid (ODPA), only the ferrocene resonances appear within the 4-5 ppm range (See Figure 3.5). This allows for accurate quantification of the concentration of all surface bound acceptor molecules in this study except for Me₈FcOC₆SH. This particular derivative has only one aromatic proton at 3.33 ppm, thus making it difficult to directly quantify. Therefore, loss of oleic acid was used as a proxy for Me₈FcOC₆SH coverage. Ferrocene thiol ligands likely undergo a one to one exchange with oleic acid as evidenced by the fact that the total ligand concentration (oleic acid + ferrocene) remains constant over the course of a ligand, with deviations on the order of 10-15%. Therefore the method for measuring Me₈FcC₆SH coverage is accurate, yet prone to slightly larger uncertainty than direct quantification. This is illustrated in Table 3.1, where the total ligand concentration is defined below in analogy to the *rel. Fc conc.*:

$$total\ lig.conc. = \frac{[OA] + [Fc\ ]}{QD\ Abs_{500\ nm}} \tag{7}$$

QD sample	<(total lig. conc.)>	stdev(total lig. conc.)	max % exchngd	Number of data points
1	0.33	0.03	44%	25
2	0.52	0.05	57%	14
3	0.54	0.05	46%	8
4	0.45	0.07	60%	11
5	0.36	0.03	44%	6

Table 3.1. Analysis of ligand exchange between ferrocene ligand and oleic acid. The average total ligand concentration for each QD sample is shown as well as the standard deviation in this value. The data points correspond to each point in **Figure 3.6**. The maximum percent exchange between the ferrocene ligand and oleic acid is also shown.

To determine the relative rate constants for hole transfer among these ferrocene derivatives, the PLQY was measured with varying surface concentrations of the acceptor ligand. As shown in Chapter 2, a plot of PLQY vs. N will yield a unique hole transfer rate constant per ligand (k_{ht}) (Equation (5)), given a known k_r and k_{nr} of a QD sample. All of the QD-ferrocene conjugates exhibited behavior well modeled by Equation (5 and yielded values for k_{ht} consistent with tunneling through the shell and organic linker, while the thiol binding head was found to have a negligible effect on the quenching.[50]

Equation (5 can be reformulated in terms of the native PLQY (QY_0), a relative ferrocene concentration (*rel. Fc conc.*), and a coefficient, *a*, proportional to k_{ht} (Equation (8). The *rel. Fc conc.* is the ratio of surface-bound ferrocene concentration (in mM) measured via NMR to the optical extinction of QDs at 500 nm in the same solution (Equation (9). Therefore, the relative ferrocene concentration serves as a proxy for the number of acceptor molecules per QD and will be proportional to N for a given batch of QDs. The *a* factor can then be related to a ratio of de-excitation rate constants as well as the molar extinction coefficient for the QDs at 500 nm (ε_{500nm}) (Equation (10).

$$PLQY = \frac{k_r}{k_r + k_{nr} + Nk_{ht}} = \frac{QY_0}{1 + (rel.\,Fc\,conc.)*a} \qquad (8)$$

$$rel.\,Fc\,conc. = \frac{[Fc\,ligand]}{QD\,Abs_{500\,nm}} \qquad (9)$$

$$a = \varepsilon_{500\,nm}\;\frac{k_{ht}}{k_r + k_{nr}} = b*k_{ht} \qquad (10)$$

While there have been extensive studies on determining the extinction coefficient for single composition QDs,[80,81] it is difficult to accurately determine extinction coefficients for core/shell QDs. Since the goal of this work is to determine *relative* rates for charge transfer between ligands, it sufficed to leave ε_{500nm} as an unknown constant, and perform the analysis based on the fact that *a* would be proportional to k_{ht}, related by a constant, *b*, that will be invariant for a given batch of QDs.

PLQY vs. relative ferrocene concentration relationships were constructed by performing successive ligand exchange reactions on portions of QD stock solutions containing approximately 10-25 μmol of surface-bound oleate ligand in 0.6 mL of solution. Lower

concentrations resulted in NMR spectra that were too noisy to easily interpret, while higher concentrations consumed too many QDs. Owing to difficulty in scaling up the core synthesis and the subsequent shelling reaction, the quantity of QDs in a given batch limited our ability to perform all ligand exchanges on a single sample of QDs. Therefore, ligand exchanges were performed on five separate batches of QDs with similar valence band positions, ensuring consistent driving forces. Since the CdSe core dictates the valence band position, similar sized cores were used in all core/shell syntheses. The cores used had first absorption peaks of 563, 565, 560, 560, and 559 nm, which would result in deviations in the valence band of no more than 10 meV. PLQY vs. *rel. Fc conc.* plots are shown in Figure 3.6 for five QD samples, each underwent 2-5 series' of ligand exchanges. For example, five portions of QD sample 1 underwent ligand exchange with five of the ferrocene derivatives used in this study.
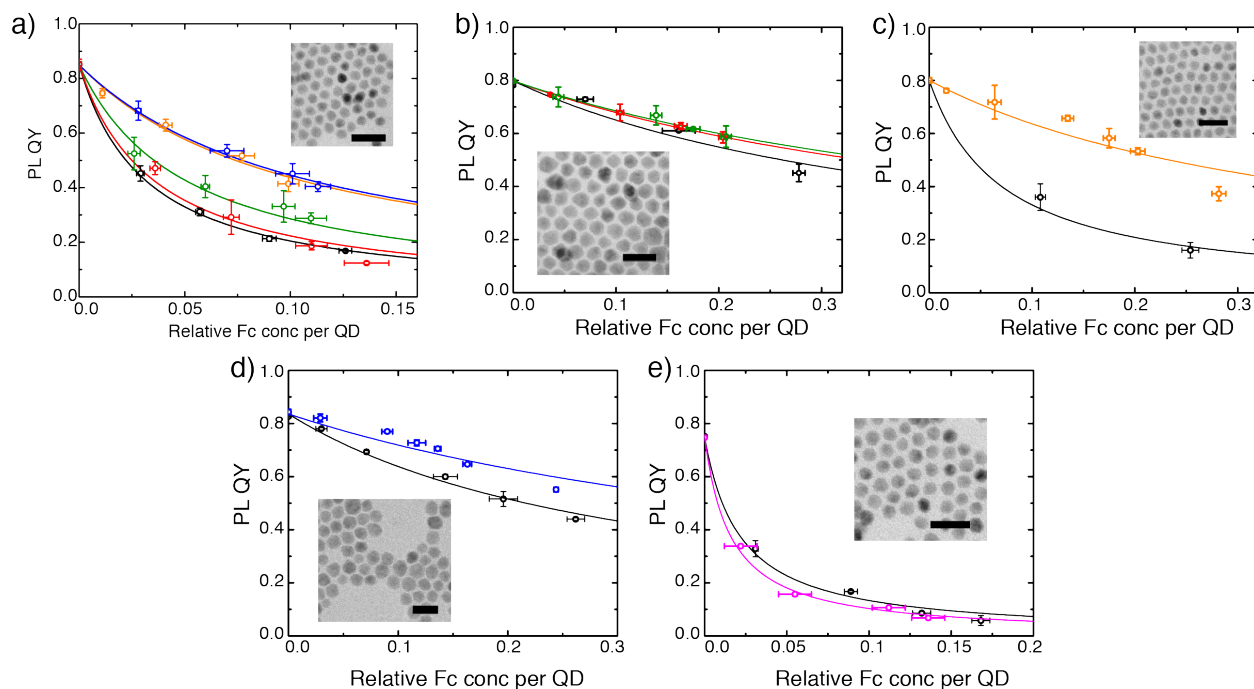
Figure 3.6. PLQY of QDs vs. relative Fc concentration. Fits to Equation **(8** are shown as solid lines for QD samples (a) 1, (b) 2, (c) 3, (d) 4, (e) 5. Br_3FcOC_6SH (orange), Br_2FcOC_6SH (blue), $BrFcOC_6SH$, (green) $FcOC_6SH$ (red), and FcC_6SH (black), Me_8FcOC_6SH (magenta). Insets: TEM micrographs of QD samples used with 25 nm scale bar.

The five QD samples did vary significantly in CdS shell thickness, with total diameters ranging from 7.3 nm to 11.9 nm (full details in Appendix). Although the values of k_{ht} will certainly vary with shell thickness for a given ligand as the electronic coupling between donor and acceptor will change dramatically, the work in Chapter 2 has shown that the ratio of hole transfer rate constants for two distinct ligands is consistent across multiple shell thicknesses.[50] Therefore, a relative hole transfer rate constant (relative k_{ht}) is reported for each ligand by referencing to the quenching rate of FcC_6SH, which was exchanged onto QD samples 1-5. This relative hole transfer rate constant is the ratio of the *a* value for a given ligand on QD sample *x* to the *a* value for FcC_6SH on QD sample *x*.

3.4 Driving force vs. rate constant relationship

Scaling the relative hole transfer rate constants on each QD to the value measured for FcC_6SH allows for all collected data to be represented on one plot of relative k_{ht} vs. driving force (Figure 3.7a). Uncertainties were generated from bootstrap error analysis while fitting the PLQY vs. *rel. Fc conc.* data, incorporating the experimental error present in both the PLQY and *rel. Fc conc.* data. The errors in values of the relative k_{ht} are therefore a convolution of fitting error and experimental error. Error bars for QD samples 2-5 were constructed from both the uncertainty in relative k_{ht} for the ligand in question as well as the reference ligand, FcC_6SH. Since five ligands were exchanged onto QD sample 1, uncertainties are shown for each of the ligand's relative k_{ht} values independently, including FcC_6SH. Each ligand, except for Me_8FcOC_6SH, was exchanged onto more than one QD sample. Therefore, the plot for driving force vs. rate gives a sense of the range in relative rate constants that can be measured.
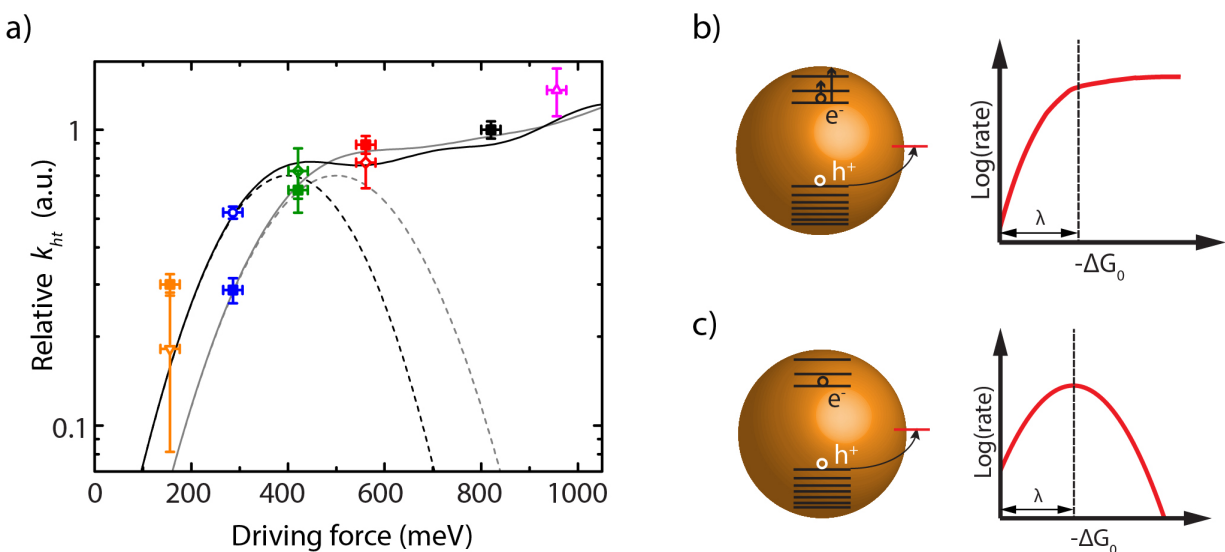
Figure 3.7. Driving force vs. rate constant. (a) Plot of the relative hole transfer rate constant as a function of driving force. Data for ferrocene ligands collected on different QD samples are scaled to the rate constant for FcC_6SH (set to one). Filled square data points are from QD sample 1, all unfilled data points are from QD samples 2-5. The dashed lines shows behavior expected from a two-state Marcus model (Equation (**2**). The solid lines show behavior expected from the Auger-assisted model (Equation (**11**). Reorganization energies of (black) 400 and (gray) 500 meV were used. (b) Schematic of general behavior predicted by the Auger-assisted model for charge transfer. The electronic excitation in the conduction band occurs during hole transfer, thus reducing the effective driving force and eliminating the inverted region. (c) Schematic of behavior predicted by the two-state Marcus model. Without the coupled electronic excitation, one would expect an inverted region.

The plot of relative rate constant vs. driving force was first examined in reference to the two-state non-adiabatic Marcus model (Equation (2). As was discussed in Chapter 1, the rate constant (k_{ct}) is expected to first increase with increasing driving force ($-\Delta G_0$), but to then decrease for driving forces greater than the reorganization energy (λ). These Marcus parameters were simulated computationally on the system mentioned earlier with FcC_6SH tethered to a CdSe/CdS nanorod (Figure 3.3b-d).[49] In this work, density functional theory was used to determine molecular reorganization energies, while solvent reorganization was computed with a dielectric continuum model. The resultant net reorganization energy for hole transfer to FcC_6SH in chloroform was calculated to be approximately 500 meV. However, in the experimental system, the ferrocene ligand will also be surrounded by lower dielectric alkane ligands along

with chloroform, thus reducing the reorganization energy.[49] Therefore, λ was set to values of 400 and 500 meV to generate expected rate vs. driving force plots (Figure 3.7a), against which to compare the experimental data. It is clear that the standard two-state Marcus model does not fit the current data since there is no inverted region. It is unlikely that this discrepancy is due to an inaccurate reorganization energy, since λ would have to be greater than 1 eV to fit the data. In water, the reorganization energy of analogous ferrocene ligands is at most 0.85 eV.[41] In the lower dielectric solvent of chloroform, this value would be decreased, and the QD would be expected to have only a minor contribution to λ.

Since there is no observable inverted region in the results, we turn to the Auger-assisted model for charge transfer described in section 3.1 to better model the data.[44,82] In this model charge transfer can be coupled with intraband excitation of the residual charge in the QD. This allows the rate to stay high at large driving force, since the excess energy that would go to vibrations in the standard Marcus model is instead efficiently coupled into electronic excitation (Figure 3.7b). The resultant rate can then be written as a sum of rates associated with each accessible electronic excitation (Equation (11). For hole transfer, the values of $E_{e,i}$ correspond to conduction band energy levels relative to the band edge where $E_{e,0} = 0$.

$$k_{ct} = \sum_{i=0} \frac{2\pi}{\hbar} |H_{a,b}(E_{e,i})|^2 \frac{1}{\sqrt{4\pi\lambda k_b T}} exp\left(-\frac{(\lambda + \Delta G_0 + E_{e,i})^2}{4\lambda k_b T}\right) \qquad (11)$$

To approximate the conduction band energy levels, we used previously computed values for CdSe core QDs with band gaps equal to the band gaps of the core/shell QDs used in our study (~2 eV).[83] This corresponds to CdSe core QDs with radii of 2.8 nm and $1P_e$, $1D_e$ and $2S_e$ energy levels of 315, 600, and 760 meV above the band edge (Table 3.2). These values were used for $E_{e,i}$ in the functions plotted in Figure 3.7a. It is also assumed that the electronic coupling does not depend on the level of electron excitation, in accordance with previous work.[44,82] It should be noted that many different conduction band energy spacings will reproduce the data we observe as long as the spacings are less than or on the order of the width of the Marcus curve, $\sqrt{2\lambda k_b T}$, which is 160 meV with $\lambda = 500$ meV at room temperature. The estimated conduction band energy levels may underestimate the true density of states in the larger core/shell structures, but this would not change the shape of the curve significantly. For example, a linearly increasing density of states was used by Lian and Prezhdo, and this resulted in curves exhibiting similar behavior.[44]

To further illustrate the variety of spacings that can reproduce the data, additional functional models based on Equation (11 were constructed by changing the conduction band energy spacings ($E_{e,i}$) and the reorganization energy (λ). Conduction band spacings that were previously calculated and correspond to different size CdSe core QDs were used (Table 3.2).[83] Additionally, reorganization energies of 400 and 500 meV were used in accordance with Figure 3.7. It is clear from the data below (Figure 3.8) that oscillations in the driving force vs. rate behavior only become prevalent with large spacings in the conduction band.

Conduction band energies (meV)	5.6 nm diameter CdSe	7 nm diameter CdSe	4.8 nm diameter CdSe	4 nm diameter CdSe
$E_{e,1}$	315	225	380	500
$E_{e,2}$	600	440	750	940
$E_{e,3}$	760	560	915	--
$E_{e,4}$	--	660*	--	--
$E_{e,5}$	--	760*	--	--
Color	Black	Blue	Green	Red

Table 3.2. Conduction band energies used in Auger-assisted model. Energies used in the functional models from Equation **(11** and the corresponding diameters of the core CdSe QDs on which they are based. The values for $E_{e,i}$ were available up to $i = 3$, so we assumed a 100 meV spacing for the higher energies in the 7 nm CdSe QD (see values with *).
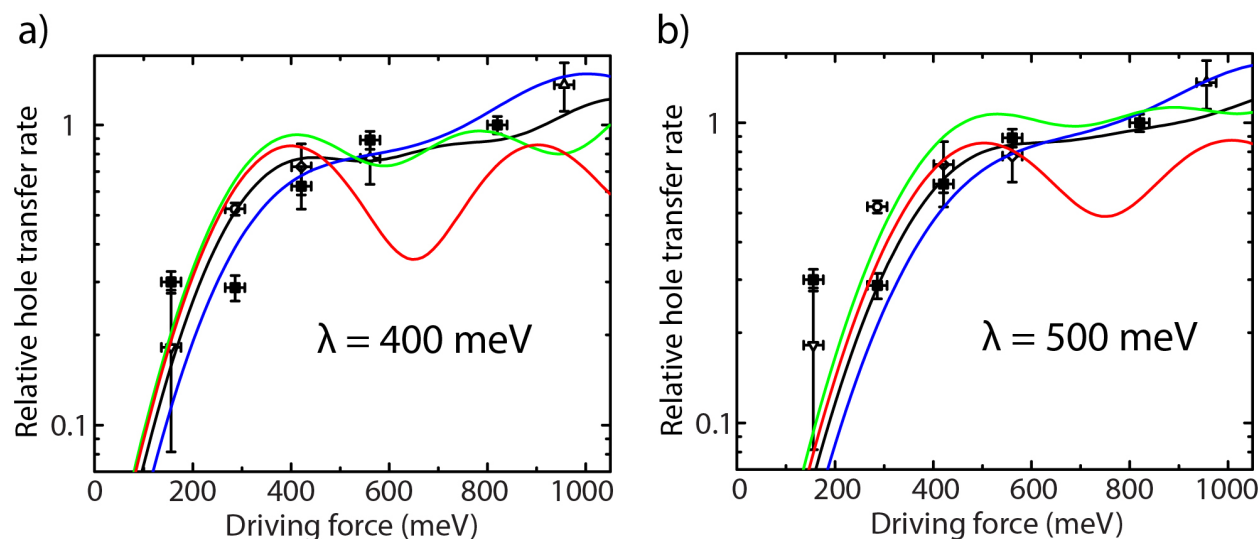
Figure 3.8. Driving force vs. rate plots with data fit to eight different functional forms. Reorganization energies of (a) 400 meV and (b) 500 meV were used. Conduction band spacings correspond to CdSe cores of diameter 5.6 (black), 7.0 (blue), 4.8 (green), and 4.0 (red) (listed in **Table 3.2**).

3.5 Size dependence and an improved model

Three different core/shell QD sizes were used to study the size dependence of the driving force vs. rate relationship. These samples have significantly thinner shells than what were used in the first part of this chapter. Thin shells were used to ensure measurable PLQY quenching of these QDs with a small number (~10) of hole quenchers tethered to the surface. Ultimately, this strategy allowed us to circumvent both cleaning of excess ligand and NMR since at these low concentrations, nearly all thiolated ferrocene ligands added to the QD solution end up binding to the QD surface.

The three QD samples had diameters (errors) of 3.6 (0.3), 4.1 (0.4), and 6.3 (0.6) nm; see Appendix for synthetic details. The 3.6 and 4.1 nm core/shell QDs were both synthesized from 2.2 nm diameter CdSe cores while the 6.3 nm core/shell QDs were synthesized from 4.3 nm diameter CdSe QDs. The three QD samples have band gaps of 2.34, 2.28, and 2.00 eV (smallest size to largest size) as determined by the emission peak, and PLQYs of 19%, 50%, and 45% respectively (Figure 3.9a). The moderate PLQYs indicate that significant non-radiative processes

will still be present at room temperature in these QDs, a consequence of the thin shell approach. The valence band edge position of the core/shell QDs were derived from the value measured electrochemically (Figure 3.3), adjusted for changes in the band gap of the CdSe core such that one third of the change in band gap could be attributed to the hole level (due to the ratio of electron and hole effective masses). This approximation assumes that the hole is localized to the CdSe core, and the size of the core dictates the valence band energy.
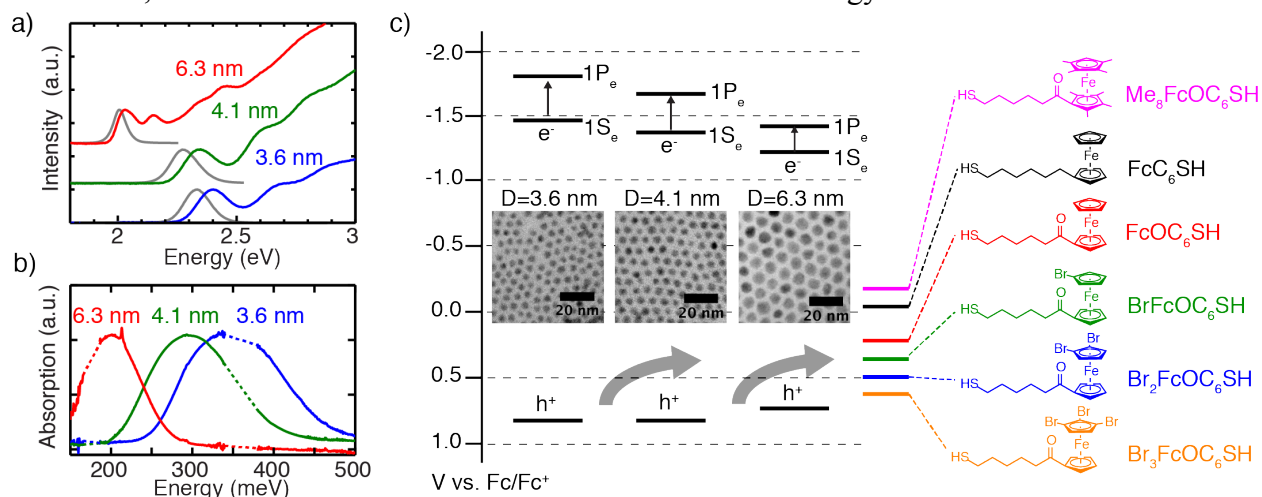
Figure 3.9. Energetics of the system with three QD sizes. (a) Absorption and emission (gray) spectra of the 3.6, 4.1, and 6.3 nm QDs. (b) IR intraband absorption spectra of the three QDs after electronic photodoping with lithium triethylborohydride. Dashed sections were removed due to large solvent absorption. (c) Energy diagram with QD band gaps determined from optical emission and $1S_e$-$1P_e$ transition energies determined from IR measurements. Ferrocene ligand energies were determined in previous work. TEM micrograph insets for each sample are shown with 20 nm scale bars.

The intraband energy spacings in the conduction band were also measured since they are important in implementing the Auger-assisted model for hole transfer from CdSe/CdS core/shell QDs. Recent work by the Gamelin group has demonstrated a facile method for photochemically doping CdSe QDs with excess electrons in the conduction band by using lithium triethylborohydride as a hole scavenger.[84] Steady-state IR absorption spectroscopy of these electronically doped QDs allows for a direct measure of the $1S_e$-$1P_e$ transitions, and therefore provides the energy of the first electronic excited state (Figure 3.9b). As expected, the $1S_e$-$1P_e$ transition energy decreased with larger QD diameters with energies of 345, 293, and 201 meV for the three different size QDs studied. It should also be noted that since the CdSe/CdS conduction band offset is small, the core/shell QDs have reduced energies with respect to their respective CdSe cores due to electron delocalization into the shell.

Hole transfer rate constants were measured from each of the three QD samples to the six ferrocene derivatives shown in Figure 3.9c using steady state PL quenching at RT. In order to reliably prepare solutions of known concentration for both the QDs and ferrocene ligands, extinction coefficients for each species were determined. Inductively coupled plasma atomic emission spectroscopy (ICP-AES) of the Cd concentration of nitric acid-digested QDs coupled with TEM sizing data was used to determine the molar extinction for the three QD samples. Quantitative ^{1}H NMR was used to determine molar extinction coefficients of the ferrocene ligands, which had absorption peaks near 440 nm and molar extinction coefficients ranging from 109 to 504 M^{-1} cm^{-1}.

For these studies, we found that mixing known concentrations of QDs and a chosen ferrocene ligand at room temperature resulted in rapid and high yield exchange of the ferrocene ligand on to the surface of the QD as long as the average number of ferrocene ligands per QD was below ~20. ^{1}H NMR was used to characterize the extent of exchange, although on much higher concentration samples than were used for optical studies. Over the range of ligand to QD ratios used for optical studies, both the 3.6 and 4.1 nm QDs exhibited quantitative exchange for thiolated ferrocene ligands added. A small percentage (7-20%) of each ligand addition contained the ferrocene disulfide dimer, which was observed to not participate in exchange.

The exchange percentages of thiolated ferrocene ligands on the 6.3 nm QDs varied over the range studied (100 - 70%) and could be fit to an equilibrium model to predict the percentage bound as a function of amount added. In this equilibrium model, the thiolated ferrocene ligand can exchange with bound oleic acid and vice versa. Therefore, the equilibrium constant is given by:

$$K = \frac{(Fc\ bound\ per\ QD)^2}{(free\ Fc\ ligands\ per\ QD)(OA_0 - Fc\ bound\ per\ QD)} \quad (12)$$

Where OA_0 is the amount of oleic acid per native QD (in the case of the 6.3 nm QDs, this was 78 ligands per QD). The number of ligands added per QD was quantified with optical extinction of the addition solution, and the concentration of free ligands present was determined by integration of NMR peaks (not counting the disulfide). The bound ligand concentration is just the difference between these two values. Fitting results for both FcC_6SH and $FcOC_6SH$ gave K = 1.15. The correspondence between the two ligands also validates employing the same K for all ligands used, see Figure 3.10a.
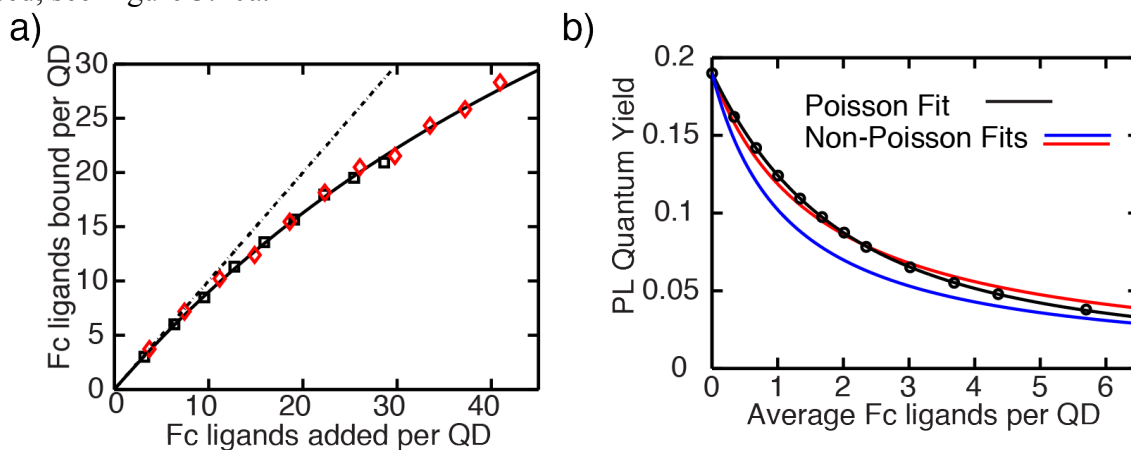
Figure 3.10. Effect of binding equilibria and Poissonian statistics on quenching curves. (a) Ligands bound per QD as a function of amount added for FcC_6SH (black squares) and $FcOC_6SH$ (red diamonds) onto the 6.3 nm QDs. The expected behavior according to Equation **(12** is plotted (solid line). The dashed line represents a quantitative binding model. (b) PLQY quenching curve for Me_8FcOC_6SH on the 3.6 nm QDs. The best fit to the data using Equation **(13** (red) is not as accurate as the best fit to the data using Equation **(14** (black), with the Poisson distribution. The blue line represents the quenching behavior without the Poisson distribution, but with the same hole transfer rate as the black curve.

Steady state quenching was performed on ~0.3 µM QD solutions that were sequentially exposed to aliquots of a solution of a given ferrocene ligand at RT. Steady state PL spectra were acquired after each ligand addition thus allowing for determination of the per-molecule hole transfer rate constant, k_{ht}. For a uniform sample of QDs, each with the same number of ligands

attached, the PLQY vs. number bound per QD (N) was shown in Chapter 2 to fit the following relation (from Equation (5):

$$PLQY = \frac{k_r}{k_r + k_{nr} + Nk_{ht}} = \frac{PLQY_0}{1 + N\tau_0 k_{ht}} \tag{13}$$

where $\tau_0 = (k_r + k_{nr})^{-1}$ is the luminescence lifetime for the native QDs. The PLQY of the native QDs is then given by $PLQY_0 = \tau_0 k_r$. Since the work in this section with thin shells is in the limit of few quenchers per QD, we found that employing a Poisson distribution of quenchers produced more adequate fits using the following relation:

$$PLQY(\langle N \rangle) = \sum_{N=0}^{\infty} \frac{\langle N \rangle^N e^{-\langle N \rangle}}{N!} \frac{PLQY_0}{1 + N\tau_0 k_{ht}} \tag{14}$$

where $<N>$ is the average number of ferrocene ligands bound per QD (See Figure 3.10b). The PL quenching curves for the two smallest QDs (3.6 and 4.1 nm) fit well to this model. RT quenching data from the 6.3 nm QDs was fit to Equation (14 with the $<N>$ value adjusted in accordance with the equilibrium model derived from the ^{1}H NMR measurements. RT quenching data are shown in Figure 3.11.
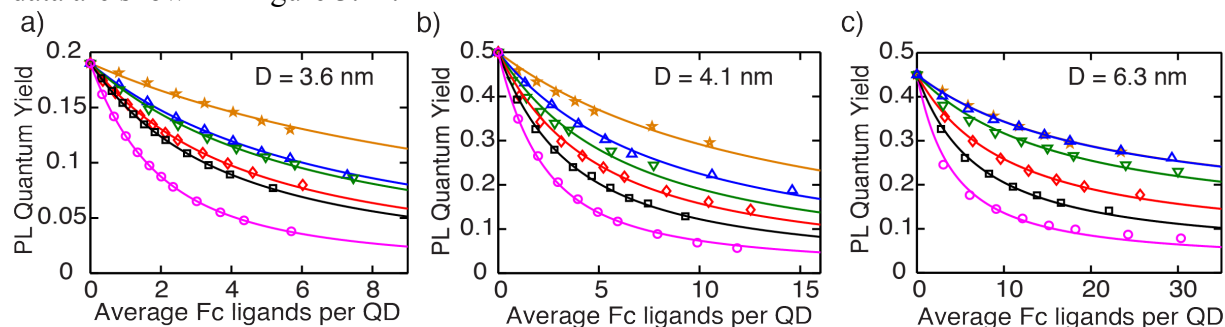
Figure 3.11. PL quenching of QD-ferrocene conjugates. (a-c) PLQY quenching of QDs as a function of the number of ferrocene ligands added. Data points represent experimental measurements and solid lines are fits using Equation (14. Br_3FcOC_6SH (orange, pentagrams), Br_2FcOC_6SH (blue, triangles), $BrFcOC_6SH$ (green, downward pointing triangles), $FcOC_6SH$ (red, diamonds), FcC_6SH (black, squares), $Me_8FcOC6SH$ (magenta, circles).

Fits to the RT quenching data for the 3.6, 4.1 and 6.3 nm QDs to Equation (14 produced values for the hole transfer rate constant per molecular acceptor, k_{ht}. In Figure 3.12a, these values are plotted as a function of the thermodynamic driving force for hole transfer for each of the three QD sizes, clearly exhibiting a monotonic increase in rate with driving force, consistent with what was seen in the first part of this chapter Figure 3.12a also shows curves constructed using the Auger-assisted formulation of the Marcus model and the $1S_e$-$1P_e$ energies measured via IR absorption, instead of theoretical energy spacings as were used in the previous section. Higher energy intraband excitations, such as $1S_e$-$1D_e$, were incorporated by using a model for CdSe core QDs developed by Efros and Bawendi.[83,85] This model generated a series of conduction band energy levels, $E_{e,i}$, and associated degeneracies, $g_{e,i}$, given by the spherical harmonics. A full list of these energies and degeneracies is shown in Table 3.3. The Auger-assisted model from the last section (Equation (11), therefore had to be modified to account for these degeneracies:

$$k_{ht} = \sum_{i=0} \frac{2\pi}{\hbar} g_{e,i} |H_{a,b}|^2 \frac{1}{\sqrt{4\pi\lambda k_b T}} exp\left(-\frac{(\lambda + \Delta G_0 + E_{e,i})^2}{4\lambda k_b T}\right) \qquad (15)$$

For this dataset, the reorganization energy is set to $\lambda = 400$ meV, in accordance with previously accepted values for this parameter in these systems.[44,49,63] The only tunable parameter in fitting these curves was therefore the electronic coupling, which is expected to be exponentially dependent on the donor-acceptor separation in accordance with a tunneling relationship: $|H_{a,b}|^2 \propto exp\,(-\beta d)$ (described first in Equation (3). In Chapter 2, the hole transfer through a CdS shell yielded a damping coefficient of $\beta = 0.24$ Å^{-1}.[50] Plotting the square of the electronic coupling vs. shell thickness (Figure 3.12b) for the three QD sizes is generally consistent with this previously determined damping coefficient (solid lines) for a given core size. It is worth noting that the larger core size has a smaller electronic coupling, consistent with its predicted smaller surface wave function population relative to smaller QDs.
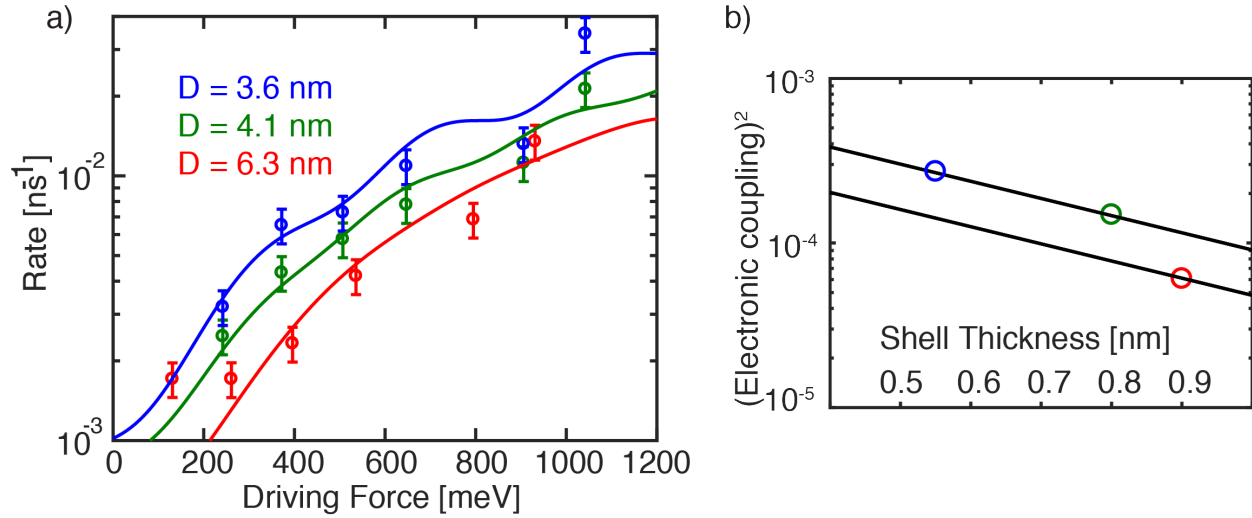
Figure 3.12. Rate vs. driving force and electronic coupling for three QD sizes. (a) Extracted per molecule hole transfer rates as a function of driving force for each QD size: 3.6 nm (blue), 4.1 nm (green), and 6.3 nm (red). Solid lines represent fits to the data using Equation **(15**. (b) Electronic coupling squared as a function of shell thickness. Solid lines represent tunneling rates with $\beta = 0.24$ Å^{-1} (Equation **(3**).

Transition	i	$E_{e,i}$ (3.6 nm) (meV)	$E_{e,i}$ (4.1 nm) (meV)	$E_{e,i}$ (6.3 nm) (meV)	$g_{e,I}$ (degeneracy)
$1S_e$-$1S_e$	0	0	0	0	1
$1S_e$-$1P_e$	1	**345**	**293**	**201**	3
$1S_e$-$1D_e$	2	705	603	422	5
$1S_e$-$2S_e$	3	859	737	519	1
$1S_e$-$1F_e$	4	1071	922	653	7
$1S_e$-$2P_e$	5	1296	1119	798	3

Table 3.3. Values of $E_{e,i}$ based on the IR absorption measurements. The first few transition energies are listed for CdSe radii with $1S_e$-$1P_e$ transition energies equal to those measured for the three core/shell QDs used in the study (measured via IR absorption, bold values).

3.6   Implications of the Auger-assisted model

Despite the success of the Auger-assisted model in reproducing the experimental data, there is currently no direct spectroscopic evidence for the intraband transition associated with the Auger-assisted mechanism, and other mechanisms could be proposed. For example, Auger-assisted electronic transitions within the distribution of surface states could also be coupled to charge transfer, which would also eliminate the inverted region. Further transient spectroscopic studies that can directly probe the absorption of the coupled transition would be necessary to definitively determine which state is coupled to charge transfer.

Nevertheless, the experimental trend informs avenues for designing more efficient QD-based photoconversion devices. The results suggest that the initial hole transfer process should be driven by approximately 300-500 meV ($\sim\lambda$), but any additional driving force will result in minimal gains in rate. The results from this model system can also help to understand how charge trapping competes with QD luminescence, relevant for applications in QD emission. Specifically, because charge transfer rates to traps will not decrease at high driving force, QD trap states deep within the band gap would continue to be efficient quenchers of emission. Lastly, in the context of the Auger-assisted model, one would expect the Marcus inverted region to be present for hole transfer in charge separation systems in which the electron transfer occurs on faster timescales than hole transfer. In this case, hole transfer would occur with no electron in the conduction band, thus eliminating the possibility for Auger-assisted electron excitation. However, further work is needed to better resolve the underlying mechanism in order to confirm this predicted behavior.

Chapter 4 : Temperature dependent charge transfer

4.1   Role of reversible traps in QD systems

Recent theoretical and experimental work suggests that surface hole traps of CdSe QDs, although ill-defined and possibly broadly distributed, are energetically located near the valence band edge.[49,86-88] Therefore, de-trapping back to the band edge is energetically possible at room temperature. A series of studies from the groups of Scholes[89,90] and Kambhampati[91-93] have found that the temperature dependent QD PL is well modeled by a thermal equilibrium between excitonic states and trap states of similar energy. It should be noted that the studies mentioned above do not deal exclusively with hole trapping, but are instead assigned to unspecified charge transfer to the surface, although hole trapping is expected to dominate.

The first set of studies focus on the temperature dependence of the time-resolved PL lifetime in CdSe/ZnS QDs. Notably, the observed average lifetimes have a non-monotonic dependence on temperature, which can be fit by an activated trapping and de-trapping model. In this model, two assumptions are made: 1) one or more trap state energy distributions exist for an ensemble of QDs and 2) excited charges transfer to these trap states in accordance with classical Marcus theory.[90] Global fits of the data following this model reveal two trap state densities with average energies either near the band edge (within 10 meV) or 100-150 meV energetically uphill. Additionally, the computed reorganization energies for the surface traps range from 200-400 meV and predictably track with the dielecric of the solvent.[90]

The studies from Kambhampati analyze the temperature dependence of both band edge and trap emission. The behavior is well modeled by a similar trapping and de-trapping model as that proposed by Jones *et al* in the previous paragraph. The authors find that a semi-classical formulation of Marcus theory (Marcus-Jortner theory) recovers the observed behavior across a broad range of temperatures. In this model, a single trap of energy within ~70 meV of the band edge was found to be sufficient in fitting the data.[91-93] Additionally, the best fitting parameters included a total reorganization energy of ~600 meV, which is somewhat consistent with other work mentioned.[49,89] Importantly, the model produced by the Kambhampati group also showed that emission from these shallow traps is significantly red-shifted and broadened relative to the band edge emission as a result of strong coupling to optical phonons. Previously, the red-shifted and broadened trap emission was attributed to deep traps well within the QD bandgap.

The existence of trapping and de-trapping implies that long-lived traps could restore fluorescence upon de-trapping back to the excitonic state. This would result in time components of the fluorescence decay longer than the radiative lifetimes. In fact, these long decay components are observed in most standard CdSe QD samples, and they are only eliminated for samples with high PLQY that lack significant surface trapping. Additionally, this delayed fluorescence has recently been linked to the mechanism responsible for fluorescence intermittency (or blinking) seen in single QDs.[94]

4.2   Theoretical work on trap-mediated charge transfer

Mediated charge transfer can occur via two types of traps: deep traps and shallow traps. A deep trap state will lie within the band gap of the QD and will cause irreversible charge trapping. This can only lead to non-radiative recombination and would therefore be reflected in

the PL of the native QDs. The experimental work in Chapters 2 and 3, with high PLQY QDs, excludes this possibility. However, it is possible for hole transfer to the ferrocene molecules to occur via shallow, reversible, traps. In this case, an equilibrium population of shallow surface trap states could still give rise to a substantial PLQY in the native QDs as long as the trap state energies are close to the CdSe valence band. However, the situation would change in the presence of a ferrocene hole acceptor, especially if the hole rapidly transfers from the shallow trap to the Fc HOMO, thus quenching the PL (as was observed in Chapters 2 and 3).

These reversible traps can therefore be harnessed to mediate desirable charge transfer if properly understood. The theoretical work shown in Figure 3.3 that computed the driving force for hole transfer from a CdSe/CdS rod to FcC_6SH also examined this possibility of trap-mediated hole transfer. An example of such a trap state is shown in Figure 4.1. This state is associated with the thiolate binding head of the ferrocene ligand and its energy is about $E_B - E_A \approx 270$ meV below the QD valence band (uphill energetically for a hole). Although this trap is significantly farther in energy from the band edge than an ideal reversible trap candidate, the presence of this state in the theoretical system allows us to directly calculate a rate of trap-mediated charge transfer.
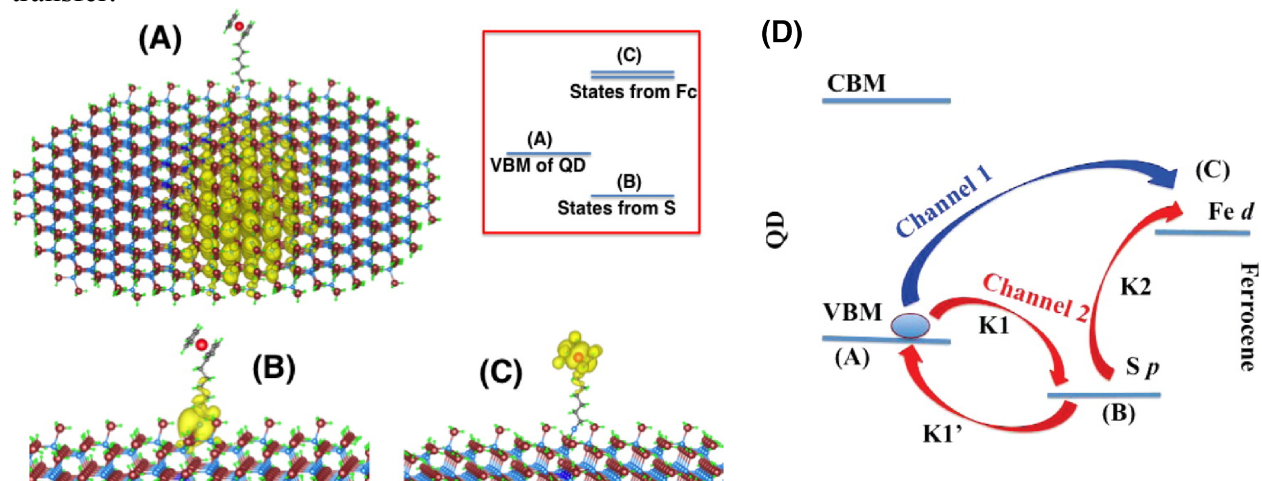
Figure 4.1. Theoretical model used to explore trap-mediated transfer. Wave function isosurface plots for the (A) QD valence band state, (B) state at the sulfur-anchoring site, and (C) the ferrocene HOMO state. Their relative energies are shown as an inset. (D) Schematic of trap-mediated transfer mechanism (Channel 2, red) compared to direct transfer (Channel 1, blue). The electronic states labeled (A), (B), and (C) correspond to the wave functions shown on the left side of the figure. K2 and K1' are both processes downhill in energy while K1 is uphill since the charge carrier is a hole.

The coupling constants between the (A) and (B) states and between the (B) and (C) states shown in Figure 4.1 were found to be 3 meV and 9 meV respectively. Both are much larger than the 0.04 meV coupling between (A) and (C), since (A) and (C) are more spatially separated (see Equation (3)). This suggests that trap-mediated hole transfer could dominate the direct hole transfer pathway. The calculated charge transfer rate from (A) to (B) is $K1 = 6.2 \times 10^{-3}$ ps^{-1} and from (B) to (C) is $K2 = 2.3 \times 10^{-2}$ ps^{-1}. While both transfer rates are significantly faster than the single step transfer rate of 8.6×10^{-6} ps^{-1} (~5×10^{-5} ps^{-1} with the Auger-assisted model), the back transfer rate K1' from (B) to (A) is even faster since it is downhill in energy. Due to the detailed balance formula, we have $K1' = K1 \cdot \exp(-(E_A - E_B)/k_BT) = 2.7 \times 10^{2}$ ps^{-1}. Since this rate is much faster than the (B) to (C) rate, we can assume an equilibrium between states (A) and (B), with the relative population of (B) vs (A) as $\exp((E_A - E_B)/k_BT) = 2.3 \times 10^{-5}$. As a result, the overall

transition rate will be K2*exp(($E_A - E_B$)/k_BT) = 5.2 x 10^{-7} ps^{-1}. This is much smaller than the direct (A) to (C) hole transfer rate.

However, this small rate is a direct consequence of the large energy difference $E_B - E_A$ (~11k_BT), which maintains a very small hole population at the surface trap state. If shallow trap states existed with similar coupling constants to the one studied above but at energies closer to the QD HOMO, then the equilibrium trap population could be orders of magnitude greater resulting in a faster trap-mediated rate compared to the single step transfer. For example, if the $E_A - E_B$ energy difference is less than 8k_BT, then the (B) mediated channel will become faster than the (A) to (C) direct transfer using the two state model. To outcompete the Auger-assisted model, the $E_A - E_B$ energy difference must be less than 6k_BT. This is all assuming that every ligand will have one such intermediate state (e.g., as a result of ideal passivation). If we assume there is only one intermediate trap state for a given QD (e.g. a surface defect state), then this total energy difference must be less than ~2k_BT in order for the channel to be competitive with the direct (A) to (C) hole transfer. This leaves a rather small energy window ($E_B - E_A$ < 50 meV) (since the E_B cannot be smaller than E_A, as precluded by Figure 4.1) for the existence of such defect states in order to interpret the experimentally observed transition rate as the result of an intermediate defect state mediated transition. Whether the charge transfer is trap-mediated or direct therefore depends on the density of surface trap states with energies near the QD valence band, e.g., whether on average there is one defect surface state within a 50 meV energy window or many traps within a 200 meV window.[49]

4.3   Temperature dependent hole transfer

To explore the possibility of trap-mediated charge transfer, temperature dependent hole transfer rates were acquired. Two distinct strategies were employed to determine the rates as a function of temperature. First, time-resolved photoluminescence lifetime (TRPL) measurements were performed in an optical cryostat to yield hole transfer rates. Second, temperature dependent PLQYs were taken in an integrating sphere to confirm these hole transfer rates. The 4.1 and 6.3 nm QDs described in Chapter 3 (Section 3.5) were used with the same six ferrocene ligands to determine hole transfer rate constants (k_{ht}) for temperatures between 78 and 300 K using TRPL measurements along with the following relation:

$$Nk_{ht}(T) = \tau_{Fc}(T)^{-1} - \tau_0(T)^{-1}$$ (16)

Here τ_{Fc} is the temperature dependent lifetime of the ferrocene-functionalized QDs and τ_0 is the lifetime of the native QDs. *N* ranged from 10-30 molecules per QD for these experiments. See Figure 4.2 for representative temperature dependent lifetime traces of the QD-ferrocene conjugates. The extracted hole transfer rates are shown in Figure 4.3. It should be noted that the decay constants at low temperatures (78 K or 100 K) did not depend on the range over which the fit was performed and, aside from a short rise time, the results exhibited highly mono-exponential decays. At higher temperatures, however, the decays deviate from single exponentials, so the decay constants become dependent on fitting range. Therefore, fits were consistently performed over the first decade and the associated error was accepted. This may result in systematic errors in the value of the rate constants measured at higher temperatures, but relative comparisons between ligands are still valid.
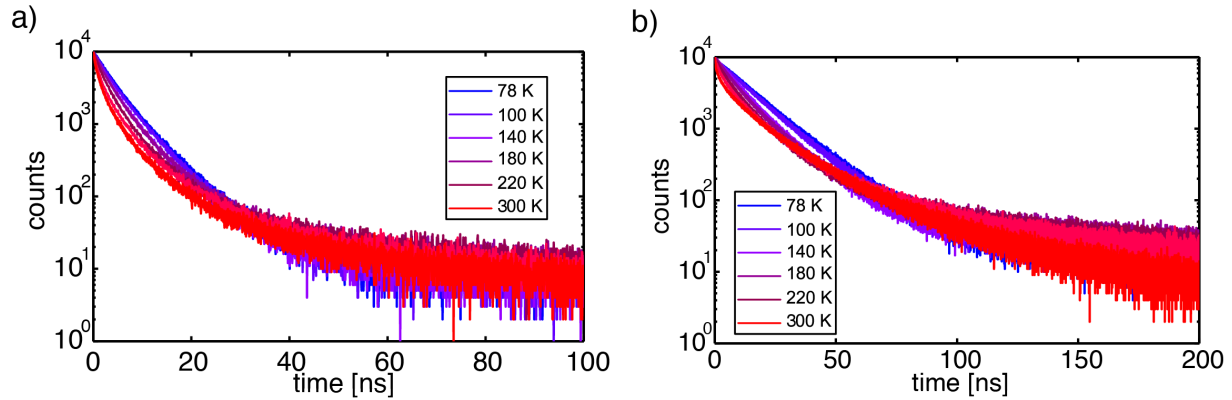
Figure 4.2. Example PL lifetime decays of ferrocene-functionalized QDs. TRPL data for the 4.1 nm QDs exchanged with (a) Me_8FcOC_6SH and (b) FcC_6SH taken over the 78 – 300 K temperature range.
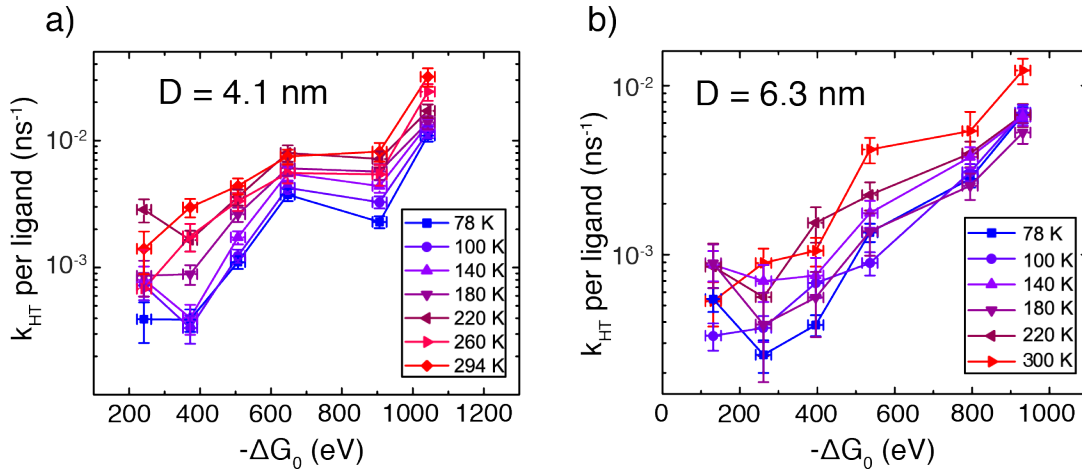
Figure 4.3. Temperature dependent rate vs. driving force plots from TRPL data. Hole transfer rate constants per ligand (k_{HT}) as a function of driving force and temperature for (a) the 4.1 nm QDs and (b) the 6.3 nm QDs. Rates were derived from Equation (**16**. The same six ferrocene ligands were used as in Chapter 3.

The second strategy for obtaining temperature dependent hole transfer rates relied on the fact that the QD emission peak energy is temperature dependent, and, furthermore, that it is nearly linear in temperature over the 80 – 300 K range.[95] We could therefore place a 78 K sample into an integrating sphere and record PLQYs while the sample warmed to RT, and then use the emission peak energy to determine the corresponding temperature. This process was repeated 5-7 times for each sample to obtain accurate QY vs. emission energy data. The temperature dependent QY for native QDs ($QY_0(T)$), the QY for ferrocene-functionalized QDs ($QY_{Fc}(T)$), and a separately determined native lifetime ($\tau_0(T)$) could then be used with the following equation to determine the hole transfer rate.

$$Nk_{ht}(T) = \tau_0(T)^{-1}\left(\frac{QY_0(T)}{QY_{Fc}(T)} - 1\right)$$

(17)

Two methods were employed to process the data using this equation (Figure 4.4). In method 1, the raw QY vs. emission peak energy was converted to QY vs. T with a linear E_g vs. T

approximation, which was then binned before applying Equation (17. In method 2, the QY data was binned relative to the peak emission energy and rates were extracted as a function of peak emission energy. In the last step, the binned energies were converted to temperature based on measurements performed in a cryostat. These two methods produce qualitatively similar results as can be seen in Figure 4.5.
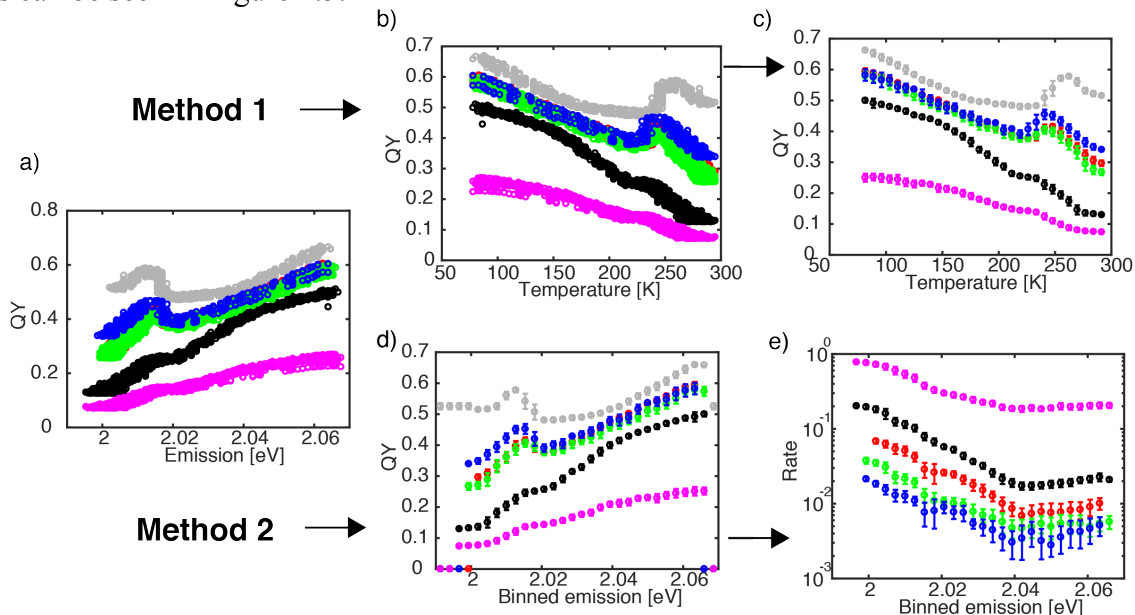
Figure 4.4. Two methods for processing PLQY data from integrating sphere. (a) raw QY vs. emission data. (b-c) Data obtained via method 1 described in text. (d-e) Data obtained from method 2. Colors correspond to Me_8FcOC_6SH (magenta), FcC_6SH (black), $FcOC_6SH$ (red), $BrFcOC_6SH$ (green), and Br_2FcOC_6SH (blue).
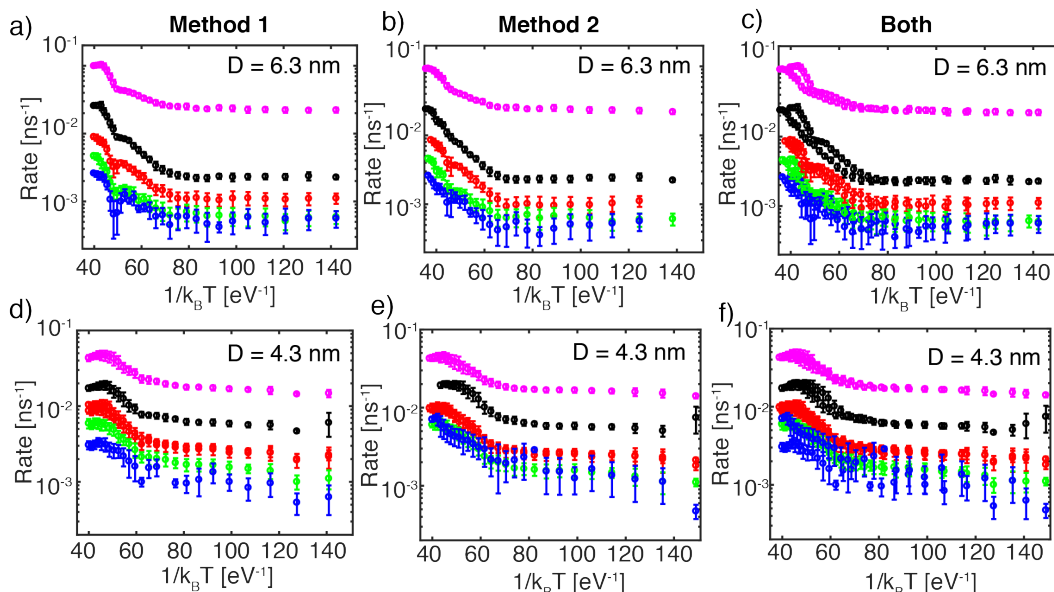
Figure 4.5. Comparison of two data processing methods with Arrhenius plots. (a,d) Data from method 1 for 6.3 and 4.3 nm QDs. (b,e) Data from method 2 for 6.3 and 4.3 nm QDs. (c,f) Data from both methods overlain. Colors correspond to Me_8FcOC_6SH (magenta), FcC_6SH (black), $FcOC_6SH$ (red), $BrFcOC_6SH$ (green), and Br_2FcOC_6SH (blue).

36

Due to sample limitations, the 4.1 nm QDs used in Chapter 3 and the TRPL studies were replaced for a similar sample with a diameter of 4.3 nm and the same sized CdSe core. The same 6.3 nm QD sample was used for all experiments. The rate as a function of driving force over a range of temperatures is shown in Figure 4.6 (data obtained using method 1).
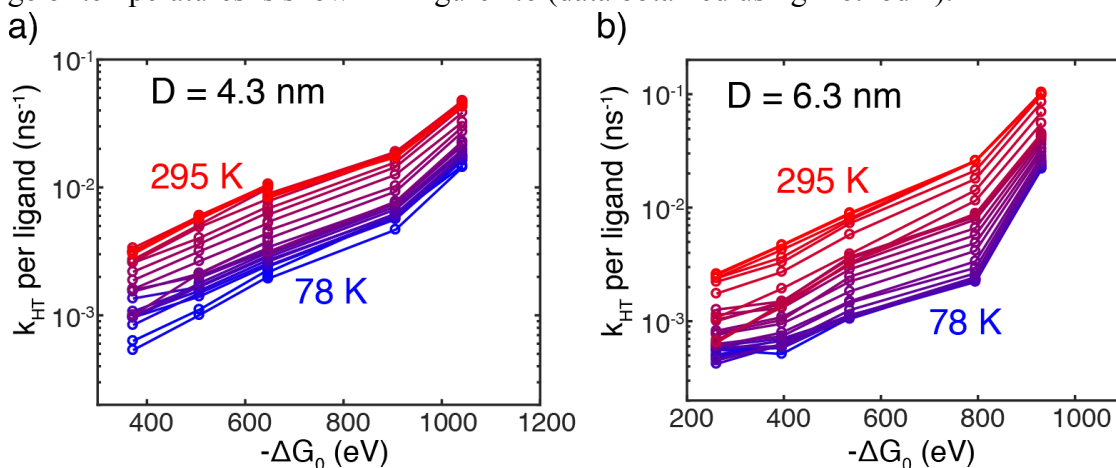
Figure 4.6. Temperature dependent rate vs. driving force plots from PLQY data. Hole transfer rates were extracted from temperature-dependent PLQY measurements performed in an integrating sphere using Equation **(17**. This data excludes the lowest driving force ligand, Br_3FcOC_6SH. The temperature range covered is from 78 K (blue) to 295 K (red).

There are clearly similarities and differences between the TRPL (Figure 4.6) and PLQY (Figure 4.3) derived hole transfer rates. The TRPL data for the 4.1 nm QDs shows inverted kinetics at low temperature between the third and second highest driving force ligands ($FcOC_6SH$ and FcC_6SH). It is unclear whether this a manifestation of the discrete nature of the conduction band states that compose the Auger-assisted model or simply error. Nevertheless, both the TRPL and PLQY data show that the rate decreases by nearly a factor of ten upon cooling to 78 K. Although the absolute rates differ for each ferrocene ligand, dependent on driving force, the temperature dependence appears to be rather consistent, as can be seen in the Arrhenius plots of Figure 4.5. The TRPL data provides coarser data in temperature and was generally susceptible to larger errors due to inconsistencies in fitting the data. Therefore, the remainder of the analysis is focused on the PLQY data shown in Figure 4.5 and Figure 4.6.

As a point of comparison to the experimental data, let us return to the three different Marcus-based electron transfer models from Chapter 1, shown in Figure 1.5. This figure contains a two-state Marcus model common to molecular systems, a multi-state Marcus model (such as the Auger-assisted model) and a model involving a continuum of final states such as what is observed in bulk systems. It is clear from Figure 1.5 that none of these formulations of Marcus theory reproduce the consistent and sizeable temperature dependence of the rate across a range of driving forces, as is observed in the experimental data (Figure 4.6).
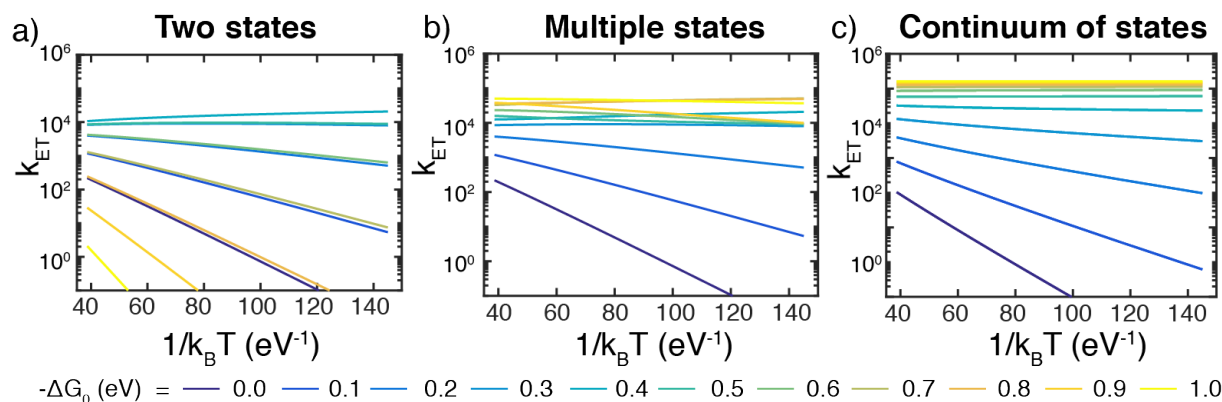
Figure 4.7. Arrhenius plots of different formulations of Marcus Theory. The three formulations of Marcus theory are outlined in **Figure 1.5**. (a) Two state model, (b) multiple state model, and (c) continuum of states model. Fitted slopes to these curves were used to generate the data in **Figure 4.8**.

To make this comparison clearer, Arrhenius plots of the Marcus based models were also prepared with a series of curves dependent on driving force (Figure 4.7). The analogous Arrhenius plots for each ferrocene ligand (ranging in driving forces) on the 6.3 nm QDs are shown in Figure 4.8a. These experimental plots exhibit a high temperature activated regime with extracted activation energies of 60 – 90 meV depending on the ligand as well as a low temperature activationless regime, which will be addressed later. The simulated Arrhenius plots for the Marcus-based models (all assumed to be in the activated regime) are nearly linear across all driving forces studied. The slight deviation from linearity comes from the $T^{-1/2}$ factor in the Marcus equation. Driving force dependent activation energies were extracted by fitting the temperature dependent curves to lines, and the results are shown with the experimental data in Figure 4.8b. Clearly, the consistently high activation energies observed in the experimental data do not fit to any single step Marcus model, which exhibit either low activation energies or driving force dependent activation energies. Therefore, a two-step mechanism is proposed and elaborated upon in the next section.
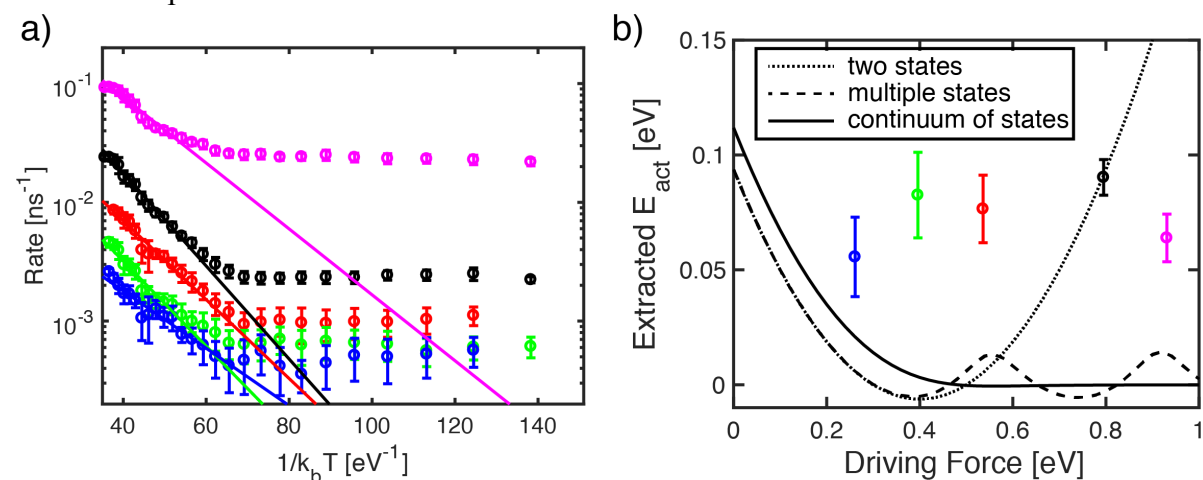
Figure 4.8. Arrhenius behavior compared with different versions of Marcus Theory. a) Arrhenius plot of the rate of hole transfer for the five ligands studied via temperature dependent PLQY for the 6.3 nm QDs (the same data as in **Figure 4.6**b). Solid lines represent linear fits over the activated regime. (b) The driving force dependence of extracted Arrhenius slopes (effective activation energies) for the experimental data (circles) and for the models presented in **Figure 1.5**. Br_2FcOC_6SH (blue), $BrFcOC_6SH$ (green), $FcOC_6SH$ (red), FcC_6SH (black), $Me_8FcOC6SH$ (magenta).

4.4   Experimental evidence for trap-mediated hole transfer

The consistency in the temperature dependence across all ligands suggests that some process independent of the ferrocene driving force is giving rise to this temperature dependence. I propose that this process is the trapping of holes on the QD surface, specifically reversible trapping. As was mentioned at the beginning of this chapter, reversible traps have been used to explain temperature dependent PL behavior and the computational work on the CdSe/CdS rod with FcC$_6$SH suggested that trap-mediated hole transfer would outcompete direct transfer if the trap was less than 200 meV below the valence band (higher in energy).[49] It should be noted that our measurements can only detect *reversible* trap mediated transfer. Irreversible traps, which lead to non-radiative recombination, are accounted for in the k_{nr} rate measured for the native QDs. Reversible trapping, however, allows for band edge PL to persist in the absence of a terminal acceptor such as ferrocene.
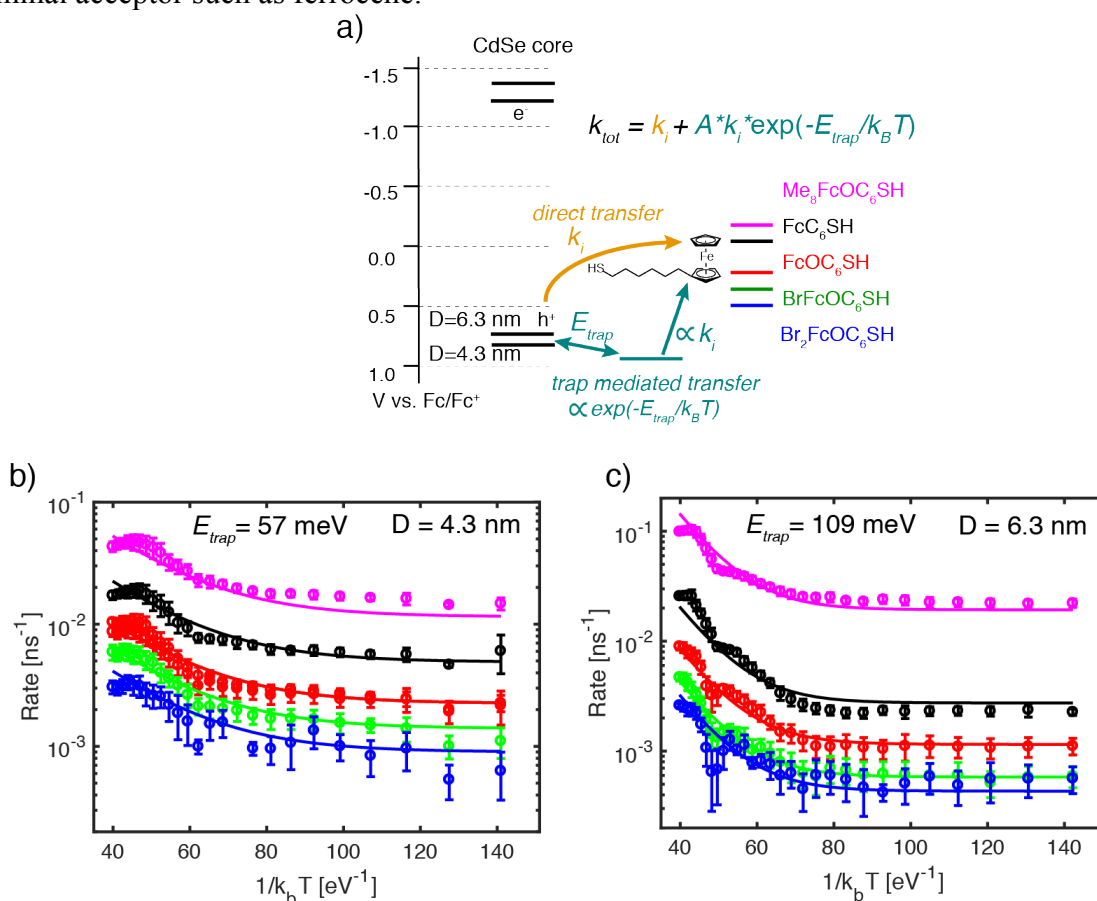
Figure 4.9. Trap mediated charge transfer model and fits of this model to the data. (a) Schematic of the model that assumes the charge transfer rate is a sum of two pathways: direct transfer and trap mediated transfer. The latter pathway relies on thermal excitation of the hole into a trap of energy E$_{trap}$ relative to the valence band, and is therefore temperature dependent. (b-c) Arrhenius plot for the five ferrocene molecules studied on (b) 4.3 and (c) 6.3 nm QDs with fits to the trap mediated model along with the extracted values for E$_{trap}$.

Based on these observations, a model was constructed that permits surface trap-mediated hole transfer. This model assumes that an equilibrium can be established between the band edge state and the trap state with relative populations dictated by a Boltzmann factor, in accordance with the computational model described in Figure 4.1. To make the model as simple as possible I

assume the existence of a single trap state with an energy of E_{trap} below the QD valence band. It is also assumed that the driving force dependence of hole transfer from the trap state will be the same as for the direct transfer, just scaled by some QD dependent factor, *A,* as shown in the following equation:

$$k_{i,tot}(T) = k_i + A * k_i * exp\left(-\frac{E_{trap}}{k_B T}\right)$$
(18)

Where k_i represents the direct transfer rate for ligand *i*. This model is schematically illustrated in Figure 4.9a.

Global fits of Equation (18 to the data for the 4.3 nm and 6.3 nm QDs were performed over the five ligands measured to extract values of E_{trap} (Figure 4.9b,c). The trap energy for the larger QDs is about 50 meV larger than for the smaller QDs. This is approximately the energy difference expected for the valence bands of these two different sized QDs, and it therefore supports the notion that traps are molecular in nature. That is, the trap energy is not affected by QD size, but as the QD size increases the E_{trap} value increases in accordance with the changing position of the valence band.

It is worth mentioning how Equation (18 reproduces the data and how other versions would also work. In this model, the values for k_i are temperature independent. Therefore, at low temperatures, when the trap state is not significantly populated the transfer rate just becomes the temperature independent k_i. At high temperatures, the faster trap-mediated rate grows in proportionally with the trap population, thus reproducing an activated regime. However, k_i should follow Marcus theory and would therefore be moderately temperature dependent. Figure 4.8b suggests that the activation energies are quite low for the multiple state model (i.e. Auger-assisted model) with driving forces greater than 200 meV, so the temperature dependence of k_i would be rather small. To confirm this assumption, a model was constructed in which the values for k_i were dictated by the Auger-assisted model (Equation (15) and were able to qualitatively reproduce the experimental Arrhenius behavior. See Figure 4.10. There are clearly discrepancies between the model and the experimental data primarily due to errors in the driving force dependence (also reflected in Figure 3.12). That being said, the temperature dependence of this combined model is quite similar to both the experimental data and the simple trap mediated model used to directly fit the data in Figure 4.9.

Finally, the presence of an activated and temperature independent regime could alternatively be explained by a quantized formulation of Marcus theory in which transfer is no longer activated when $k_B T < \hbar \omega$, where ω corresponds to the relevant vibrational frequency for the nuclear rearrangement associated with charge transfer (i.e. the harmonic oscillator frequency for the parabolic potentials shown in Figure 1.3).[96] In this case, the activated regime would be dictated by Marcus-based hole transfer to a trap state (instead of a Boltzmann population). However, the conclusion that trap-mediated transfer must be present would not be affected.

The observation of significant trap-mediated transfer necessitates a revised understanding of the room temperature hole transfer presented in Chapters 2 and 3, which assumed direct transfer.[50,63] The hole transfer from the trap state to the ferrocene clearly does not exhibit an inverted regime, so a multi-state Marcus model would be necessary to fit the behavior. The Auger-assisted model still appears to be a valid way to obtain these multiple states. In this interpretation, the hole transfer from the trap site (rather than direct transfer) to ferrocene is coupled to electron excitation in the conduction band. Alternatively, this hole transfer could be coupled to electron trapping, which would result in the same observed behavior.
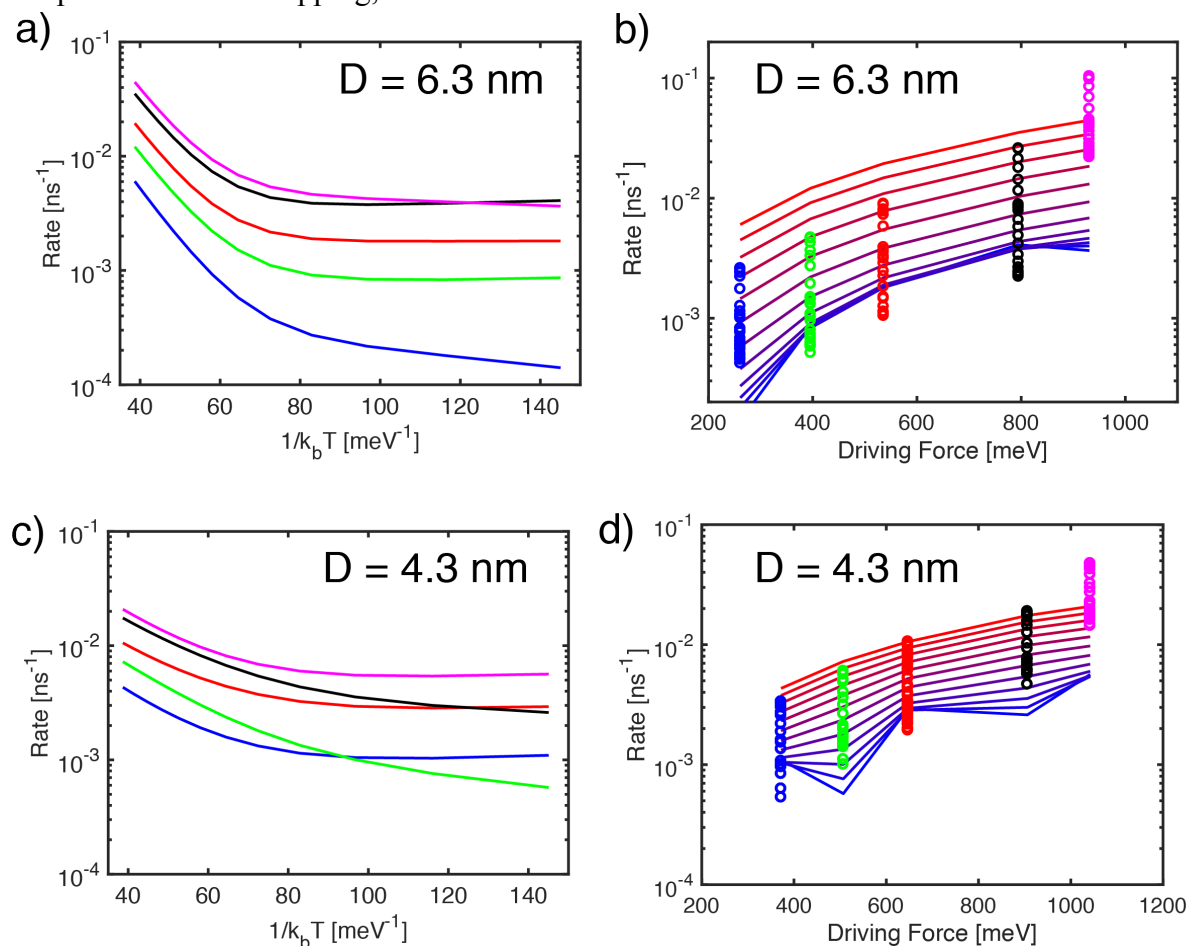
Figure 4.10. Combining the Auger-assisted model with the trap-mediated model. The proportionality constant, A, and E_{trap} values were input in a combined model in which the k_i values were derived from the Auger-assisted model presented in Equation **(15** and shown in **Figure 3.12**a. (a,c) Arrhenius plots based on this model. (b,d) Solid lines show the temperature dependent rate as a function of driving force predicted by this combined model from 80 K (red) to 300 K (blue). The data points represent the experimental data for each ligand (same data as **Figure 4.6**). Colors correspond to Me_8FcOC_6SH (magenta), FcC_6SH (black), $FcOC_6SH$ (red), $BrFcOC_6SH$ (green), and Br_2FcOC_6SH (blue).

The work presented in this chapter highlights the importance of shallow and reversible traps in QD systems. In particular, efficient and controlled extraction of charge can take advantage of the presence of these traps if they are properly understood. The determination of effective trap energies in this chapter offers the first steps towards better understanding these electronic states. Furthermore, this work highlights the benefits of designing multi-step charge

transfer systems that can always be designed to be faster than single step, longer range, transfer due to the exponential nature of the tunneling efficiency.

Chapter 5 : Compiling previous work

In Chapters 2-4, I have described in detail a model system for studying hole transfer from QDs to surface bound ferrocene molecules. I have demonstrated how the coupling (Chapter 2), driving force (Chapter 3), and shallow traps (Chapter 4) can all affect the hole transfer rate. In this chapter, I aim to apply the lessons learned in the first four chapters of this dissertation to compile previously published work on hole transfer with the goal of creating a generalizable model for hole transfer. This section is primarily focused on cadmium chalcogenide QDs and divides hole transfer studies into two broad categories: native traps and engineered traps.

5.1   Native traps

Native hole traps are often ill-defined and poorly understood, but are believed to be composed primarily of under-coordinated surface chalcogen atoms. For example, in CdSe QDs the conduction and valence bands are composed of primarily Cd 5s and Se 4p orbitals, respectively. These unpassivated atomic states can give rise to states within the band gap that can then trap charge (Figure 5.1A). Ligand binding heads can also contribute to hole trapping such as in the case of thiols (Figure 5.1B). As was mentioned previously, native hole traps are particularly interesting since hole trapping is faster than trapping to native electron states and is what is primarily responsible for low PLQYs in CdSe and CdS QDs synthesized via routine methods.[87,97]
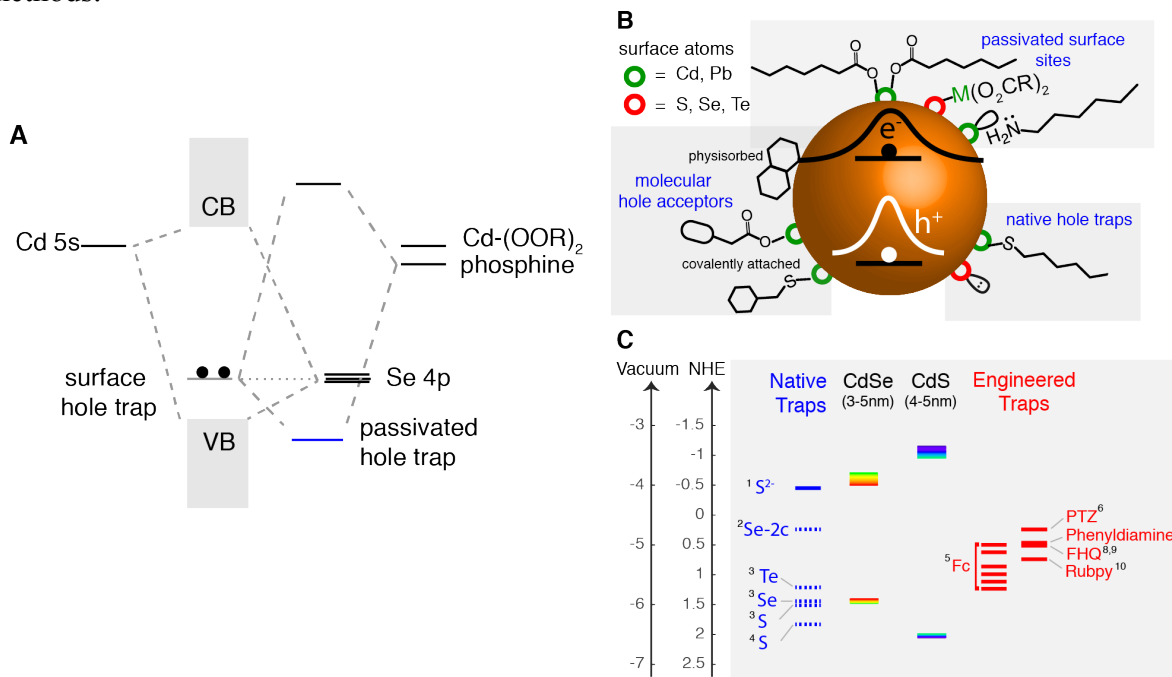
Figure 5.1. Schematic of native and engineered traps. (A) Molecular orbital description of the origin of native hole traps in CdSe QDs. (B) Cartoon of the variety of surface species on metal chalcogenide QDs including engineered molecular hole acceptors, passivated surface sites, and native hole traps either due to thiols or undercoordinated chalcogen atoms. (C) Energy diagram of common sizes of CdSe and CdS QDs with energetic potentials of native and engineered traps found in literature. The dashed and solid lines depict calculated and measured positions, respectively. Superscripts indicate reference: 1 Pu *et al*,[98] 2 Houtepen *et al*.[99] 3 Buckley *et al*.[88] 4 Tarafder *et al* (and Chapter 4).[49] 5 Olshansky *et al* (and Chapter 3).[63] 6 Lian *et al*.[100] 7 Sharma *et al*.[101] 8,9 Cotlet *et al*.[102,103] 10 Sykora *et al*.[19]

CdSe QDs synthesized via the standard nucleation and growth method exhibit 30-70 excess Cd (approximately 10% stoichiometric excess).[67] Post-synthetic surface treatment with successive injections of Se or Cd precursors can produce variable percentages of excess Se and Cd, thereby controlling the number of traps.[104,105] More recent methods to remove the Cd excess layer via a Lewis base can also be used to vary the coverage of excess Cd.[67] Recent work in the Owen and Peng research groups have shed more quantitative insight into these hole traps with the use of time-resolved absorption and PL spectroscopic techniques.[67,87,97,98] Gao and Peng demonstrated that the excess Cd associated with electron traps results in a long-lived decay that is slower than k_r (2.9 x 10^{-2} to 4.2 x 10^{-2} ns^{-1} for 3-5 nm diameter CdSe).[97] On the other hand, excess Se on QDs results in fast PL decays: 1.0 x 10^{-1} to 5.0 x 10^{-1} ns^{-1}. Passivating Se with electron withdrawing phosphine groups and Cd carboxylates improves the PLQY, agreeing with our MO theory depiction of the effect of ligands in drawing trapping levels out of the band gap (Figure 5.1A). Work by Busby et al provides experimental proof that surfacial Se states are hole traps by demonstrating that increasing the amount of unpassivated Se has no effect on the QD electron population (as measured by transient absorption) but substantially reduces the PL lifetime (reflecting shorter excitonic hole lifetimes).[87]

However, without quantification of the number of Se traps, we cannot discern whether the measured hole transfer rate is a result of high k_{ht} and low N or vice versa. Work in the Owen group has utilized quantitative NMR to report the percentage of bound excess Cd, which in turn gives us the number of unpassivated Se sites. Following the PLQY and the lifetime decay over this quantitative range allows us to calculate the rate constant for hole transfer to native Se traps, with the assumption that each Se on the QD is identical. Using a k_r of 3.7 x 10^{-2} ns^{-1},[97] we get a single hole transfer rate to Se of 2.2 x 10^{-3} ns^{-1}. Trapping to an individual acceptor is much slower than k_r, but under normal coverage of around 30 uncoordinated Se per QD, these nonradiative paths collectively compete effectively with k_r to decrease the PLQY. Given our understanding of QD facets and their relative energies, the assumption that each Se on the QD is identical is unlikely true although they are typically within a few hundred meV of each other.[86] Calculated and experimental values of hole traps are shown in Figure 5.1C. Although there is a range of values reported for native traps, most studies tend to place them near the valence band edge in accordance with the observations of reversible trapping mentioned in Chapter 4. In deviation from most studies, Houtepen et al calculates a deep trap associated with Se that lies near the center of the bandgap, with a driving force upward of 1 eV.[99]

While the Peng and Owen groups agree that Cd-carboxylate effectively passivates Se traps, discrepancies in the extent to which PLQY recovers from Se passivation exist. In Peng's work, electron traps, which can still decrease the PLQY of the QD by a factor of 2-3, are passivated with primary amines. This, along with the use of the smaller Cd-formate, which may be able to bind to more Se traps, is likely the reason for the much higher PLQY (nearly unity) achieved for Peng's work on native CdSe QDs.[97]

Sulfur surface traps are analogous to Se and have been known longer to cause diminished PLQY especially in CdSe.[69] Their energetic position varies in literature, but are close to the Se level, with Buckley et al calculating S to be only 70 meV lower in energy[88] than Se and Tarafder et al calculating it to be 270 meV below the valence band of CdSe (See Figure 4.1).[49] Sulfur states form unpassivated S on CdS and bound thiolate ligands have similar hole trapping and are

thought to be similar in energy. Hole transfer to these two similar traps as a function of the CdS shell thickness is shown in Chapter 2 and has also been studied by the Peng group.[50,98]

5.2   Engineered traps

The second class of traps, engineered traps, is also described in Figure 5.1B,C. Engineered traps constitute any system in which the electronic state associated with the hole transfer is well-defined and purposefully introduced into the system such as the molecular hole acceptors described in the bulk of this dissertation. Figure 5.1B shows how these molecular hole acceptors can interact with the nanocrystal surface, either through physisorption, or covalent attachment with a variety of binding heads. Energetic positions for reported engineered hole traps (including those described in Chapter 3) are shown in Figure 5.1C in relation to the band positions of CdSe and CdS QDs.

As was mentioned in Chapter 1, it is critical to account for the number of acceptors, their binding geometries, and their energetics when comparing rates between disparate systems. A handful of hole transfer studies in the literature with both native and engineered traps have adequately accounted for these effects such that quantitative comparison is merited. This comparison relies on using appropriate parameters from Marcus theory (and the related Auger-assisted model). The parameters of rate and driving force can be measured experimentally. Reorganization is harder to measure experimentally; however a handful of studies encompassing a range of acceptors, both engineered and native, have calculated or extracted λ from empirical data to be $300 - 600$ meV.[49,63,89,92] This value is likely dominated by inner sphere reorganization of the molecular state. The reorganization energy due to the delocalized excitations on the QD and the outer sphere contributions from the low dielectric solvents and ligands is expected to be minor.

The Marcus parameter of electronic coupling is probably the most difficult to measure. It is proportional to the wave function overlap between the donor and the acceptor electronic states. The valence band position of CdSe and CdS is not strongly affected by size and therefore large differences in hole transfer rates as a function of QD size are likely a result of a change in the hole wave function probability on the surface (which decreases with increasing diameter). In one study, the rate was shown to decrease by a factor of three going from 3.6 nm to 4.6 nm QDs,[102] while in another the rate decreased by a factor of three going from 2.8 nm to 5.3 nm.[106]

As was discussed in Chapter 1, the electronic coupling is also exponentially dependent on distance between donor and acceptor (Equation (3). In Chapter 2, it was shown that the tunneling rate for hole transfer through a CdS shell from CdSe has a damping coefficient of $\beta = 0.24$ Å^{-1}. Another study on hole transfer from CdSe/ZnS QDs varying shell thickness to electrostatically bound fluorine-phenylene based polymerica acceptors (FHQ) found a damping coefficient of 0.28 Å^{-1}.

Since the electronic coupling is most difficult to determine experimentally, we decided to compare the handful of hole transfer studies through the lens of an extrapolated electronic coupling value after fitting with the Auger-assisted model (Equation (15). The reorganization energy was set to 400 meV and the values of $E_{e,i}$ were chosen to match average ($\sim$ 4 nm) CdSe QDs for all curves. Clearly, these values would change between systems and affect the extracted electronic coupling value potentially as much as an order of magnitude. However, the qualitative

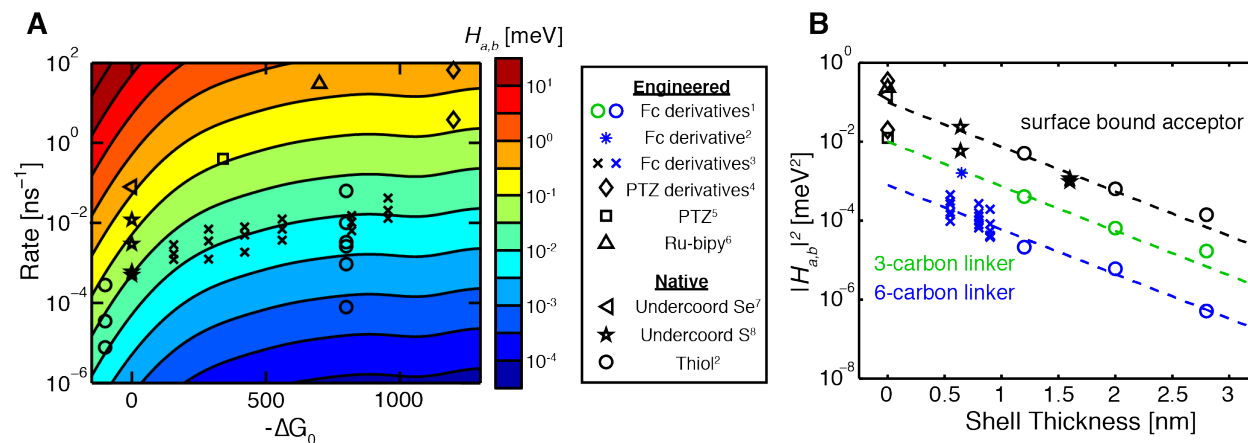relationships over this large range of driving force, rate constant, and coupling are still very useful.

Figure 5.2. Compiled rates vs. driving force for hole transfer. (A) A color map of the electronic coupling as a function of rate and driving force based on the Auger-assisted model (Equation **(15)** with a reorganization energy of 400 meV and conduction band energies given by a standard sized CdSe QD. Experimental data points are overlaid. (B) Electronic coupling squared plotted against the thickness of the barrier (CdS or ZnS), for different acceptor types including fits based on tunneling (Equation **(3)** with $\beta = 0.26$ Å^{-1} (dashed lines). Superscripts correspond to references: 1 Ding *et al* (Chapter 2).[50] 2 Tarafder *et al* (Chapter 4).[49] 3 Olshansky *et al* (Chapter 3). 4 Lian *et al*.[100] 5 Huang *et al*.[46] 6 Sykora *et al*.[19] 7 Busby *et al*.[87] 8 Shen *et al*.[107]

5.3   A generalizable model for hole transfer

Figure 5.2A shows a series of rate vs. driving force curves given by Equation (15, color-coded by calculated values of the electronic coupling. Overlaid on these curves are the individual data points collected from experimental studies. The curve on which these points reside determines their electronic coupling. In Figure 5.2B, the electronic coupling squared (proportional to rate) is plotted as a function of shell thickness for surface bound acceptors, and acceptors that are three and six carbons from the surface. For each of these classes of acceptor, the decay of $|H_{a,b}|^2$ as a function of shell thickness appears exponential (linear on the log plot), in accordance with Equation (3.

The compiled data in Figure 5.2 provides a link between the studies on molecular acceptors on core-only QDs, the molecular acceptors in the model system described in this dissertation, and the molecular-like acceptors that give rise to native traps. Notably, the couplings calculated for the surface bound acceptors match what one would expect from extrapolating the varying shell thickness studies back to zero. Furthermore, it was found that using low driving forces for the native traps (within 100 meV of the band edge) was necessary for obtaining reasonable results in Figure 5.2B, confirming the general consensus that shallow traps dominate on the surface of cadmium chalcogenide QDs.

In this dissertation, I have described in detail the design, synthesis, and characterization of a model system for studying hole transfer from QDs. In Chapter 2, I introduced this model system and showed how it could be used to eliminate complications resultant from irreversible traps by using high PLQY QDs. Furthermore, by accurately quantifying the number of acceptors, the per molecule rate constant for hole transfer could be determined and was shown to depend exponentially on donor-acceptor distance. This model system was further expanded in Chapter 3 to cover an 800 meV range in driving force for hole transfer. The experimentally observed lack

of a Marcus inverted regime led to the implementation of the Auger-assisted multi-state Marcus model, which fit well to the data. The temperature dependence of hole transfer was explored in Chapter 4 and the results suggested that trap-mediated hole transfer is the dominant pathway for charge transfer at room temperature. Finally, in the current chapter I have compared the results obtained with this model system to results obtained by other groups on hole transfer to both native and engineered traps. A generalizable model is presented for interpreting data from hole transfer experiments with CdSe QDs. I hope that the data shown in Figure 5.2 can provide guidance to researchers in predicting hole transfer rates and couplings for new QD systems with varied geometries and energetics, or designing new systems to achieve desirable rates.

References

(1)   Medintz, I. L.; Uyeda, H. T.; Goldman, E. R.; Mattoussi, H. *Nat. Mater.* **2005**, *4*, 435–446.

(2)   Pinaud, F.; Michalet, X.; Bentolila, L. A.; Tsay, J. M.; Doose, S.; Li, J. J.; Iyer, G.; Weiss, S. *Biomaterials* **2006**, *27*, 1679–1687.

(3)   Shirasaki, Y.; Supran, G. J.; Bawendi, M. G.; Bulović, V. *Nat. Photonics* **2013**, *7*, 13–23.

(4)   Kramer, I. J.; Sargent, E. H. *Chem. Rev.* **2014**, *114*, 863–882.

(5)   Chuang, C.-H. M.; Brown, P. R.; Bulović, V.; Bawendi, M. G. *Nat. Mater.* **2014**, *13*, 796–801.

(6)   Kamat, P. V. *Acc. Chem. Res.* **2012**, *45*, 1906–1915.

(7)   Kamat, P. V. *J. Phys. Chem. C* **2008**, *112*, 18737–18753.

(8)   Wilker, M. B.; Schnitzenbaumer, K. J.; Dukovic, G. *Isr. J. Chem.* **2012**, *52*, 1002–1015.

(9)   Han, Z.; Qiu, F.; Eisenberg, R.; Holland, P. L.; Krauss, T. D. *Science* **2012**, *338*, 1321–1324.

(10)   Amirav, L.; Alivisatos, A. P. *J. Phys. Chem. Lett.* **2010**, *1*, 1051–1054.

(11)   Zhao, K.; Pan, Z.; Mora-Seró, I.; Cánovas, E.; Wang, H.; Song, Y.; Gong, X.; Wang, J.; Bonn, M.; Bisquert, J.; Zhong, X. *J. Am. Chem. Soc.* **2015**, *137*, 5602–5609.

(12)   Wu, K.; Lian, T. *Chem. Soc. Rev.* **2016**, *45*, 3781–3810.

(13)   Manzi, A.; Simon, T.; Sonnleitner, C.; Döblinger, M.; Wyrwich, R.; Stern, O.; Stolarczyk, J. K.; Feldmann, J. *J. Am. Chem. Soc.* **2015**, *137*, 14007–14010.

(14)   Wang, C.; Thompson, R. L.; Ohodnicki, P.; Baltrus, J.; Matranga, C. *J. Mater. Chem.* **2011**, *21*, 13452–13457.

(15)   Caputo, J. A.; Frenette, L. C.; Zhao, N.; Sowers, K. L.; Krauss, T. D.; Weix, D. J. *J. Am. Chem. Soc.* **2017**, *139*, 4250–4253.

(16)   Zhang, Z.; Edme, K.; Lian, S.; Weiss, E. A. *J. Am. Chem. Soc.* **2017**, *139*, 4246–4249.

(17)   Knowles, K. E.; Peterson, M. D.; McPhail, M. R.; Weiss, E. A. *J. Phys. Chem. C* **2013**, *117*, 10229–10243.

(18)   Boulesbaa, A.; Issac, A.; Stockwell, D.; Huang, Z.; Huang, J.; Guo, J.; Lian, T. *J. Am. Chem. Soc.* **2007**, *129*, 15132–15133.

(19)   Sykora, M.; Petruska, M. A.; Alstrum-Acevedo, J.; Bezel, I.; Meyer, T. J.; Klimov, V. I. *J. Am. Chem. Soc.* **2006**, *128*, 9984–9985.

(20)   Robel, I.; Kuno, M.; Kamat, P. V. *J. Am. Chem. Soc.* **2007**, *129*, 4136–4137.

(21)   Žídek, K.; Zheng, K.; Ponseca, C. S.; Messing, M. E.; Wallenberg, L. R.; Chábera, P.; Abdellah, M.; Sundström, V.; Pullerits, T. *J. Am. Chem. Soc.* **2012**, *134*, 12110–12117.

(22)   Cánovas, E.; Moll, P.; Jensen, S. A.; Gao, Y.; Houtepen, A. J.; Siebbeles, L. D. A.; Kinge, S.; Bonn, M. *Nano Lett.* **2011**, *11*, 5234–5239.

(23)   Peng, W.; Du, J.; Pan, Z.; Nakazawa, N.; Sun, J.; Du, Z.; Shen, G.; Yu, J.; Hu, J.-S.; Shen, Q.; Zhong, X. *ACS Appl Mater Interfaces* **2017**, *9*, 5328–5336.

(24)   Kamat, P. V.; Christians, J. A.; Radich, J. G. *Langmuir* **2014**, *30*, 5716–5725.

(25)   Abdellah, M.; Marschan, R.; Zidek, K. *J. Phys. Chem. C* **2014**, *118*, 25802–25808.

(26)   Shen, Q.; Kobayashi, J.; Diguna, L. J.; Toyoda, T. *J. Appl. Phys.* **2008**, *103*, 084304.

(27)   Chakrapani, V.; Baker, D.; Kamat, P. V. *J. Am. Chem. Soc.* **2011**, *133*, 9607–9615.

(28)   Robel, I.; Subramanian, V.; Kuno, M.; Kamat, P. V. *J. Am. Chem. Soc.* **2006**, *128*,

2385–2393.

(29)   Mora-Seró, I.; Giménez, S.; Fabregat-Santiago, F.; Gómez, R.; Shen, Q.; Toyoda, T.; Bisquert, J. *Acc. Chem. Res.* **2009**, *42*, 1848–1857.

(30)   Kalisman, P.; Nakibli, Y.; Amirav, L. *Nano Lett.* **2016**, *16*, 1776–1781.

(31)   Zhu, H.; Song, N.; Lv, H.; Hill, C. L.; Lian, T. *J. Am. Chem. Soc.* **2012**, *134*, 11701–11708.

(32)   Wu, K.; Chen, Z.; Lv, H.; Zhu, H.; Hill, C. L. *J. Am. Chem. Soc.* **2014**, *136*, 7708–7716.

(33)   Marcus, R. A.; Sutin, N. *Biochim. Biophys. Acta* **1985**, *811*, 265–322.

(34)   Yu, G.; Gao, J.; Hummelen, J. C.; Wudl, F.; Heeger, A. J. *Science* **1995**, *270*, 1789–1791.

(35)   Ardo, S.; Meyer, G. J. *Chem. Soc. Rev.* **2009**, *38*, 115–164.

(36)   Yang, Z.; Zhang, J.; Kintner-Meyer, M. C. W.; Lu, X.; Choi, D.; Lemmon, J. P.; Liu, J. *Chem. Rev.* **2011**, *111*, 3577–3613.

(37)   Chen, X.; Shen, S.; Guo, L.; Mao, S. S. *Chem. Rev.* **2010**, *110*, 6503–6570.

(38)   Miller, J. R.; Calcaterra, L. T.; Closs, G. L. *J. Am. Chem. Soc.* **1984**, *106*, 3047–3049.

(39)   Gray, H. B.; Winkler, J. R. *Proc. Natl. Acad. Sci.* **2005**, *102*, 3534–3539.

(40)   Asbury, J. B.; Hao, E.; Wang, Y.; Ghosh, H. N.; Lian, T. *J. Phys. Chem. C* **2001**, *105*, 4545–4557.

(41)   Chidsey, C. E. *Science* **1991**, *251*, 919–922.

(42)   Huang, J.; Stockwell, D.; Huang, Z.; Mohler, D. L.; Lian, T. *J. Am. Chem. Soc.* **2008**, *130*, 5632–5633.

(43)   Zhu, H.; Song, N.; Lian, T. *J. Am. Chem. Soc.* **2010**, *132*, 15038–15045.

(44)   Zhu, H.; Yang, Y.; Hyeon-Deuk, K.; Califano, M.; Song, N.; Wang, Y.; Zhang, W.; Prezhdo, O. V.; Lian, T. *Nano Lett.* **2014**, *14*, 1263–1269.

(45)   Morris-Cohen, A. J.; Frederick, M. T.; Cass, L. C.; Weiss, E. A. *J. Am. Chem. Soc.* **2011**, *133*, 10146–10154.

(46)   Huang, J.; Huang, Z.; Jin, S.; Lian, T. *J. Phys. Chem. C* **2008**, *112*, 19734–19738.

(47)   Dorokhin, D.; Tomczak, N.; Velders, A. H.; Reinhoudt, D. N.; Vancso, G. J. *J. Phys. Chem. C* **2009**, *113*, 18676–18680.

(48)   Malicki, M.; Knowles, K. E.; Weiss, E. A. *Chem. Commun.* **2013**, *49*, 4400–4402.

(49)   Tarafder, K.; Surendranath, Y.; Olshansky, J. H.; Alivisatos, A. P.; Wang, L.-W. *J. Am. Chem. Soc.* **2014**, *136*, 5121–5131.

(50)   Ding, T. X.; Olshansky, J. H.; Leone, S. R.; Alivisatos, A. P. *J. Am. Chem. Soc.* **2015**, *137*, 2021–2029.

(51)   Busby, E.; Anderson, N. C.; Owen, J. S.; Sfeir, M. Y. *J. Phys. Chem. C* **2015**, *119*, 27797–27803.

(52)   Gao, Y.; Peng, X. *J. Am. Chem. Soc.* **2015**, *137*, 4230–4235.

(53)   Pu, C.; Peng, X. *J. Am. Chem. Soc.* **2016**, *138*, 8134–8142.

(54)   Jones, M.; Lo, S. S.; Scholes, G. D. *Proc. Natl. Acad. Sci.* **2009**, *106*, 3011–3016.

(55)   Jones, M.; Scholes, G. D. *J. Mater. Chem.* **2010**, *20*, 3533–3538.

(56)   Mooney, J.; Krause, M. M.; Saari, J. I.; Kambhampati, P. *Phys. Rev. B* **2013**, *87*, 081201.

(57)   Krause, M. M.; Kambhampati, P. *Phys. Chem. Chem. Phys.* **2015**, *17*, 18882–18894.

(58)   Li, X.; Nichols, V. M.; Zhou, D.; Lim, C.; Pau, G. S. H.; Bardeen, C. J.; Tang, M. L. *Nano Lett.* **2014**, *14*, 3382–3387.

(59)   Hens, Z.; Martins, J. C. *Chem. Mater.* **2013**, *25*, 1211–1221.

(60)   Klimov, V. I.; McBranch, D. W.; Leatherdale, C. A.; Bawendi, M. G. *Phys. Rev. B* **1999**, *60*, 13740.

(61)   Klimov, V. I.; Mikhailovsky, A. A.; McBranch, D. W.; Leatherdale, C. A.; Bawendi, M. G. *Phys. Rev. B* **2000**, *61*, R13349.

(62)   Robel, I.; Gresback, R.; Kortshagen, U.; Schaller, R. D.; Klimov, V. I. *Phys. Rev. Lett.* **2009**, *102*, 177404.

(63)   Olshansky, J. H.; Ding, T. X.; Lee, Y. V.; Leone, S. R.; Alivisatos, A. P. *J. Am. Chem. Soc.* **2015**, *137*, 15567–15575.

(64)   Andrea M Munro; Ilan Jen-La Plante; Marsha S Ng, A.; Ginger, D. S. *J. Phys. Chem. C* **2007**, *111*, 6220–6227.

(65)   Ji, X.; Copenhaver, D.; Sichmeller, C.; Peng, X. *J. Am. Chem. Soc.* **2008**, *130*, 5726–5735.

(66)   Bullen, C.; Mulvaney, P. *Langmuir* **2006**, *22*, 3007–3013.

(67)   Anderson, N. C.; Hendricks, M. P.; Choi, J. J.; Owen, J. S. *J. Am. Chem. Soc.* **2013**, *135*, 18536–18548.

(68)   She, C.; Demortière, A.; Shevchenko, E. V.; Pelton, M. *J. Phys. Chem. Lett.* **2011**, *2*, 1469–1475.

(69)   Wuister, S. F.; de Mello Donegá, C.; Meijerink, A. *J. Phys. Chem. B* **2004**, *108*, 17393–17397.

(70)   Wider, G.; Dreier, L. *J. Am. Chem. Soc.* **2006**, *128*, 2571–2576.

(71)   Gomes, R.; Hassinen, A.; Szczygiel, A.; Zhao, Q.; Vantomme, A.; Martins, J. C.; Hens, Z. *J. Phys. Chem. Lett.* **2011**, *2*, 145–152.

(72)   Adams, D. M.; Brus, L.; Chidsey, C. E. D.; Creager, S.; Creutz, C.; Kagan, C. R.; Kamat, P. V.; Lieberman, M.; Lindsay, S.; Marcus, R. A.; Metzger, R. M.; Michel-Beyerle, M. E.; Miller, J. R.; Newton, M. D.; Rolison, D. R.; Sankey, O.; Schanze, K. S.; Yardley, J.; Zhu, X. *J. Phys. Chem. B* **2003**, *107*, 6668–6697.

(73)   Inkpen, M. S.; Du, S.; Driver, M.; Albrecht, T.; Long, N. J. *Dalton Trans.* **2013**, *42*, 2813–2816.

(74)   Tindale, J. J.; Hartlen, K. D.; Alizadeh, A.; Workentin, M. S.; Ragogna, P. J. *Chem. Eur. J.* **2010**, *16*, 9068–9075.

(75)   Zou, C.; Wrighton, M. S. *J. Am. Chem. Soc.* **1990**, *112*, 7578–7584.

(76)   García-Santamaría, F.; Chen, Y.; Vela, J.; Schaller, R. D.; Hollingsworth, J. A.; Klimov, V. I. *Nano Lett.* **2009**, *9*, 3482–3488.

(77)   Zhu, H.; Song, N.; Rodríguez-Córdoba, W.; Lian, T. *J. Am. Chem. Soc.* **2012**, *134*, 4250–4257.

(78)   Eshet, H.; Grünwald, M.; Rabani, E. *Nano Lett.* **2013**, *13*, 5880–5885.

(79)   Noviandri, I.; Brown, K. N.; Fleming, D. S.; Gulyas, P. T.; Lay, P. A.; Masters, A. F.; Phillips, L. *J. Phys. Chem. B* **1999**, *103*, 6713–6722.

(80)   Jasieniak, J.; Smith, L.; Embden, J. V.; Mulvaney, P.; Califano, M. *J. Phys. Chem. C* **2009**, *113*, 19468–19474.

(81)   Yu, W. W.; Qu, L.; Guo, W.; Peng, X. *Chem. Mater.* **2003**, *15*, 2854–2860.

(82)   Hyeon-Deuk, K.; Kim, J.; Prezhdo, O. V. *J. Phys. Chem. Lett.* **2014**, 244–249.

(83)   Ekimov, A. I.; Kudryavtsev, I. A.; L Efros, Al; Yazeva, T. V.; Hache, F.; Schanne-Klein, M. C.; Rodina, A. V.; Ricard, D.; Flytzanis, C. *J. Opt. Soc. Am. B* **1993**, *10*, 100–107.

(84)   Rinehart, J. D.; Schimpf, A. M.; Weaver, A. L.; Cohn, A. W.; Gamelin, D. R. *J. Am. Chem. Soc.* **2013**, *135*, 18782–18785.

(85)   Norris, D.; Bawendi, M. *Phys. Rev., B Condens. Matter* **1996**, *53*, 16338–16346.

(86)   Voznyy, O.; Sargent, E. H. *Phys. Rev. Lett.* **2014**, *112*, 157401.

(87)   Busby, E.; Anderson, N. C.; Owen, J. S.; Sfeir, M. Y. *J. Phys. Chem. C* **2015**, *119*, 27797–27803.

(88)   Buckley, J. J.; Couderc, E.; Greaney, M. J.; Munteanu, J.; Riche, C. T.; Bradforth, S. E.; Brutchey, R. L. *ACS Nano* **2014**, *8*, 2512–2521.

(89)   Jones, M.; Lo, S. S.; Scholes, G. D. *Proc. Natl. Acad. Sci.* **2009**, *106*, 3011–3016.

(90)   Jones, M.; Lo, S. S.; Scholes, G. D. *J. Phys. Chem. C* **2009**, *113*, 18632–18642.

(91)   Mooney, J.; Krause, M. M.; Saari, J. I.; Kambhampati, P. *J. Chem. Phys.* **2013**, *138*, 204705.

(92)   Mooney, J.; Krause, M. M.; Saari, J. I.; Kambhampati, P. *Phys. Rev. B* **2013**, *87*, 081201.

(93)   Kambhampati, P. *Chemical Physics* **2015**, *446*, 92–107.

(94)   Rabouw, F. T.; Kamp, M.; van Dijk-Moes, R. J. A.; Gamelin, D. R.; Koenderink, A. F.; Meijerink, A.; Vanmaekelbergh, D. *Nano Lett.* **2015**, *15*, 7718–7725.

(95)   Balan, A. D.; Eshet, H.; Olshansky, J. H.; Lee, Y. V.; Rabani, E.; Alivisatos, A. P. *Nano Lett.* **2017**, *17*, 1629–1636.

(96)   Jortner, J. *J. Chem. Phys.* **1976**, *64*, 4860–4867.

(97)   Gao, Y.; Peng, X. *J. Am. Chem. Soc.* **2015**, *137*, 4230–4235.

(98)   Pu, C.; Peng, X. *J. Am. Chem. Soc.* **2016**, *138*, 8134–8142.

(99)   Houtepen, A. J.; Hens, Z.; Owen, J. S.; Infante, I. *Chem. Mater.* **2017**, *29*, 752–761.

(100)   Lian, S.; Weinberg, D. J.; Harris, R. D.; Kodaimati, M. S.; Weiss, E. A. *ACS Nano* **2016**, *10*, 6372–6382.

(101)   Sharma, S. N.; Pillai, Z. S.; Kamat, P. V. *J. Phys. Chem. B* **2003**, *107*, 10088–10093.

(102)   Zang, H.; Routh, P. K.; Alam, R.; Maye, M. M.; Cotlet, M. *Chem. Commun.* **2014**, *50*, 5958–5960.

(103)   Xu, Z.; Hine, C. R.; Maye, M. M.; Meng, Q.; Cotlet, M. *ACS Nano* **2012**, *6*, 4984–4992.

(104)   Jasieniak, J.; Mulvaney, P. *J. Am. Chem. Soc.* **2007**, *129*, 2841–2848.

(105)   Li, J. J.; Wang, Y. A.; Guo, W.; Keay, J. C.; Mishima, T. D.; Johnson, M. B.; Peng, X. *J. Am. Chem. Soc.* **2003**, *125*, 12567–12575.

(106)   Arvani, M.; Virkki, K.; Abou-Chahine, F.; Efimov, A.; Schramm, A.; Tkachenko, N. V.; Lupo, D. *Physical Chemistry Chemical Physics* **2016**, *18*, 27414–27421.

(107)   Shen, Y.; Tan, R.; Gee, M. Y.; Greytak, A. B. *ACS Nano* **2015**, *9*, 3345–3359.

(108)   Sünkel, K.; Bernhartzeder, S. *J. Organomet. Chem.* **2011**, *696*, 1536–1540.

(109)   Menzel, K.; Fisher, E. L.; DiMichele, L.; Frantz, D. E.; Nelson, T. D.; Kress, M. H. *J. Org. Chem.* **2006**, *71*, 2188–2191.

(110)   Goeltz, J. C.; Kubiak, C. P. *Organometallics* **2011**, *30*, 3908–3910.

(111)   Carbone, L.; Nobile, C.; De Giorgi, M.; Sala, F. D.; Morello, G.; Pompa, P.; Hytch, M.; Snoeck, E.; Fiore, A.; Franchini, I. R.; Nadasan, M.; Silvestre, A. F.; Chiodo, L.; Kudera, S.; Cingolani, R.; Krahne, R.; Manna, L. *Nano Lett.* **2007**, *7*, 2942–2950.

(112)   Chen, O.; Zhao, J.; Chauhan, V. P.; Cui, J.; Wong, C.; Harris, D. K.; Wei, H.; Han, H.-S.; Fukumura, D.; Jain, R. K.; Bawendi, M. G. *Nat. Mater.* **2013**, *12*, 445–451.

(113)   Würth, C.; Grabolle, M.; Pauli, J.; Spieles, M.; Resch-Genger, U. *Anal. Chem.* **2011**,

83, 3431–3439.

(114) Bronstein, N. D.; Yao, Y.; Xu, L.; O'Brien, E.; Powers, A. S.; Ferry, V. E.; Alivisatos, A. P.; Nuzzo, R. G. *ACS Nano* **2015**, *2*, 1576–1583.

Appendix A: Synthetic methods

A.1   Synthesis of ferrocene derivatives

Synthetic details for FcC$_3$SH, used in Chapter 2, may be found in the Supporting Information of our published work.[50] The following syntheses correspond to the ferrocene derivatives described in Chapter 3. The synthesis is schematically shown in Figure 3.2.

A.1.1   Chemicals

6-(Ferrocenyl)hexanethiol (FcC6SH), bromoferrocene (BrFc), n-butyllithium solution (n-BuLi, 1.6 M in hexanes), 2,2,6,6-tetramethylpiperidine (TMP, $\geq$ 99.0%), zinc chloride solution (ZnCl$_2$, 1.9 M in 2-methyltetrahydrofuran), 1,1,2,2-tetrabromoethane (TBE, 98%), bromine (Br$_2$, $\geq$ 99.5%), iron(III) chloride (FeCl$_3$, 97%), ferrocene (Fc, 98%, sublimed), 6-bromohexanoyl chloride (97%), aluminum chloride (AlCl$_3$, $\geq$ 99.0%), tetrabutylammonium fluoride solution (TBAF, 1.0 M in tetrahydrofuran), chloroform-d (CDCl$_3$, 99.8 atom % D), tetrabutylammonium hexafluorophosphate (TBA-PF$_6$, $\geq$ 99.0%) and silver nitrate (AgNO$_3$, 99.9999%) were purchased from Sigma-Aldrich and used as received. Bis-(tetramethylcyclopentadienyl)-iron (Me$_8$Fc, 98%), and bis-(pentamethylcyclopentadienyl)-iron (Fc*, 99%) were purchased from STREM. Other chemicals used include bis(trimethylsilyl)sulfide ((TMS)$_2$S, TCI America), silica gel (SiliaFlash P60, 40-63 μm, Silicycle), magnesium sulfate (MgSO$_4$, EMD), sodium chloride (NaCl, EMD), sodium bicarbonate (NaHCO$_3$, EMD), and the anhydrous solvents chloroform, acetone, tetrahydrofuran (THF), hexanes, dichloromethane (DCM), ethyl acetate, and acetonitrile.

A.1.2   1,2-dibromoferrocene (Br2Fc) and 1,2,3-tribromoferrocene (Br3Fc)

To achieve high specificity towards the desired products, an ortho-lithiation with lithium tetramethylpiperidide was performed on either BrFc or Br$_2$Fc followed by a transmetallation with ZnCl$_2$ to produce the less reactive aryl-zinc species prior to bromination with either Br$_2$ or TBE, thus preventing over-bromination. This strategy allowed for controlled successive ortho-additions of bromine (Figure A1).[108,109] Br$_3$Fc was synthesized from Br$_2$Fc with a high enough yield that a simple column and recrystallization resulted in pure Br$_3$Fc. However, bromination of BrFc to make Br$_2$Fc had a much lower yield, resulting in a 60:40 ratio of Br$_2$Fc to BrFc. Since many of the standard purification methods fail to separate halogenated ferrocenes, an electrochemical technique was employed.[110] Iron (III) chloride has a redox potential between Br$_2$Fc and BrFc, so exposure of a mixture of BrFc and Br$_2$Fc in an organic solvent to aqueous FeCl$_3$ preferentially oxidizes BrFc, thus transferring it to the aqueous phase as BrFc$^+$. Repeating this purification process multiple times resulted in pure Br$_2$Fc in the organic phase.
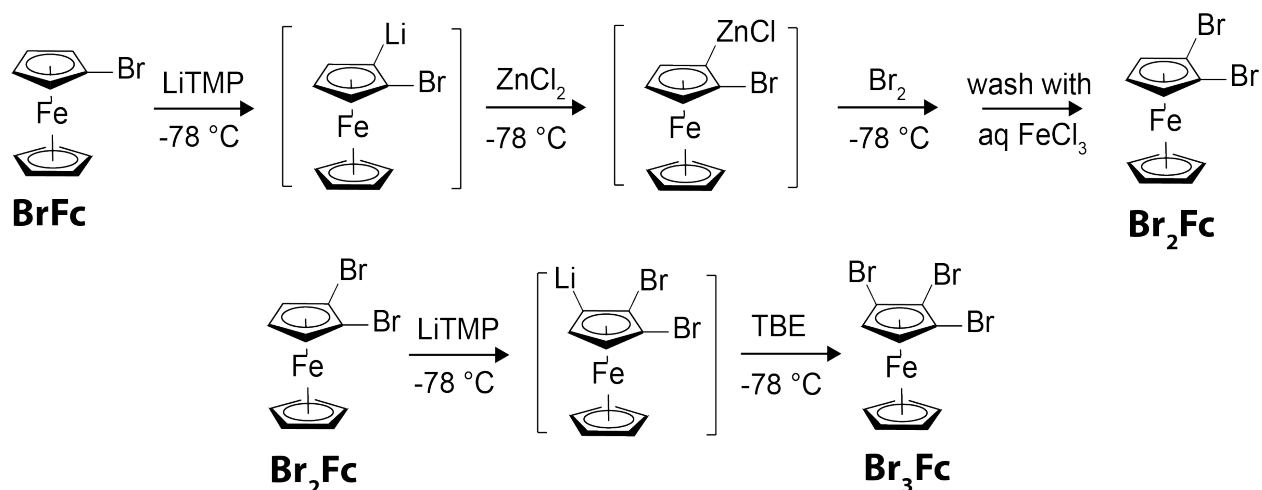
Figure A1. Synthesis of 1,2-dibromoferrocene (Br$_2$Fc) and 1,2,3-tribromoferrocene (Br$_3$Fc) from bromoferrocene (BrFc).

1,2-dibromoferrocene (Br$_2$Fc)

Adapted from Sunkel *et al*.[108] A 200 mL 3-neck round bottomed flask was charged with THF (20 mL), TMP (3.84 g, 27.2 mmol), and *n*-BuLi solution (15.5 mL, 24.8 mmol) at 0 °C and stirred for 30 min under argon. BrFc (6 g, 22.6 mmol) dissolved in THF (80 mL) was then added to the reaction mixture, still at 0 °C, and allowed to react for 60 min. At this point ZnCl$_2$ solution (13.3 mL, 25.2 mmol) was added and the reaction mixture was held at 0 °C for an additional 30 min. Upon cooling to -78 °C, Br$_2$ (1.74 mL, 33.9 mmol) was added dropwise. After 15 min, the reaction was quenched by pouring into ~300mL of 0.1 M HCl and extracted twice with DCM. The organic layer was then washed once more with ~300 mL of 0.1 M HCl, dried over MgSO$_4$, and the solvent removed under vacuum. The residue was purified by flash column chromatography using silica gel as the stationary phase and hexanes as the solvent to reveal 6 g of a 2 : 1 mixture of Br$_2$Fc : BrFc. The crude product was dissolved in ~150 mL of hexanes and washed twice with aqueous FeCl$_3$ (20 g in 150 mL), shaking vigorously for 10 min during each wash. The organic layer was washed once more with water, dried over MgSO$_4$, and the solvent removed under vacuum. The product was then dissolved in minimal boiling hexanes, and left to recrystallize at room temperature over night. Crystals were isolated via vacuum filtration, washing with cold hexanes, to reveal pure Br$_2$Fc (3.11 g, 9.0 mmol, 40% yield). **^{1}H NMR** (CDCl$_3$, 400 MHz) δ 4.44 (d, J = 2.8 Hz, 2H), 4.26 (s, 5H), 4.11 (t, J = 2.8 Hz, 1H).

Synthesis of 1,2,3-tribromoferrocene (Br$_3$Fc)

Adapted from Sunkel *et al*. A 200 mL 3-neck round bottomed flask was charged with THF (15 mL), TMP (1.23 g, 8.72 mmol), and *n*-BuLi solution (5.0 mL, 8.0 mmol) at 0 °C and stirred for 30 min. Br$_2$Fc (2.50 g, 7.27 mmol) in THF (50 mL) was then added and the reaction stirred for an additional 90 min at 0 °C. The reaction temperature was reduced to -78 °C prior to the addition of TBE (0.93 mL, 8.0 mmol). After 20 min, the reaction was quenched by pouring into water and extracted twice with DCM. The organic layer was washed once with 0.1 M HCl and then with water, dried over MgSO$_4$, and solvent removed under vacuum. The crude product was purified by flash column chromatography with a silica gel stationary phase and hexanes as the solvent, and further purified with two recrystallizations from minimal hexanes to yield pure Br$_3$Fc (1.08 g, 2.55 mmol, 35% yield). **^{1}H NMR** (CDCl$_3$, 400 MHz) δ 4.50 (s, 2H), 4.28 (s, 5H).

A.1.3 Friedel-Crafts acylation: Compounds 1-5

All compounds were synthesized in a similar manner.[74] The ferrocene derivative (Br_3Fc, Br_2Fc, $BrFc$, Fc, or Me_8Fc) and 6-bromohexanoyl chloride were dissolved in DCM. $AlCl_3$ was added at 0 °C under argon and the reaction was allowed to proceed for between 30 min and 1.5 hrs. The reaction was quenched with water, washed with sat. aq. $NaHCO_3$ and sat. aq. NaCl, dried over $MgSO_4$, and the solvent was removed in vacuum. The product was purified via column chromatography with hexanes and ethyl acetate. Ratios of reactants varied between reactions.

Synthesis of compound 1
    A 50 mL round-bottomed flask was charged with Br_3Fc (1.00 g, 2.37 mmol), 6-bromohexanoyl chloride (452 μL, 2.96 mmol), and DCM (20 mL). To this was added $AlCl_3$ (394 mg, 2.96 mmol) under argon at 0 °C. The reaction was quenched after 60 min by pouring into water, diluted with diethyl ether, washed with sat. aq. $NaHCO_3$, and twice with sat. aq. NaCl. The organic layer was dried over $MgSO_4$, and solvent was removed in vacuum. The crude product was purified via flash column chromatography with silica gel and a 10 : 1 hexanes : ethyl acetate mobile phase, which separated unreacted Br_3Fc and multiply reacted Br_3Fc from the desired product. The product was then recrystallized in hexanes overnight to yield pure **1** (1.1 g, 1.83 mmol, 77% yield). **^{1}H NMR** (CDCl$_3$, 400 MHz) δ 4.81 (t, J = 2.0 Hz, 2H), 4.52 (t, J = 2.0 Hz, 2H), 4.51 (s, 2H), 3.45 (t, J = 6.8 Hz, 2H), 2.76 (t, J = 7.4 Hz, 2H), 1.93 (m, 2H), 1.75 (m, 2H), 1.54 (m, 2H).

Synthesis of Compound 2
    A 25 mL round-bottomed flask was charged with Br_2Fc (500 mg, 1.45 mmol), 6-bromohexanoyl chloride (278 μL, 1.82 mmol), and DCM (12 mL). To this was added $AlCl_3$ (242 mg, 1.82 mmol) under argon at 0 °C. The reaction was quenched after 90 min by pouring into water, diluted with ethyl ether, washed with sat. aq. $NaHCO_3$, and twice with sat. aq. NaCl. The organic layer was dried over $MgSO_4$, and solvent was removed in vacuum. The crude product was purified via flash column chromatography with silica gel and a 10 : 1 hexanes : ethyl acetate mobile phase, which separated unreacted Br_2Fc from the desired product. Pure **2** was obtained upon removal of solvent from fractions obtained from the second visible band to elute off the column (600 mg, 1.15 mmol, 79% yield). **^{1}H NMR** (CDCl$_3$, 400 MHz) δ 4.80 (t, J = 2.0 Hz, 2H), 4.53 (t, J = 2.0 Hz, 2H), 4.45 (d, J = 2.4 Hz, 2H), 4.16 (t, J = 2.8 Hz, 1H), 3.45 (t, J = 6.8 Hz, 2H), 2.77 (t, J = 7.2 Hz, 2H), 1.93 (m, 2H), 1.75 (m, 2H), 1.54 (m, 2H).

Synthesis of Compound 3
    A 50 mL round-bottomed flask was charged with BrFc (800 mg, 3.02 mmol), 6-bromohexanoyl chloride (582 μL, 3.78 mmol), and DCM (20 mL). To this was added $AlCl_3$ (503 mg, 3.78 mmol) under argon at 0 °C. The reaction was quenched after 30 min by pouring into water, diluted with additional DCM, washed with sat. aq. $NaHCO_3$, and then washed again with sat. aq. NaCl. The organic layer was dried over $MgSO_4$, and solvent was removed in vacuum. The crude product was purified via flash column chromatography with silica gel and initially a 10 : 1 hexanes : ethyl acetate mobile phase to elute unreacted BrFc and the constitutional isomer of **3** in which acylation occurred on the cyclopentadienyl ring with the bromine. An eluent

containing 4 : 1 hexanes : ethyl acetate was then used to obtain pure **3** from the column (1.00 g, 2.25 mmol, 74 % yield). **^{1}H NMR** (CDCl$_3$, 400 MHz) δ 4.79 (t, J = 1.8 Hz, 2H), 4.53 (t, J = 2.0 Hz, 2H), 4.41 (t, J = 2.0 Hz, 2H), 4.14 (t, J = 2.0 Hz, 2H), 3.44 (t, J = 6.8 Hz, 2H), 2.76 (t, J = 7.4 Hz, 2H), 1.93 (quin, J = 7.1 Hz, 2H), 1.74 (quin, J = 7.6 Hz, 2H), 1.54 (m, 2H).

Synthesis of Compound 4

A 50 mL round-bottomed flask was charged with Fc (5.50 g, 35.2 mmol) and DCM (15 mL). To this was added AlCl$_3$ (2.19 g, 14.0 mmol) under argon at 0 °C, followed by the drop wise addition of 6-bromohexanoyl chloride (1.96 mL, 12.7 mmol) dissolved in DCM (5 mL). The reaction was quenched after 2 hrs by pouring into water, diluted with DCM, and washed twice with water. The organic layer was dried over MgSO$_4$, and solvent was removed in vacuum. The crude product was purified via flash column chromatography with silica gel and hexanes as the mobile phase to elute unreacted Fc. The column was then eluted with ethyl acetate to obtain **4** (2.13 g, 5.87 mmol, 46% yield based on 6-bromohexanoyl chloride). **^{1}H NMR** (CDCl$_3$, 400 MHz) δ 4.78 (t, J = 2.0 Hz, 2H), 4.50 (t, J = 2.0 Hz, 2H), 4.20 (s, 5H), 3.44 (t, J = 6.8 Hz, 2H), 2.73 (t, J = 7.2 Hz, 2H), 1.93 (quin, J = 7.1 Hz, 2H), 1.74 (quin, J = 7.5 Hz, 2H), 1.54 (m, 2H).

Synthesis of Compound 5

A 25 mL round-bottomed flask was charged with Me$_8$Fc (200 mg, 0.67 mmol) and DCM (4 mL). Under argon at 0 °C, 6-bromohexanoyl chloride (21 μL, 0.13 mmol) was first added, followed by the addition of AlCl$_3$ (48 mg, 0.36 mmol). The reaction was quenched after 30 min by pouring into cold water, diluted with diethyl ether, and washed with first sat. aq. NaHCO$_3$, then sat. aq. NaCl, and washed a final time with water. The organic layer was dried over MgSO$_4$, and solvent was removed in vacuum. The crude product was purified via flash column chromatography with silica gel and initially a 25 : 1 hexanes : ethyl acetate mobile phase to elute unreacted Me$_8$Fc. The column was then eluted with 10 : 1 hexanes : ethyl acetate to yield **5** (55 mg, 0.12 mmol, 92% yield based on 6-bromohexanoyl chloride). **^{1}H NMR** (CDCl$_3$, 400 MHz) δ 3.48 (t, J =7.0 Hz, 2H), 3.33 (s, 1H), 2.67 (t, J = 7.2 Hz, 2H), 2.06 (s, 6H), 1.92 (quin, 7.1 Hz, 2H), 1.81 (s, 6H), 1.70 (m, 2H), 1.68 (s, 6H), 1.62 (s, 6H), 1.51 (m, 2H).

A.1.4 Thiolation

All thiolation reactions were performed following the same procedure.[74] In a typical reaction, the product from the Friedel-Crafts Acylation was combined with (TMS)$_2$S in a vial containing 1-2 mL of THF per 100 mg of reactant. TBAF solution was then added drop wise at 0 °C under argon and the reaction was allowed to proceed for between 45 min and 1.5 hrs. The reaction was quenched by pouring it into cold water, diluted with diethyl ether, washed three times with water, and dried over MgSO$_4$. The solvent was removed in vacuum yielding an orange oil. Column purification was performed if necessary to remove the disulfide product.

Synthesis of Br$_3$FcOC$_6$SH

In an argon atmosphere, **1** (1.00 g, 1.66 mmol), (TMS)$_2$S (425 μL, 1.99 mmol), and 5 mL of THF were combined in a 20 mL vial. The vial was cooled to 0 °C and TBAF solution (1.83 mL, 1.83 mmol) was added drop wise. After 60 min at 0 °C, the reaction was halted by pouring into cold water, diluted with diethyl ether, and washed three times with water. The organic layer was dried over MgSO$_4$, and solvent was removed in vacuum. The resultant product

had a small disulfide impurity (<10%), but was not further purified since the disulfide would be washed away during the ligand exchange procedure. (0.90 g, 1.62 mmol, 97% yield). **¹H NMR** (CDCl$_3$, 400 MHz) δ 4.81 (t, J = 2.0 Hz, 2H), 4.52 (t, J = 2.0 Hz, 2H), 4.50 (s, 2H), 2.76 (t, J = 7.4 Hz, 2H), 2.57 (q, J = 7.3 Hz, 2H), 1.71 (m, 4H), 1.49 (m, 2H), 1.37 (t, J = 7.8 Hz, 1H). **HRMS** (ESI) exact mass calculated for [M+H⁺] (C$_{16}$H$_{18}$OSFe^{79}Br$_2$^{81}Br): m/z 552.7946; calc: 552.7952

Synthesis of Br$_2$FcOC$_6$SH

In an argon atmosphere, **2** (520 mg, 1.00 mmol), (TMS)$_2$S (256 μL, 1.20 mmol), and 5 mL of THF were combined in a 20 mL vial. The vial was cooled to 0 °C and TBAF solution (1.10 mL, 1.10 mmol) was added drop wise. After 60 min at 0 °C, the reaction was halted by pouring into cold water, diluted with diethyl ether, and washed three times with water. The organic layer was dried over MgSO$_4$, and solvent was removed in vacuum. The resultant product had a small disulfide impurity (<10%), but was not further purified since the disulfide would be washed away during the ligand exchange procedure. 413 mg, 0.87 mmol, 87% yield. **¹H NMR** (CDCl$_3$, 400 MHz) δ 4.80 (t, J = 2.0 Hz, 2H), 4.53 (t, J = 2.0 Hz, 2H), 4.44 (d, J = 2.8 Hz, 2H), 4.16 (t, J = 2.8 Hz, 1H), 2.76 (t, J = 7.4 Hz, 2H), 2.56 (q, J = 7.3 Hz, 2H), 1.70 (m, 4H), 1.49 (m, 2H), 1.36 (t, J = 7.8 Hz, 1H). **HRMS** (ESI) exact mass calculated for [M+H⁺] (C$_{16}$H$_{19}$OSFe^{79}Br$_2$): m/z 472.8859; calc: 472.8867

Synthesis of BrFcOC$_6$SH

In an argon atmosphere, **3** (946 mg, 2.13 mmol), (TMS)$_2$S (545 μL, 2.56 mmol), and 5 mL of THF were combined in a 20 mL vial. The vial was cooled to 0 °C and TBAF solution (2.40 mL, 2.40 mmol) was added drop wise. After 45 min at 0 °C, the reaction was halted by pouring into cold water, diluted with diethyl ether, and washed three times with water. The organic layer was dried over MgSO$_4$, and solvent was removed in vacuum. 820 mg, 2.06 mmol, 97% yield. ¹H NMR (CDCl$_3$, 600 MHz) δ 4.79 (t, J = 1.8 Hz, 2H), 4.53 (t, J = 1.8 Hz, 2H), 4.41 (t, J = 1.8 Hz, 2H), 4.13 (t, J = 1.8 Hz, 2H), 2.75 (t, J = 7.5 Hz, 2H), 2.56 (q, J = 7.4 Hz, 2H), 1.70 (m, 4H), 1.49 (m, 2H), 1.36 (t, J = 7.8 Hz, 1H). **HRMS** (ESI) exact mass calculated for [M+H⁺] (C$_{16}$H$_{20}$OSFe^{79}Br): m/z 394.9757; calc: 394.9762

Synthesis of FcOC$_6$SH

A 25 mL round-bottomed flask was charged with **4** (930 mg, 2.56 mmol), (TMS)$_2$S (654 μL, 3.07 mmol), and 5 mL of THF under an inert atmosphere. The reaction was cooled to 0 °C and TBAF solution (2.82 mL, 2.82 mmol) was added drop wise. After 60 min at 0 °C, the reaction was halted by pouring into cold water, diluted with diethyl ether, and washed three times with water. The organic layer was dried over MgSO$_4$, and solvent was removed in vacuum. The crude product was purified via flash column chromatography with silica gel and a 4 : 1 hexanes : ethyl acetate mobile phase, which separated residual Fc and a dithiol impurity from the desired product. 450 mg, 1.42 mmol, 56% yield. ¹H NMR (CDCl$_3$, 600 MHz) δ 4.78 (t, J = 2.0 Hz, 2H), 4.50 (t, J = 2.0 Hz, 2H), 4.20 (s, 5H), 2.71 (t, J = 7.4 Hz, 2H), 2.56 (q, J = 7.5 Hz, 2H), 1.70 (m, 4H), 1.49 (m, 2H), 1.37 (t, J = 7.8 Hz, 1H). **HRMS** (ESI) exact mass calculated for [M⁺] (C$_{16}$H$_{20}$OSFe): m/z 316.0582; calc: 316.0579

Synthesis of Me₈FcOC₆SH

In an argon atmosphere, **5** (55 mg, 0.12 mmol), (TMS)$_2$S (30 μL, 0.14 mmol), and 2 mL of THF were combined in an 8 mL vial. The vial was cooled to 0 °C and TBAF solution (0.13 mL, 0.13 mmol) was added drop wise. After 90 min at 0 °C, the reaction was halted by pouring into cold water, diluted with diethyl ether, and washed three times with water. The organic layer was dried over MgSO$_4$, and solvent was removed in vacuum. 40 mg, 0.09 mmol, 80% yield. ^{1}H NMR (CDCl$_3$, 600 MHz) δ 3.33 (s, 1H), 2.66 (t, J = 7.4 Hz, 2H), 2.56 (q, J = 7.5 Hz, 2H), 2.06 (s, 6H), 1.81 (s, 6H), 1.69 (s, 6H), 1.67 (m, 4H), 1.62 (s, 6H), 1.46 (m, 2H), 1.35 (t, J = 7.8 Hz, 1H). **HRMS** (ESI) exact mass calculated for [M$^+$] (C$_{24}$H$_{36}$OSFe): m/z 428.1822; calc: 428.1831

A.2   Synthesis of CdSe/CdS Core/Shell QDs

Synthetic details for the 3, 5, and 7 ML CdSe/CdS QDs used in Chapter 2 may be found in our previously published work.[50] The procedures described below are nearly identical as the ones used in this work.

A.2.1   Chemicals

Trioctylphosphine oxide (TOPO, 99%), selenium (Se, 99.99 %), cadmium oxide (CdO, ≥ 99.99%), oleic acid (OA, 90%), 1-octadecene (ODE, 90%), oleylamine (OLAM, 70%), and 1-octanethiol (OctSH, ≥ 98.5%) were purchased from Sigma-Aldrich and used as received. Other chemicals used include tri-*n*-octylphosphine (TOP, 99%, STREM) and octadecylphosphonic acid (ODPA, 99%, PCI Synthesis) and the anhydrous solvents acetone, isopropanol, and hexanes.

A.2.2   CdSe core synthesis

QDs described in sections 3.3 and 3.4:

CdSe cores were synthesized following a previously reported procedure.[111] In a typical reaction 120 mg of CdO, 560 mg of ODPA, and 6 g of TOPO were combined in a 25 mL round-bottomed flask, and degassed under vacuum at 150 °C for 30 min. The reaction vessel was then heated to 320 °C under argon, and maintained at that temperature until the solution turned clear, indicating full complexation of Cd. In some cases a second degas step was performed after complexation. At 320 °C, 2 mL of TOP was injected into the reaction solution, which was then heated to between 370 and 380 °C for the injection of Se (120 mg) dissolved in TOP (1 mL). Upon injection, CdSe nanocrystals were allowed to grow for between 30-60 seconds to achieve the desired size, then rapidly cooled. QDs were cleaned in air with successive precipitation and dissolution using hexanes (solvent) and isopropanol or acetone (non-solvent), and were stored in hexanes in an inert environment. See Table A1 for details on quantity of reactants used in each shelling reaction as well as the resultant QD size.

QDs described in section 3.5 and Chapter 4 (thin shells):

The typical reaction described above was scaled down by a factor of two. Additionally, upon injection, CdSe nanocrystals were allowed to grow for 15 seconds to produce the larger cores. To produce the smaller cores, 5 mL of ODE was injected into the reaction mixture immediately following Se-TOP injection to halt growth. QDs were cleaned in an inert

atmosphere with successive precipitation and dissolution using hexanes (solvent) and isopropanol (non-solvent), and were stored in hexanes in an inert environment. The large CdSe QDs had a first excitonic absorption feature at 590 nm, the first batch of smaller CdSe QD's first absorption feature was at 476 nm (used to make the 4.1 and 3.6 nm core/shells), and the second batch of small CdSe QD's first absorption feature was at 473 nm (used to make the 4.3 nm core/shells). Sizing and concentrations were determined by a previously reported empirical formula.[80]

A.2.3 CdS shell growth

QDs described in sections 3.3 and 3.4:

QDs were synthesized following previously published procedures.[50,112] Multiple reactions were run under slightly varying conditions. The quantity of CdSe QDs used ranged from 250 to 900 nmols, as determined by optical extinction of the first excitonic feature.[81] In a typical reaction, CdSe QDs were first degassed at room temperature for an hour and next at 120 °C for 30 min in a solution with equal volumes of OLAM and ODE. The total volume of OLAM and ODE ranged from 3-6 mL per 100 nmol of QDs used. The reaction was then heated under argon to 310 °C, and held there for the duration of the shell growth. Slow injection of 0.2 M OctSH in ODE and 0.2 M cadmium oleate in ODE was started at 250 °C, and continued for 2 hours. Injection solution volumes varied between 6 and 12 mL for each precursor. Upon injection completion, the reaction was maintained at 310 °C for 10 min, then cooled to room temperature. The core/shell QDs were isolated from excess ligand via precipitation in acetone and redispersion in hexanes, repeated two or three times. Insoluble impurities were often precipitated out via centrifugation in hexanes only. QDs were stored in either hexanes or chloroform in an inert environment.

QD Sample	CdSe peak abs.	Quantity of QDs	OLAM + ODE vol.	Cd or S Inj. volume	Core/shell diameter (error)
1	559 nm	900 nmol	40 mL	8 mL	7.3 (0.4) nm
2	563 nm	300 nmol	18 mL	9 mL	10.6 (1.2) nm
3	565 nm	666 nmol	36 mL	12 mL	8.3 (0.6) nm
4	560 nm	250 nmol	8 mL	6 mL	11.9 (1.8) nm
5	560 nm	500 nmol	24 mL	8 mL	8.8 (0.6) nm

Table A1. Synthetic details for the five QD samples, including the location of the first excitonic absorption feature of the cores, the quantity of cores used, and the volumes of solvent and injection solutions. The resultant core/shell diameter is also shown.

QDs described in section 3.5 and Chapter 4 (thin shells):

The 3.6 and 4.1 nm core/shell QDs were synthesized by first degassing 4 mL ODE, 4 mL OLAM, and 200 nmol of the first batch of small CdSe cores in a 50 mL flask at RT for 1 hr and 120 °C for 20 min. The solution was heated to 310 °C, and injection of Cd and S precursor solutions in ODE began when the flask reached 240 °C. For the 3.6 nm dots, the Cd precursor solution contained 0.06 mmols of $Cd(OA)_2$ in 1 mL of ODE and the S precursor contained 10.5 μL of OctSH in 1 mL ODE. The precursor solutions were injected over the course of 30 min. For the 4.1 nm dots, the Cd precursor solution contained 0.10 mmols of $Cd(OA)_2$ in 1 mL of ODE

and the S precursor contained 17.3 μL of OctSH in 1 mL of ODE. The precursor solutions were injected over the course of 1 hr.

The 4.3 nm core/shell QDs were synthesized by first degassing 8 mL ODE, 8 mL OLA, and 400 nmol of the second batch of small CdSe cores in a 50 mL round-bottomed flask at RT for 30 min and 120 °C for 30 min. The solution was heated to 310 °C, and injection of Cd and S precursor solutions in ODE began when the flask reached 240 °C. The Cd precursor solution contained 0.2 mmols of $Cd(OA)_2$ in 2 mL of ODE and the S precursor contained 35 μL of OctSH in 2 mL of ODE. The precursor solutions were injected over the course of 1.5 hrs.

The 6.3 nm core/shell QDs were synthesized by first degassing 3 mL ODE, 3 mL OLA, and 100 nmol of the large CdSe cores in a 50 mL flask at RT for 1 hr and at 125 °C for 25 min. The solution was heated to 310 °C, and injection of Cd and S precursor solutions in ODE began when the flask reached 230 °C. The Cd precursor solution contained 0.144 mmols of $Cd(OA)_2$ in 2 mL of ODE and the S precursor contained 30 μL of OctSH in 2 mL of ODE. The precursor solutions were injected over the course of 1.5 hrs.

Upon completion of precursor injection, all reactions were maintained at 310 °C for ten min, cooled to RT, and cleaned in an inert environment by precipitating the QDs in acetone and re-suspending in hexanes. This cleaning process was repeated twice, and samples were stored in hexanes under an inert atmosphere.

A.3 Ligand Exchange

Chapters 2 and 3:

Ferrocene ligands were added to QD solutions at room temperature in chloroform. Since the thiol readily displaces the native oleate ligand, extent of exchange was controlled by amount of ferrocene added. Excess ligand was removed via precipitation with acetonitrile and disposal of the supernatant. The lack of significant free peaks in the ^{1}H NMR (Figure 3.5) indicates that this purification was successful, although incomplete cleaning sometimes resulted in free ligand at concentrations up to 5 % that of the bound concentration. This could easily be quantified by peak fitting, and accounted for in determining the bound ferrocene concentration.

Appendix B: Characterization methods

B.1 Transmission electron microscopy (TEM)

Transmission electron microscopy (TEM) samples were prepared by drop-casting dilute solutions of nanoparticles onto carbon film 400 square mesh copper grids (Electron Microscopy Sciences). Images were acquired on a FEI Tecnai T20 with a LaB_6 filament and 200 kV accelerating voltage.

B.2 Electrochemistry

Cyclic voltammograms (CVs) of ferrocene ligands (Chapter 3)

CVs were recorded on a CHI-600C electrochemical analyzer. Measurements were performed under argon in quiescent THF electrolyte with 0.1 M TBA-PF$_6$ as the supporting electrolyte. A freshly polished 3.0 mm diameter glassy carbon button electrode served as the working electrode and a platinum mesh served as the counter electrode. An encased silver wire electrode with a porous Teflon tip filled with a 10mM $AgNO_3$, 0.1 M TBA-PF$_{6,}$ acetonitrile solution served as the reference electrode (part no. CHI112, CH Instruments). The concentration of ferrocene ligand in solution was approximately 1 mM. CV scans were performed at 10, 50, 100, 250, 500, and 1000 mV s^{-1} and E$_{1/2}$, taken at the average of the oxidation and reduction peak potentials, did not depend on scan rate. All potentials were calibrated using an Fc* ($E_{1/2} = -427$ mV vs Fc/Fc$^+$ in THF)[79] internal standard added to the electrochemical cell after CVs were performed on the analyte.

Low temperature QD conduction band measurements (Chapter 3)

QD films on ITO were prepared by drop-casting dilute solutions of QD sample 1 onto the conductive glass slides, followed by immersion in a 1 % 1,2-ethanedithiol solution in methanol for 3 hrs at 55 °C. The slides were then cleaned with methanol, hexanes, and chloroform. Cyclic voltammograms (CVs) were recorded on a CHI-600C electrochemical analyzer. Measurements were performed under argon in quiescent chloroform electrolyte with 0.1 M TBA-PF$_6$ as the supporting electrolyte, and at -40 °C (with an acetonitrile/ dry ice bath). The QD coated ITO served as the working electrode and a platinum mesh served as the counter electrode. An encased silver wire electrode with a porous Teflon tip filled with a 10mM $AgNO_3$, 0.1 M TBA-PF$_{6,}$ acetonitrile solution served as the reference electrode (part no. CHI112, CH Instruments). All potentials were calibrated using an Fc* ($E_{1/2} = -483$ mV vs Fc/Fc$^+$ in chloroform)[79] internal standard added to the electrochemical cell after CVs were performed on the QD film.

B.3 Quantitative NMR

Quantitative ^{1}H NMR spectra were obtained on a Bruker 400 MHz instrument. Ligand concentrations were computed from absolute integration values divided by the number of scans and referenced to a standard sample of known concentration. The standard sample was 10 mM Fc in d_8-toluene. For all quantitative NMR spectra, the 90° pulse was calibrated and the dwell time between successive scans was ensured to be at least five times T$_1$.[70]

B.4　Inductively coupled plasma (ICP) atomic emission spectroscopy

Nanocrystal concentration was determined by measuring the Cd^{2+} concentration using an Optima 7000 DV ICP-AES (Perkins Elmer) and calculating the number of Cd atoms per nanocrystal for the given size as determined via Transmission Electron Microscopy (TEM). Cadmium ICP standards serially diluted to cover a range of concentrations were measured to generate a calibration curve. Nanocrystal samples are prepared by evacuating a 200µl aliquot of the stock solution, and then adding 500µl of nitric acid to digest the particles for a few hours. The solutions were then diluted in Millipore water in the same series of dilutions as the Cd^{2+} ICP standards, and measured.

B.5　Optical spectroscopy

Absorption spectra were collected on a Shimadzu 3600 spectrophotometer. Emission spectra were obtained on a Horiba Jobin Yvon TRIAX 320 Fluorolog

Experiments in Chapter 2 and sections 3.3 and 3.4:

PLQYs were determined by diluting the solutions of QD-ferrocene conjugates used for NMR by factors of typically 100-800x into chloroform and taking absorption and fluorescence measurements. In a typical QY measurement, four dilutions of differing concentrations were prepared. A plot was then generated of the integrated fluorescence intensity vs. $1-10^{-A}$, where A is the absorption of the sample at the excitation wavelength (500 nm in our case). The slope of this line is proportional to the quantum yield, and by comparing to the slope generated by a standard dye (Rhodamine 6G, QY= 96% in ethanol) will yield the QY. This relationship is shown in the Equation A1:

$$QY = QY_R \left(\frac{Flint_R}{1 - 10^{-A_R}}\right)^{-1} \left(\frac{Flint}{1 - 10^{-A}}\right)\frac{n^2}{n_R^2} = QY_R \frac{Slope}{Slope_R}\frac{n^2}{n_R^2} \qquad \text{(A1)}$$

Where QY_R is the QY of the reference, *Flint* is the integrated fluorescence intensity, *n* is the index of refraction of the solvent used, and *A* is the absorption (with subscript *R* denoting the reference sample).[113] Note that it is important to calibrate the fluorescence detector in these measurements.

The linearity of the QY plot (Figure A2), even at high ferrocene coverage indicates that ferrocene ligands are not in dynamic exchange with the surface. If there were dynamic exchange, at low concentration more ligand would desorb resulting in higher relative fluorescence intensities.
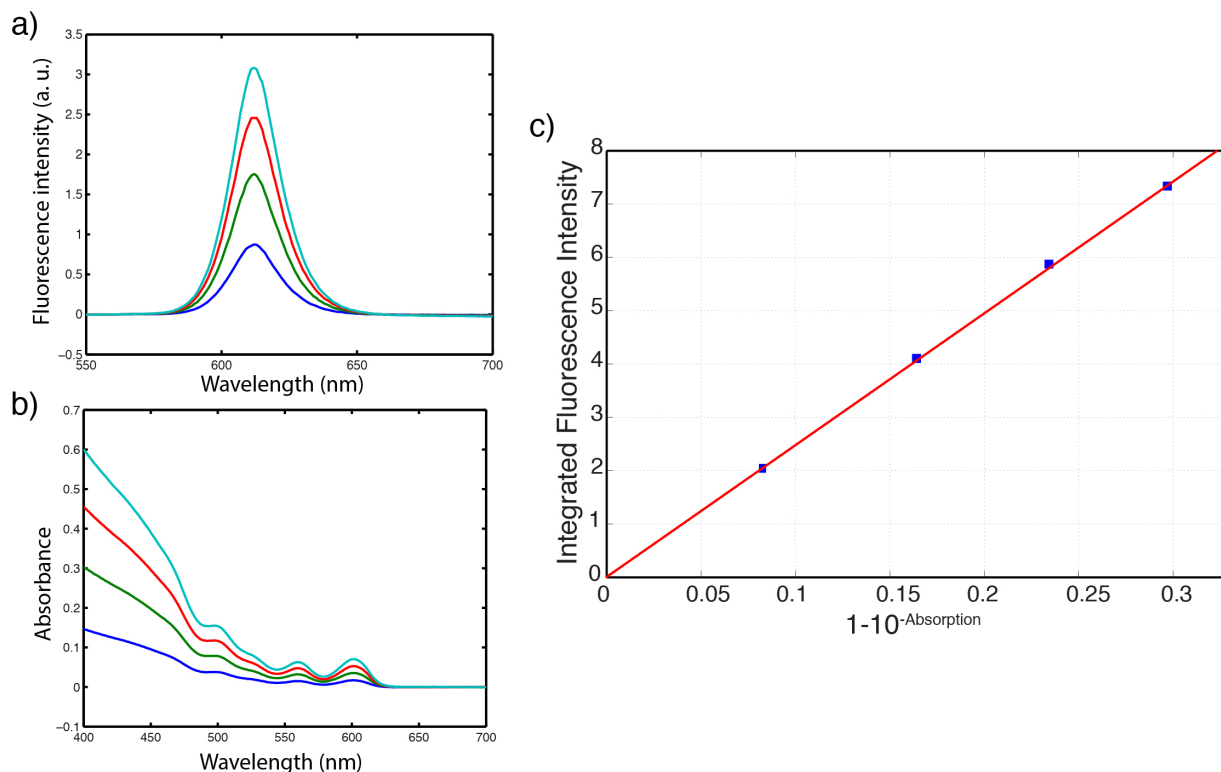
Figure A2. Data collected from an arbitrarily chosen sample for determining QY (QD sample 1 from section 3.4, exchanged with Br_3FcOC_6SH at highest coverage). (a) Fluorescence spectra and (b) absorption spectra of this sample at four dilutions. (c) The plot of integrated fluorescence intensity vs. $1-10^{-A}$, with a best-fit line (red).

Experiments in section 3.5 (thin shells):

   PLQYs of native QDs were obtained on a custom built integrating sphere fluorometer described in published work from the Alivisatos group.[114] Emission spectra and PLQYs of ligand-exchanged samples were recorded relative to the native QDs. Steady state fluorescence quenching curves were performed on 3 mL, ~0.3 µM, QD solutions in hexanes with 10 µL aliquots of a given ferrocene ligand in toluene added sequentially (each data point in Figure 3.11(a-c) represents a ferrocene aliquot addition).

Experiments in Chapter 4:

   Photoluminescence lifetime measurements were acquired using a time-correlated single photon counting apparatus consisting of a Picoquant Fluotime 300 spectrometer, a PMA 175 detector, and an LDH-P-C-405 diode laser with a 407 nm excitation wavelength. A 1.0 MHz repetition rate was used. Approximately 1 nmol of QDs and 10-20 nmols of ferrocene ligand were dissolved in 0.6 mL of 2,2,4,4,6,8,8-heptamethylnonane (98%, Sigma-Aldrich), an optical glass forming solvent, and were then loaded into a sample cell with two sapphire windows and an inert spacer. The sample cell was placed on a holder within a Janis ST-100 continuous flow optical cryostat and cooled under flowing liquid nitrogen. The temperature was tuned controllably via a Lakeshore 330 temperature controller.

   Temperature dependent PLQY measurements were performed in flame sealed NMR tubes containing QD-ferrocene conjugates in 0.4 mL of 3-methylpentane. Tubes were immersed in liquid nitrogen and then quickly transferred to the integrating sphere fluorometer described

above. Spectra were obtained every second for five to ten minutes to allow the tube to warm to room temperature. This process was repeated as necessary to obtain adequate data.

B.6   IR absorption spectroscopy

Approximately 5 nmol of QDs dissolved in 300 µL of hexanes were combined with 10-50 µL of a THF solution containing 500-2000 nmol of lithium triethylborohydride (Super-Hydride, 1.0 M in THF, Sigma-Aldrich). This solution was kept in an inert, dark, environment and loaded into an IR cell with CaF_2 windows and a 500 µM spacer. It was crucial to make sure the cell was impermeable to oxygen and remained dark prior to taking a baseline spectrum on a Bruker IFS 66v/S vacuum FT-IR. The sample was then exposed to light from a UV lamp (365 nm) for 30 sec increments prior to acquiring an IR spectrum. The intensity initially increased after each 30 sec exposure to UV light, but eventually decreased presumably due to oxidation of the photodoped dots. The peak intensity spectrum was used in the plot in Figure 3.9b. Although the IR absorption spectra of photo-doped QDs were baselined to the undoped QDs, certain spectral regions had large enough solvent absorption signals that an accurate subtraction was not possible. These regions were removed in the plot in the main text but the raw (scaled) data is shown below.
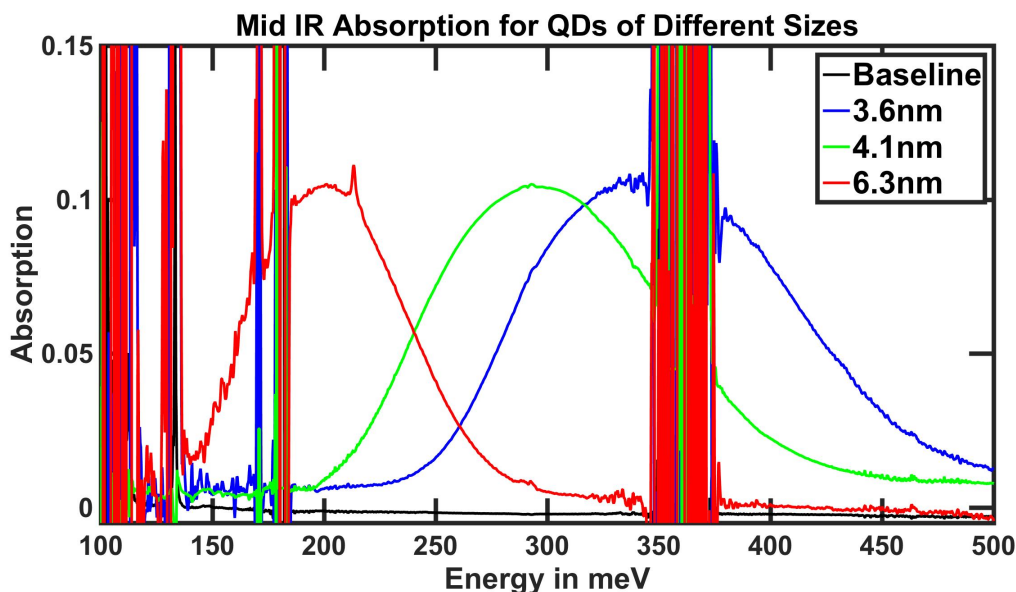

Figure A3. IR absorption spectra of CdSe/CdS QDs in hexanes and THF photodoped with lithium triethylborohydride. A scan of the same solutions prior to UV exposure served as the baselines.

B.7   Mass spectrometry

High resolution mass spectrometry analysis was done by electrospray ionization using a Finnigan LTQFT Mass Spectrometer (Thermo) via direct injection with a flow rate of 5 µL per min. Analytes were prepared in 20-50 µM solutions in acetonitrile.